Design of a Solid-State Electrochemical Methane Sensor Based on Laser-Induced Graphene

by

Manan Dosi

A thesis
presented to the University of Waterloo
in fulfillment of the
thesis requirement for the degree of
Master of Applied Science
in
Chemical Engineering

Waterloo, Ontario, Canada, 2018

AUTHOR'S DECLARATION

I hereby declare that I am the sole author of this thesis. This is a true copy of the thesis, including any required final revisions, as accepted by my examiners.

I understand that my thesis may be made electronically available to the public.

Abstract

Methane is a potent greenhouse gas with significant, yet largely unknown, emissions occurring across gas distribution networks and mining/extraction infrastructure. The development of low-cost, low-power electrochemical sensors could provide an inexpensive means to carry out distributed and easy sensing over the entire network and to identify leaks for rapid mitigation. In this work, a simple and cost-effective approach is proposed for developing electrochemical methane sensors which operate at room temperature with the highest reported sensitivity and response time.

Laser-induced graphene (LIG) technology, which selectively carbonizes commercial polyimide films using a low-cost CO_2 laser cutting and patterning system is utilized. Interdigitated LIG electrodes are infiltrated with a dilute palladium (Pd) nanoparticle dispersion which distributes within and coats the high surface area LIG electrode. A pseudo-solid state electrolyte ionic liquid (IL)/polyvinylidene fluoride was painted onto the flexible cell resulting in a porous electrolyte structure which allows for rapid gas transport and improved three-phase contact between methane, IL and Pd. By subjecting the resulting sensors to methane in a gas flow cell, with off-gas analysis analyzed by Fourier transform infrared spectroscopy, the performance of the sensor over a wide range of operating conditions can be determined and the methane oxidation mechanism can be investigated. The optimized system provides a rapid response (less than 50 s) and high sensitivity (0.55 $\mu A/ppm/cm^2$) enabling a ppb-level detection limit.

Acknowledgements

First and foremost, I would like to express my sincere gratitude to my supervisors Professor Michael Fowler and Professor Michael Pope for their continuous support and guidance during my entire Master's program. In addition to the great deal of technical knowledge I have acquired under their supervision, I have also learned how to communicate efficiently, how to conduct myself professionally, and how to approach any challenge with fortitude and determination. My time as a student has been a very rewarding experience in large part due to friendly and professional demeanour of both these Professors.

I would also like to extend my thanks to Professor David Simakov and his student Yichen Zhuang for allowing me to use their lab space and help in running experiments.

I would also like to thank my colleagues, Muneendra Prasad Arcot, Irene Lau, Dilara Yilman and Manoj Matthew for helpful discussions and to all my friends at Waterloo for making my time here a very enjoyable experience.

Finally, I would like express my deepest gratitude to my parents and my brother who have always been there for me. As I move on to the next chapter of my life, it is comforting to know that, regardless of wherever life takes me, I will always have a loving family to lean on.

Table of Contents

LIST OF FIGURES

LIST OF TABLES

Chapter 1: Introduction, Research Objectives and Outline

1.1 Introduction

Methane is the major constituent of natural gas. As a result of mining and various defects in the natural gas pipeline network, methane emissions occur throughout the oil and gas industry. This leads to the largest anthropogenic source of the hazardous greenhouse gas (25 times more potent than CO_2) and causes a significant loss in revenue for the industries. Almost 60% of methane loss is due to fugitive release, out of which a large percentage is due to transmission lines (pipelines).[1]

However, these leaks at this point are challenging to identify or detect due to the expansive nature of the distribution network. The currently available sensing technology that includes optical and combustion based sensors are expensive and not viable for detecting minor leaks.[2] The sensors require higher temperatures and also have a slow response time and typically must be monitored manually. Gas pipelines that are spread throughout a country's terrain covering thousands of miles of distance, makes it impossible to find and address all leaks using the currently available portable detection systems. Plant and facility configuration involve numerous potential valve, flanges and potential leakage points. Moreover considerable skilled manpower is required to accomplish such a task.

The focus of this research is to develop an electrochemical sensor with methane sensing capabilities. The research aims to fabricate, low power and inexpensive methane sensor, which can detect any fugitive emissions or leaks occurring in and around the natural gas pipelines.

1.2 Motivation

Methane is a significant climate change forcing greenhouse gas with a short-term impact 25 times greater than carbon dioxide.[3] According to data from Canada's United Nations Framework Convention on Climate Change (UNFCCC), oil and gas methane accounts for approximately 6% of Canada's total GHG emissions when the 100 year global warming potential of methane is considered.[3]

In addition to natural gas exploration and transmission, methane is released and extracted during oil sands mining and processing activities. It is estimated that these activities release about 10% of the greenhouse gases (GHGs) generated in the extraction sector.[3] In addition to being a potent GHG, methane build-up in enclosed spaces also poses a significant safety concern.

Although Canada only accounts for approximately 1.6% of the world's GHG emissions, it is among the top 10 countries for absolute emissions. Standing firmly in the top three for estimated emissions per capita, Canada comprises 0.5% of the world's population, but emits three times its population share.[1]

It is projected that a 45% reduction in methane emissions can be achieved by monitoring unintended emissions through implementation of currently prevailing technologies. As reported in the Pembina Institute's report, "A 45% reduction of oil and gas methane is equal to 27 million tonnes of CO_2 (56 Bcf of methane), and is achievable with existing technologies and techniques. This reduction comes at a net cost of $2.76 CAD per ton CO_2 reduced.[1] If the natural gas is valued at $5.00 CAD per Mcf. The methane reduced results in recovery of gas worth approximately $251.10 million CAD ($200.80 million USD) per year."[1]

Canada played an active role at the Paris COP21 (21st Conference of the Parties) which led to a global agreement on mitigation, adaptation and financing of climate change action.[3] The current government policy indicates that Canada will seek to fulfill its global responsibility in reducing GHGs.

In May of 2015, the government submitted its Intended Nationally Determined Contribution (INDC) to the UNFCCC indicating an economy-wide target of reducing GHG emissions by 30 % below 2005 levels by 2030.[3]

Reduction in current methane emissions will be a major step towards meeting the GHG reduction goals of the country. Methane sensor technology will play a vital role in this direction as it helps to detect fugitive emissions which account for a major part of the current emissions. The benefit of this technology is to detect the emission of GHG's. "In Alberta, the oil and gas sector is the largest source of methane emissions. Methane emissions in 2014 from Alberta's oil and gas sector

were 31.4 mega tonnes of carbon dioxide equivalents. This accounted for 70% of provincial methane emissions and 25% of all emissions from the upstream oil and gas sector"[3]. Methane sensor technology will also help Canada to fulfill its pledge of reducing its emissions to below 30% of 2005 levels by 2030.

There are also economic benefits for using methane sensor technology in detecting and thus reducing emissions from an economic perspective; the industrial segments of ownership such as oil and gas production can grow by making money by reducing gas losses. This is also true in some other segments. Most midstream companies (gathering, processing, and storage) are paid a fixed fee for gas lost and consumed during their operations; a reduction in loss would result in a direct monetary profit.

1.3 Research Objectives

This thesis work aims to develop a new, cost-effective electrochemical methane detection technology to help reduce the methane emissions through distributed monitoring and thus providing tools for the government and industry to meet their emission standards. Accomplishment of these objectives would lead to a fully developed functional electrochemical methane sensor.

1. To understand the importance of methane sensing for fugitive emissions and comprehend the different methane sensors that are available, their advantages and shortcomings. In addition, this work will investigate the feasibility of an electrochemical methane sensor and understand the mechanism involved in the preparation and running of the sensor.
2. Development of electrochemical sensor materials, an effective sensor geometry and methods to configure a thin film, conformable sensor which can sense methane at room temperature.
3. Prototype testing of sensor in dry conditions. Investigate the operating conditions of the sensor and develop ways to optimize the performance and reduce the cost. Design experiments to figure out the sensitivity response at different concentrations of methane, signal noise ratio, response time. Finally, initiate cost analysis, modeling and design studies for sensor commercialisation.

1.4 Thesis Outline

Chapter 2 will highlight the important research that has been conducted in field of methane sensing. More specifically, it will examine the different categories of methane sensors, their properties such as sensitivity, cost, range etc. It will also provide a brief overview of electrochemical methane sensors and their advantages and disadvantages compared to other sensors. Finally a comparative analysis of different sensors will be done based on a variety of parameters.

Chapter 3 will dwell into the experimental methods used in fabrication of electrochemical methane sensor. The methods involved in fabrication of interdigitated electrodes, nanoparticle synthesis, solid polymer electrolyte development, deposition techniques and various setups for testing the sensor for sensitivity towards methane will be discussed in detail.

Chapter 4 discusses the results obtained during the preparation and testing of the sensor. The characterization and results obtained from laser induced graphene electrodes will be discussed. The morphology of Pd nanoparticle and solid polymer electrolyte obtained from techniques such as SEM and the reaction mechanism that has been established with various methods will be discussed in depth. The sensitivity response of the sensor at various concentrations will be looked into, while parameters such as response time, and signal to noise ratio will be presented. Finally, electrochemical impedance spectroscopy results, effect of interference gases and life time analysis of sensor will be discussed.

Chapter 5 entails a model developed in COMSOL that dwells into leakages across a flange in a natural gas pipeline. The model is based on a pin-hole leak and is an early attempt in modelling the gas leakage. It tries to develop efficient approaches to minimize the usage of sensor by placing it optimally on a flange. At the end cost estimation of the sensor will be discussed.

Finally, Chapter 6 will present the conclusions of this research and discuss possible future work.

Chapter 2: Literature Review and Background

This chapter will provide a review of the theoretical background applied in this research. It will first introduce the current methane detection technologies available. This will be followed by a discussion on the different type of methane sensors such as electrochemical sensors, optical sensors, catalytic combustion sensors, pyroelectric sensors and semiconducting oxide sensors. The discussion includes their detection mechanism, properties such as sensitivity, selectivity, cost, detection range, fouling issues and current technology readiness. Finally, electrochemical methane sensors with a focus on the current detection challenges will be addressed.

2.1 Sensor classification categories:

The methane sensors can be broadly classified as:

1. **Optical Sensors**
2. **Catalytic Combustion Sensors**
3. **Pyroelectric sensors**
4. **Semiconducting oxide sensors**
5. **Electrochemical Sensors**

2.2 Optical sensor

Optical sensors use absorption spectroscopy to detect certain chemical compounds such as methane gas.[4] Infrared absorption spectroscopy is the most commonly used form of spectroscopy for optical methane sensors because it can be used to qualitatively analyze molecules by measuring the wavelength and intensity of the absorption of mid-infrared light.[5] Certain chemical bonds have specific absorption band wavelengths making it possible to identify the composition of a given sample. For example the atmospheric transmission of methane has a wavelength of 2.3 μm and 3.26 μm.[6]

A typical optical methane gas sensor is composed (shown in Figure 2-1) of a light source to provide the mid-infrared light, a tube to hold the gas sample being tested, an optical spectrum detector and a spectral filter. During operation mid-infrared light is emitted from the light source and reflects along the inside walls of the tube as it passes through the sample gas. As the light passes through the sample gas the gas molecules that vibrate within the infrared frequency range

would absorb the infrared radiation provided from the light source. After passing through the gas the infrared light would reach the optical spectrum detector which would produce a measurement of the output intensity of the emitted light. Using both the initial intensity of the light source and the length of the sample which are known quantities along with the output intensity, a value for the effective absorption coefficient of the gas can be determined. The effective absorption coefficient would be used to identify whether methane was present in the sample gas by comparing measured and literature values. The use of a spectral filter improves the measured value of the effective absorption coefficient because it blocks spectral regions that are not greatly affected by the sample gas allowing the detector to focus on the regions of high absorption.[7]

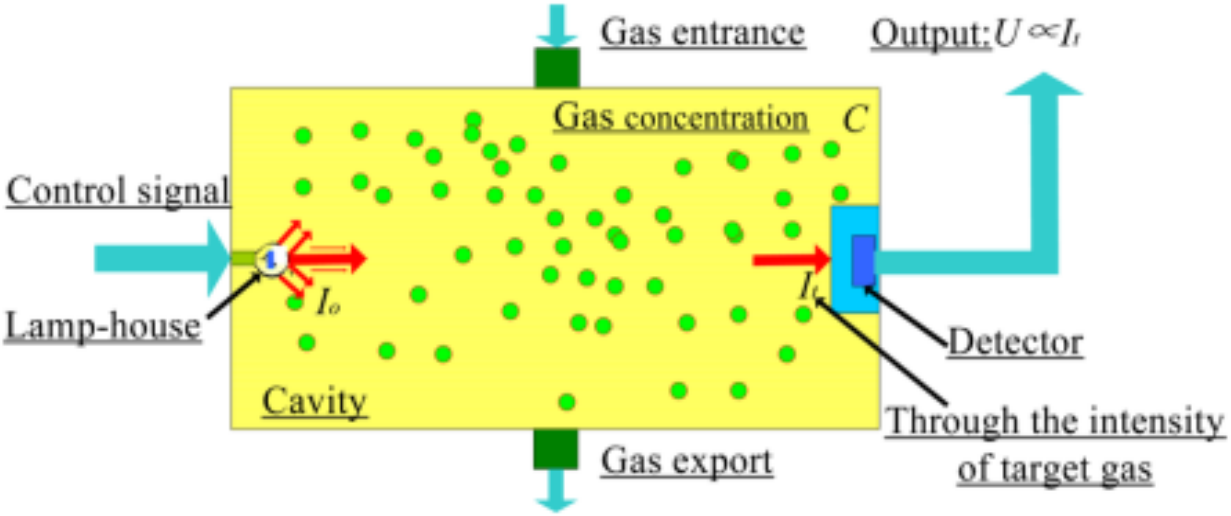

Figure 2- 1: Gas Detection by IR Absorption Spectroscopy [21]

The technology applied in the operation of optical methane sensors is already at the point where it is viable for industry. Currently there are multiple optical methane sensors on the market that are based on infrared laser spectroscopy. The optical sensors available on the market belong to one of two categories, either they are *in situ* (on-site) sensors or they have remote sensing capabilities. The more common of the two are the *in situ* sensors which require physical sampling of the air to be tested for methane detection. An example of an *in situ* optical methane sensor on the market would be the mobile methane leak detector manufactured by Health Consultants Incorporated. This methane sensor was developed to detect methane along natural gas distribution, transmission and gathering pipelines and is mounted to a vehicle during operation. If methane is detected

through infrared spectroscopy as the vehicle drives along the pipeline, both an audio and visual signal is sent to a display inside the vehicle alerting the operator. Similarly, Lechtzer Incorporated manufactured an optical methane sensor that is also attached to a vehicle and detects methane as one drives. [8] There are also hand-held detectors that are used detection of methane leaks along pipelines. The remote sensing methane detectors still detect methane by infrared spectroscopy but don't require physical sampling of a gas; instead the detector surveys a specific area and relays a signal through an optical fibre network when methane is detected. Applied Optoelectronics is an example of a company that manufactures remote sensing optical methane detectors for various industries.[8]

Even though there are many operational optical methane sensors on the market there are still lab-scale experiments that continuously try to optimize the design. Typically the focus of these experiments is to improve the sensors selectivity, sensitivity and response time as these three fields are vital for sensing operations. Selectivity is important because there are many hydrocarbons at a similar wavelength as methane so the more sensitive the sensor is the more accurate it will be at detecting methane. Sensitivity is important so that the sensor will be able to detect methane concentrations at low levels and response time is important because in industry quickly detecting methane leaks is critical.

An innovation that focuses on increasing the sensitivity of the sensors is the use of a long period fibre grating (LPFG) optical sensor with a polycarbonate/ cryptophane A overlay deposition. LPFGs (shown in Figure 2-2) are used to couple light from a guided node towards forwards propagating cladding modes and can have their sensitivity increased through the use of overlays.[9] In one experiment a polycarbonate/ cryptophane A overlay was used as an overlay due to its high refractive index. Altering the overlay thickness caused the resonant wavelength to shift and at optimal thickness there was found to be a drastic shift in resonant wavelength that resulted in a great increase in the sensor's sensitivity.[2] Through the use of the polycarbonate/ cryptophane A overlay the optical sensor was able to achieve a minimum methane detection limit of 0.2% on a volume be volume basis.[10]

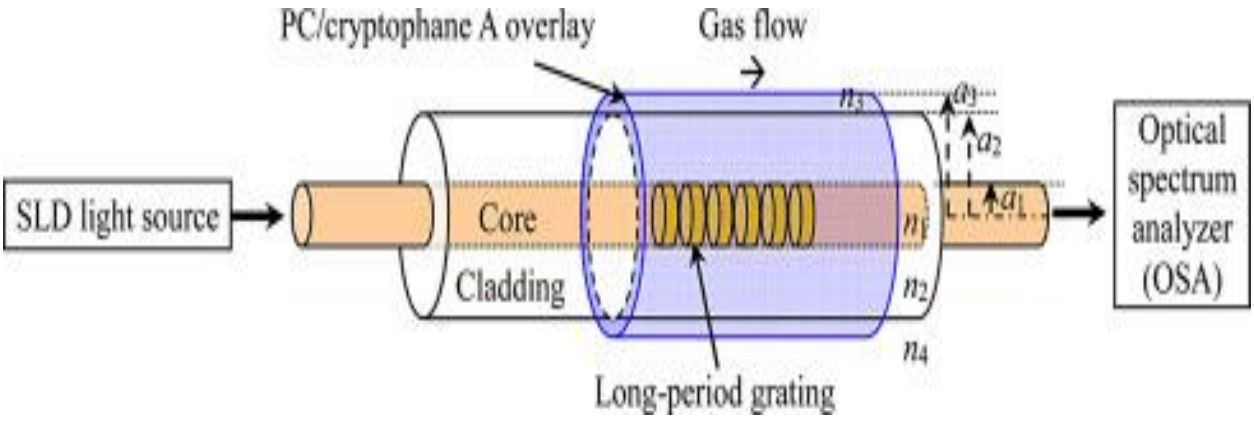

Figure 2- 2: Basic Design of a LPFG Optical Sensor [2]

The detection of methane gas leaks is very important for many industries and results in a large demand for precise but low cost sensors. Optical methane sensors are good for these industrial applications because of their low cost when compared to other methane sensors due to the fact that the main working principle behind optical methane sensors is absorption spectroscopy. Absorption spectroscopy requires much lower costs than other forms of analysis such as mass spectroscopy or gas spectroscopy but have very high operating costs when used for detection in a larger setting.[11]

Optical methane gas sensors and calorimetric gas sensors have similar low operating costs but where calorimetric sensors are non-selective, optical methane sensors have the advantages of being highly selective like gas spectroscopy based methane sensors which have high costs.[12] One of the main reasons that optical methane gas sensors have low costs is because they have a low cost of ownership or in other words optical sensors are non-destructive.[7] Since absorption spectroscopy is a physical process not a chemical reaction during operation the actual sensing apparatus is not damaged and does not require replacing unlike other methane sensors that use chemical reactions to detect the methane gas. The bulk of the cost associated with optical methane sensors is the manufacturing (capital) cost itself. The cost of production would increase if there was a need to increase the sensitivity of the methane sensor as more individual components would be needed, for example having two detectors in the sensor instead of one. Also the cost of production would also increase if there was a need to increase the selectivity of the sensor by adding a spectral filter or narrowing the bandwidth and tolerance of a spectral filter already in

use.[7] These capital cost for precise detection makes optical sensors less desirable when detecting minor gas leakages in pipelines which are spread in hundreds of miles.

Optical methane sensors are useful for many industrial applications because they provide many advantages with few disadvantages when compared to other methane sensing technologies. One of the biggest advantages of optical methane sensors is that absorption spectroscopy is a physical analysis method not a chemical reaction which makes optical sensing a non-destructive method of detecting methane. This means that the components do not get degraded after repeated operation which in turn reduces any maintenance costs that other methane sensors would have to deal with. Another important advantage that optical methane sensors have is that they are immune to any electromagnetic interference which in other sensing techniques would impair the sensor from operating properly.[2] Also optical methane sensors are very versatile and can be adapted to fit the requirements of various applications. There are portable designs available allowing for use in different environments and whether the application is detecting a possible leak or monitoring a specific area the sensors can be designed to be manual or remote sensing. Some other advantages include the ability to operate in the absence of oxygen, have fast response time, does not require any pre-treatment or build-up of gas sample, low cost and have good selectivity and sensitivity. The table below lists the sensitivities of various optical sensors currently available.

Table 2- 2: List of sensitivity of optical sensors

Method	**IR Source Wavelength**	**Sensitivity**
Fabry-Perot Cavity[10]	1650 nm	0.7-2.9 ppm-m
Interband Cascade Laser[11]	3291 nm	1.0-2.1 ppm-v
QEPAS[6]	2300 nm	~ 15 ppm-v
Infrared LED[7]	1660 nm	~ 100 ppm
LPFG[2]	1550 nm	~100 ppm

The main disadvantage of optical sensors is that to be effective the target gas should have a significant and distinct optical absorption region. The problem is that methane has absorption bands in the same spectral region as many other hydrocarbons.[7] This issue can be easily

overcome by increasing the selectivity of the sensor by adding a spectral filter, however this would lead to an increase in the production costs of the sensor.

2.3 Catalytic combustion sensor

Catalytic bead sensors have been in use for almost a decade and are primarily used to detect combustible gases, more generally in industrial safety instruments. They were initially used for the detection of methane and other gases in coal mines.[13] Combustible gas mixtures will burn once they reach their ignition temperature but in the presence of a particular chemical process, these mixtures can ignite at lower temperatures. This process is known as a catalytic combustion. Many metal oxides and compounds have these catalytic properties to help the combustion process such as platinum and palladium.

The basic principle of catalytic sensors is based that the oxidation of combustible gases to release heat. A "pellistor" (catalytic pallet resistor) is used as the major sensing mechanism in catalytic

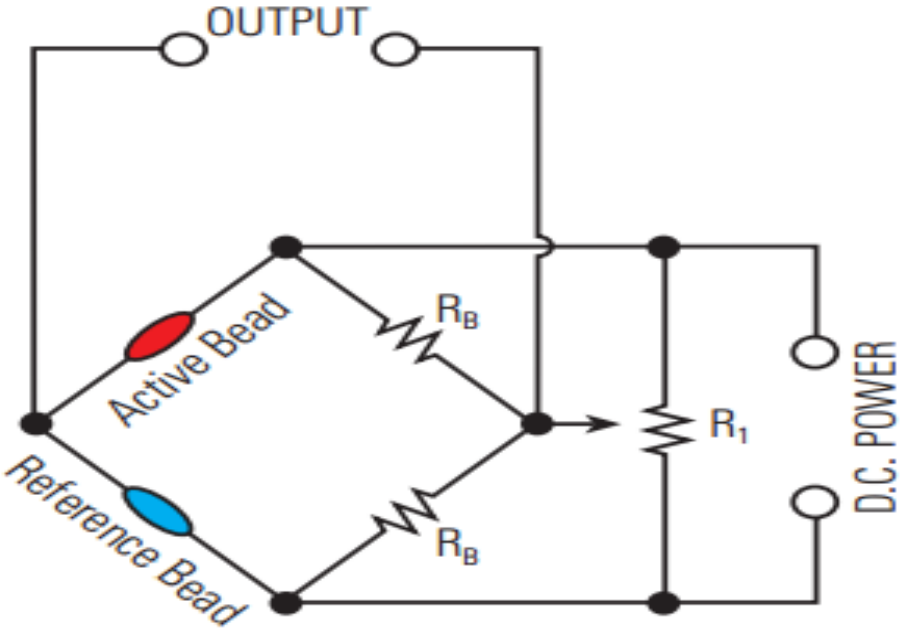

Figure 2- 3: A Wheatstone bridge configuration for catalytic bead sensor.

sensors. This pellet usually consists of a platinum wire embedded within a ceramic bead. A surface layer of noble metal is utilized as a catalyst for the combustible gas oxidation reaction. Pellistors are manufactured in pairs where one acts as the detector while the other acts as a reference

resistance to remove the potential effects of environmental factors.[14] The oxidation of combustible gas when in contact with the catalyst is an exothermic reaction and releases heat.[15] This results in a temperature change within the coil and causes the resistance of the coil to change. An electrical circuit called a Wheatstone bridge, as seen in Figure 2-3, is used to measure this resistance.[13] During the burning of the gas of interest, it causes an imbalance of the bridge circuit. The offset voltage is measured as the signal and can be used to measure resistance, capacitance, inductance, impedance, and concentration.

The catalytic gas sensor is a popular due to its simplistic design, ease in manufacturing, and being inexpensive. Environmental factors such as temperature, exposure to water vapour and pressure will influence both pellistors. Since these pellistors are similar in nature, they will be influenced similarly and as such, the Wheatstone bridge will not become unbalanced.[14] This property makes it possible for the catalytic gas sensor to operate in harsh environmental conditions.

The calorimetric gas sensor measures the heat released during the exothermic combustion oxidation reaction on the sensor surface. These devices are also known as pellistor, catalytic bead, catalytic gas sensor, combustible gas sensor, or thermometric gas sensor.[16] Platinum, palladium, and rhodium [17] are the most used catalysts in calorimetric gas sensors.

Gas calorimeters are used in steel mills, petrochemical furnaces, and power plant turbines. Calorimeters for natural gas and coal gasification are used for measuring the exothermic heat during the combustion of fuels in burners and turbines in industrial settings. Typical calorimeters are large monitoring units for industrial-scale systems.[17]

New Cosmos – BIE offers a catalytic combustion sensor that utilizes a platinum coil. SRI Instruments Europe's catalytic combustion detector consists of a coil of platinum wire embedded in a catalytic ceramic bead to detect hydrocarbons and H_2 gas.[14] Finally, Figaro Engineering Inc. offers various catalytic sensors to detect methane, propane, and iso-butane.[18]

The original catalytic sensor was a coil-shaped platinum wire which gave a compact geometry resulting in efficient heating. Unfortunately, at high temperatures, platinum starts to evaporate, causing a reduction in the platinum area and increases resistance, making it more difficult for the detection of combustible gases. Additionally, the platinum wire can become soft above 1000^{o}C

and can warp the geometry of the wire. Treating the surface of the wire by applying a coating of metal oxides of palladium or theoria compounds improves the stability of the sensor and reduces the temperature issues. The reference wire should ideally be identical to the active wire, with similar geometry and properties but remain inert. While it is not actually possible to make them exactly the same, various compromises have been considered. Lowering the operating temperature of the reference wire and treating the reference wire with gold to modify the material's properties are examples of ways to accomplish this. Using a fine diameter wire will reduce the size, increase the signal of the sensor, and reduce the power consumption.[13]

A method to optimize a sensor is to cut the bead more deeply to create larger channels for the gas diffusion to the active sites of the sensor. This is particularly useful for detection of large hydrocarbon molecules which will be able to easily diffuse in the sensor. Since the heat produced from the reaction will cause the heating of molecules which will escape more easily, there is less attenuation in the atmosphere, resulting in a higher relative response of the sensor.[18] There are several calibration strategies to prevent incorrect readings due to the loss of sensitivity to methane. One method is to calibrate the sensor to a known concentration of methane which uses the relative response factor to determine if there is a less of sensitivity.[19] This can then be used to calibrate the instrument to make up for the sensitivity variation.

The catalytic combustion sensor was initially used for the detection of methane and other gases in coal mines. Nowadays, applications include detection of combustible gases in industrial safety instruments, controlling heat inputs in various furnaces and turbines, and to monitor the combustion reaction of fuels in burners and turbines in the industrial setting.

The general cost can range from $1-$3 USD for individual sensor units up to $100-$1000 USD for prebuilt-incased sensors.[20] Prebuilt-incased infrared gas sensors can range from $300-$2000 USD.

Catalytic combustion sensors have various advantages including a low cost, low replacement cost, ability to detect a wide variety of combustible gases and vapors, simplistic design and easy to manufacture. Additionally, it can be very portable and has a good selectivity for methane and other volatile hydrocarbon vapors.[21] Compared to the infrared technology, it is much cheaper if

operated in the correct setting as the lifespan can be drastically shorten if contaminated or poisoned.

The disadvantages include not being able to operate long-term, requires elevated temperatures, susceptible to catalyst poisoning, sensor inhibitors, and cracking.[20] Poisoning compounds can deactivate the sensor by permanently reducing sensitivity until eventually completely damaging the sensor, resulting in the sensor becoming nonresponsive to gases.

2.4 Pyroelectric sensor

Pyroelectric sensors involves the conversion of thermal energy into electrical energy. To do this pyroelectric sensors employ the use of a dielectric substrate and a pyroelectric detector that is sandwiched between two electrodes. In pyroelectric sensors the dielectric substrate is an electrical insulator that when an electric field is applied becomes polarized and typically has a high thermal conductivity to minimize any heat loss.[22] The detection process for pyroelectric sensors can be divided into a few main stages, the first stage being the generation of the thermal energy or wave that will propagate through the substrate which is typically caused by either a resistive heater or infrared light source.

The resistive heater generates the thermal energy by passing an electrical current through a highly resistive material, as the current flows it generates heat at a steady rate that can travel through the substrate. The thermal wave travels through the gas of interest until it reaches the pyroelectric detector located across from the resistive heater. When a pyroelectric material undergoes a

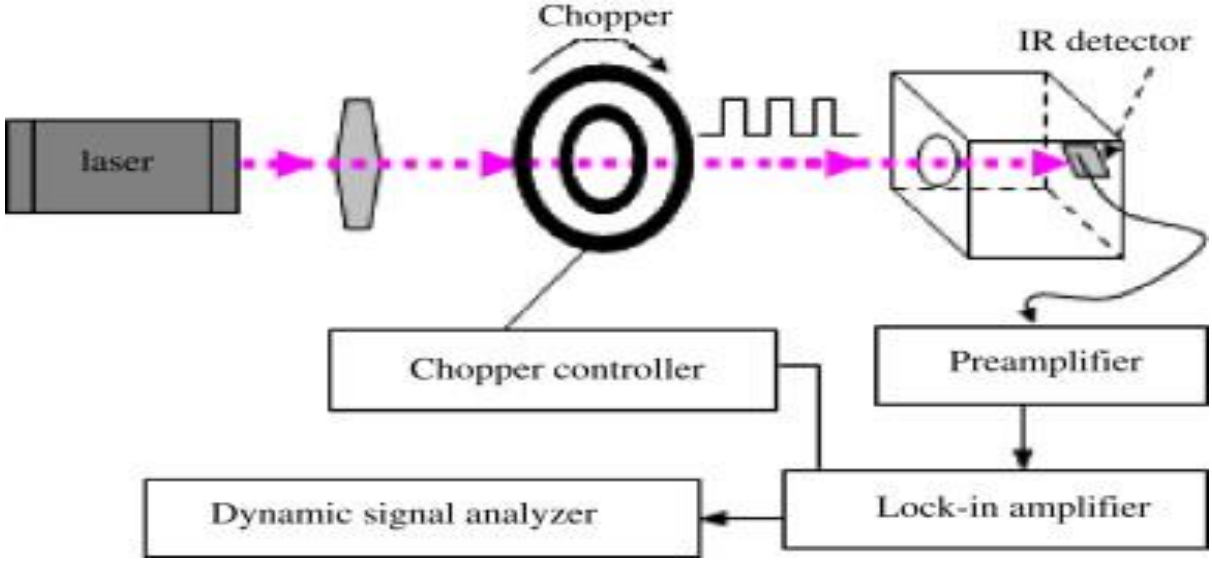

Figure 2- 4: Basic Design of Pyroelectric Sensor based on Infrared Heating [40]

temperature change it produces an electrical current that can be measured.[23] This current has a corresponding voltage which can be used to find the composition of the gas of interest because both the voltage and phase of the output signal are a function of the gas's thermal conductivity and diffusivity.[24] The other method causes a temperature change in the pyroelectric material by focusing an intense infrared light source on a pyroelectric thin film.[24] Once the pyroelectric material changes temperature the sensor operates in the same way as the electric heater method mentioned previously.

The technology used in the operation of pyroelectric methane sensors (shown in Figure 2-4) is already past the experimental phase of development and can be found on the market. There are multiple pyroelectric sensors used to detect gases including methane available that are based on the pyroelectric effect. An example of this is the pyroelectric detector developed by InfraTec that uses single-crystalline lithium tantalate as its think film pyroelectric material.[25] This pyroelectric detector is very versatile as it can be used for methane detection as well as many other applications such as motion detection and flame detection. For gas sensing applications there are specific filters that can be used to target the detection of specific gases such as methane.

Even with pyroelectric methane sensors already on the market there are still many experiments being run to improve the design by increasing the overall sensitivity and reducing the sensor's power consumption. Sensitivity is always important quality for gas sensors to have because the target gases are typically in very low concentrations so the sensor must be able to pick up these minuscule readings. Also low power consumption is an important factor since many applications require the pyroelectric sensors to be portable, for example they might need to be taken to the location of a possible methane leak from a pipeline.

According to the pyroelectric effect that states when a pyroelectric material undergoes a temperature change it produces a current, therefore the thicker electrically active area of the lithium tantalate would undergo a larger temperature change and produce an increased output signal compared to that of a simple thin film sensor. From this study it was found that altering the structure of the pyroelectric material in this way could increase the sensitivity/responsivity of the sensor by 150%.[26]

Due to their characteristic pyroelectric sensors are applicable for a variety of industries. Since they provide high responsivity and excellent detection pyroelectric sensors are used in applications such as fire alarms[27], laser detectors[24][27], thermal analyzers[25][27] and gas analysis.[27]

Pyroelectric sensors are used for environmental applications such as gas analysis and pollution control because there is a need to quickly detect leaks and accurately determine the composition of the leak itself. This makes them a good choice for the oil and gas industry, water treatment plants and landfill sites where the detection of methane is a large safety and environmental concern.[28] Also another reason why pyroelectric sensors are used for these applications is that they can be designed to be a portable or remote-sensing sensor depending on the situation. Typically pyroelectric sensors that are based on infrared heating are used for applications that require remote sensing such as gas monitoring in coal mines. Detection of gases in coal mines can be very dangerous which is why it is beneficial if monitoring can be done from a remote location and infrared pyroelectric sensors make that possible.[26] Portable pyroelectric sensors are useful for applications where there is a need to check for possible leaks and can be based on electric heater or infrared principles.

As previously stated there are many applications that pyroelectric sensors can be used for but to have any practical use there are certain criteria that have to be met. For pyroelectric sensors to be an effective method of methane detection in industry they must be low cost to allow for easy availability and widespread use.

The main cost benefit of pyroelectric methane sensors as opposed to some other sensors such as photon sensors is that they do not require any cooling.[28] Pyroelectric methane sensors that use infrared light detection methods work well at room temperature unlike other sensors types that require a form of constant cooling. This eliminates the need to have any additional equipment to cool the sensor which in turn greatly reduces operational costs.[27]

Pyroelectric methane sensors can be very useful in industrial applications because they provide many advantages that distinguish them from other sensor types. One main advantage is that pyroelectric sensors are able to operate at room temperature.[28] As mentioned previously this reduces operating costs by eliminating the need for cooling equipment but it also enables pyroelectric sensors to be used in a variety of environments and climates. To add to its versatility

pyroelectric sensors can function in environments absent of oxygen as well as inert atmospheres. Another advantage of pyroelectric sensors is that the technology they are based on is a physical process. The pyroelectric effect is a thermal process and does not involve any chemical reactions like some other sensor types which could lead to degradation. Some other advantages that pyroelectric methane sensors have are high sensitivity, easy miniaturization, wide measuring range and excellent responsivity. The table lists the sensitivities of the sensor currently available.

Table 2- 3: List of sensitivity of pyroelectric sensors

Method	Material	Sensitivity
NDIR[29]	Mgg lamp (6004-10)	~ 1 ppm
Thermal Wave Pyroelectric Film[23]	organic polycyclic molecular crystalline substance	~ 50 ppm

Pyroelectric sensors also have some disadvantages, the main one being the high power consumption compared to other sensors. As stated previously the power consumption is a result of a need for a constant current or constant infrared light source to provide the thermal energy required for methane detection.[28] Some other minor disadvantages would be slow degradation of components due to repeated heating and the potentially high operating costs.

2.5 Semiconducting oxide sensor

Semiconducting metal oxides (SMO) are electrical conductivity sensors that detect gas by a REDOX reaction when a gas of interest comes in contact with the sensor. The gas of interest will absorb onto the sensor's active sensing layer which causes a change in the resistance; the concentration of the gas can be determined from this resistance change.[30] They are inexpensive compared to other sensing technologies, lightweight, robust, and long lasting.[31] SMOs are well-suited for a wide range of applications and for a variety of reactive gases.

A SMO sensor possesses an electrical resistance made of a porous assembly of tiny crystals of n-type metal oxide semiconductors, such as SnO_2 or WO_3.[32] When heated to a high temperature in the absence of oxygen, electrons will flow through the grain boundaries of the SMO film. On the other hand when oxygen is present, the oxygen molecules will absorb onto the SMO surface

to form a potential barrier. This forms ionic species including O_2^-, O^- and O^{2-}, which trap electrons from the bulk of the material. This will also repel other electrons from the bulk of the film, to create a region with a reduced amount of electrons; thus resulting in an increased potential barrier at the grain boundaries. Due to this interaction, it will reduce the flow of electrons which will increase the resistance. When exposed to an atmosphere containing a reducing gas such as CH_4 and H_2S, the gas molecules will absorb onto the SMO surface and lowers the potential barrier, thus increasing the concentration of electrons at the surface while reducing the electrical resistance.[33] In the case of oxidizing gases such as NO_2 and CO_2, the electrical resistance will increase. Several researchers have reported that the conductivity response is highly affected by the presence of a catalyst, which will increase the surface reactivity.[34] Figure 2-5 is a schematic of a SMO sensor design during a study conducted for the United States Environmental Protection Agency's Environmental Monitoring Systems Laboratory.[35]

Figure 2- 5: Schematic of a metal oxide semiconductor sensor.

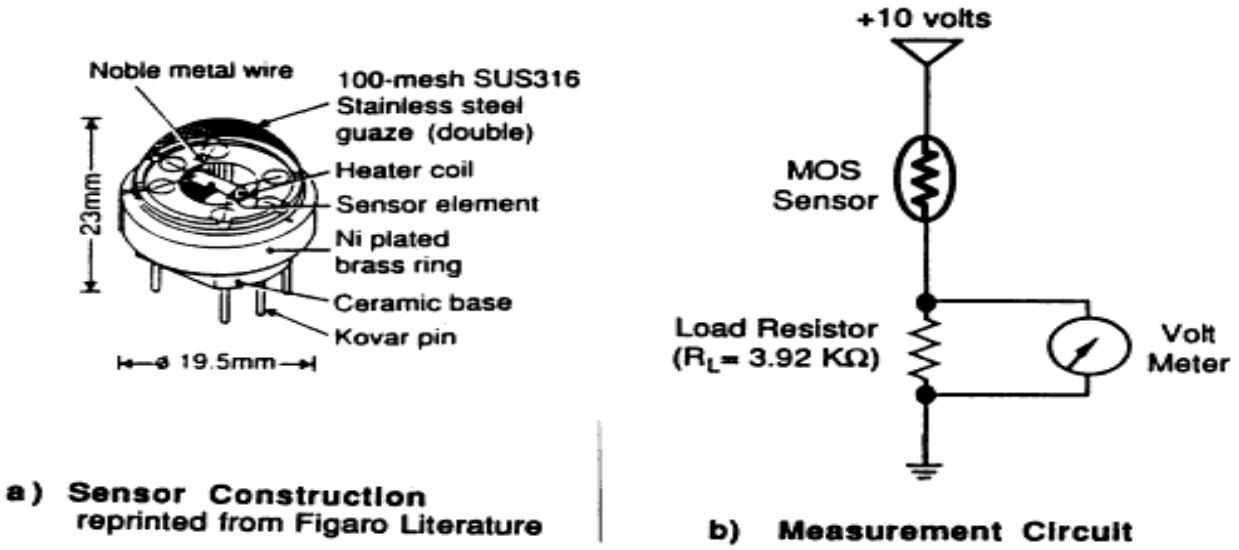

In the case of SMO sensors for CH_4 gas, a number of metal oxide materials have been studied as seen in Table 2-2[33]:

Table 2- 4: Gas sensing properties of unloaded/loaded metal oxide semiconductors for methane gas.

Sensing Material	Method	Gas Concentration	Sensing Response
7 wt% Sb/ZnO[34]	Screen printing	1000 ppm	~25 to 1000 ppm at 360°C
SnO_2[31]	Thin films on micromachined SOI wafers	1%/room temperature – 700°C	~23 at 500°C to 1% Response time: 5-10 ms
SnO_2-ZnO (0-15 wt% ZnO)[36]	Thick films	50 ppm/170-330°C	~1 (10% ZnO loaded SnO_2) at 300°C to 50 ppm Response time: ~2s
Unloaded WO_3[30]	RF-sputtering (sensors)	1000 ppm	< 0.5 to 1000 ppm at 300-500°C
Unloaded SnO_2, Pt/SnO_2, Mo/SnO_2, Cu/SnO_2[33]	Thin films on alumina substrates by CVD	1000 ppm/450-500°C	0.4, 0.72, 1.03, 1.50 to 1000 ppm, at 500°C respectively Response time: ~5s

Conductometric semiconducting metal oxide sensors have been widely used in various domestic, commercial, and industrial gas sensing systems. They currently constitute one of the most investigated groups of gas sensors due to their low cost and flexibility in production, wide variety of detectable gases, and lightweight.[33] In addition, SMO sensors tend to be long-lived and resistant to poisoning. For these reasons, they have grown rapidly in popularity to become the most widely used gas sensors available. They are used in environmental monitoring and gas detection, carbon monoxide sensors, and breath analyzers. Most common detected gases include nitrogen oxide gases (NOx), H_2S, NH_3 and amine sensors, hydrogen, ozone, carbon monoxide, and methane gas. [34]

Researchers have determined that the interaction of the gas with the surface of the material is a characteristic of semiconducting metal oxide gas sensors. The reaction can be influenced by many

factors such as natural properties of base materials, surface areas and microstructure of sensing layers, surface catalyst, temperature and humidity, etc. The principle of the classical semiconductor gas sensors is well known since the development of the "Taguchi-type" sensors.[37]

Doping the metal oxide layer will enhance the sensing characteristics of the oxide semiconductor. For example, doping SnO_2 with Sb, Cl, and F increases the conductivity. Depositing SnO_2 on Ti presents high over potentials for the oxygen generation reaction, giving good anodes for the electrochemical oxidation.[38] The addition of noble metal additives can be used to modify or control the surface properties of semiconductor metal oxides. The most important aspects of the additives are to increase the maximum sensitivity and rate of response, as well as lowering the temperature of maximum sensitivity.

Semiconductor gas sensors can be used for a wide variety of applications, ranging from safety equipment (explosion, leakage, fire, contamination, and poisoning protection), air quality monitoring, quality assurance, and measurement technology. Unfortunately, they are susceptible to contaminants and changes due to environmental conditions. Non-linear response will cause complexity in the readings. Additionally, solid state metal oxide semiconducting gas sensors can be susceptible to background gasses, or have cross-selectivity, and are sensitive to changes in humidity. There are options and configurations to help mitigate the sensitivity but it is an inherent characteristic of the sensing technology.

2.6 Electrochemical Sensors

2.6.1 Aqueous electrolyte based electrochemical sensor.

Electrochemical gas sensors generally operate upon the principles of differential electric double layer capacitance (DEDLC), amperometry and potentiometric to name a few.[39] A typical sensor design is modelled after the conventional three electrode system: a working electrode where the substrate will undergo a redox reaction, a counter electrode which balances the current at the working electrode, and a reference electrode with which to measure the working electrode potential against. In practice, most sensor designs compartmentalize the reference electrode to its own cell while being in contact with the electrolyte, also the working and counter electrodes must be connected by an electrolyte to maintain charge neutrality in the system. Aqueous electrolytes

(AEs) are routinely used to fulfill this role since they are widely available, relatively cheap, and simple to use. Some examples of common AEs are sulfuric acid (H_2SO_4) and sodium hypochlorite (NaClO).

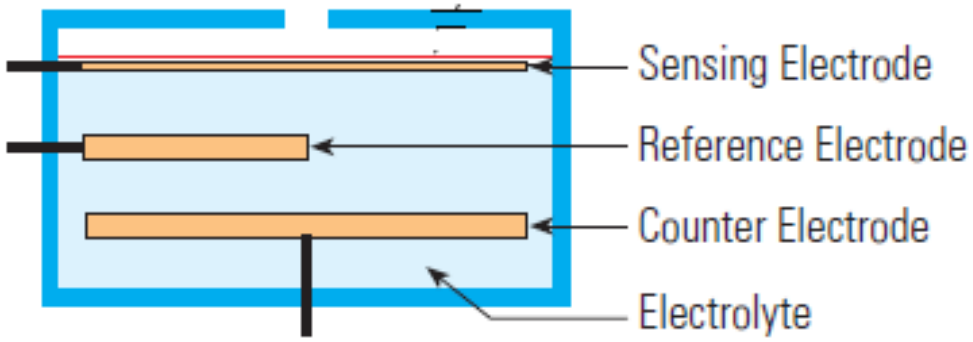

Figure 2- 6: Typical electrochemical sensor setup [39]

Despite their widespread use, aqueous electrolyte-based sensors (AESs) introduce a variety of problems in gas sensor design. First and foremost, AESs suffer from limited working lifespans primarily due to the volatility of the AEs used; evaporation of the AE requires that sensors of this design must be replaced more frequently than would be desired, translating to increased maintenance costs for the projects that employ them (mining, natural gas transportation, etc.). Of additional concern is the potential for interference through the electrolysis of water; in the practice of voltammetry, the potential range in which water is not electrolyzed is referred to as the "water window", and overpotentials outside of this range (1.5 V – 3.5 V) will cause considerable loss of accuracy in the sensor. AESs also often require extreme process conditions to carry out the redox reactions required to sense certain analyte gases. For example, methane oxidation can require process temperatures ranging from 775 °C down to 50 °C, depending on the type of electrolytes and catalysts used (i.e. yttria-stabilized zirconia[40], lanthanide ruthenium oxide[41], Nafion-sulfuric acid[42], etc.). Additionally, methane oxidation is kinetically slow; this in turn has led to the design of systems utilizing hot acid electrolytes and platinum (Pt) catalysts, which give a reasonable oxidation rate. However, aside from the safety hazards associated with such a system, these designs also suffer from side-reactions which produce CO by-products, poisoning the catalyst and reducing the lifespan of the sensor[43]. Another issue is that AESs generally suffer

from significant signal interference from other common gases such as H_2, C_2H_6 and C_3H_8.[44] It is clear that while AEs are convenient and cheap to use, their associated drawbacks prevent AESs from reaching widespread commercial viability.

2.6.2. Ionic Liquid (RTIL) based electrochemical sensor.

Room temperature ionic liquids (RTILs) are commonly defined as the salts which happen to be in a liquid state under laboratory conditions.[45] They generally consist of a large and bulky organic cation (e.g., tetraalkyl-ammonium, pyrrolidinium, pyridinium, 1-alkyl-3-methylimidazolium) and an organic/inorganic anion (e.g., bis(trifluoromethylsulfonyl)imide, tetrafluoroborate, trifluoromethanesulfonate, or tris(pentafluoro-ethyl)trifluorophosphate). The huge difference in the sizes of the two anions and cations hinders the formation of an ionic lattice, moreover the ions are mostly disorganised which lets the salt remain in the liquid state at room temperatures.[45]

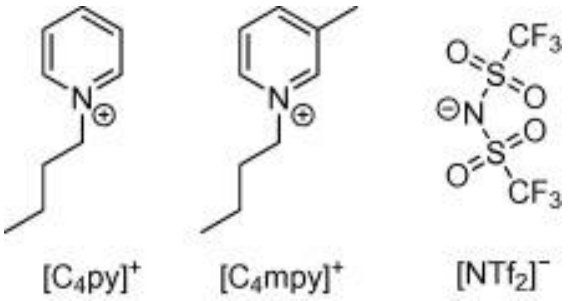

Figure 2- 7: Molecular structure of ionic liquid ([C_4mpy][NTf_2]) [45]

RTILs have unique set of properties that includes very low volatility, a greater electrochemical window, high thermal stability, and good intrinsic conductivity.[46][47][48] These properties and high structural variability make ionic liquids intriguing and promising materials for use in batteries, fuel cells and electrochemical capacitors [49][50], in medicine [15][16], and in electrochemistry for the electrodeposition of numerous metals and semiconductors [49], [53] and also for separation and extraction techniques [54]. An interesting application is the use of RTILs for the electrochemical detection of various substances in gaseous or liquid phase [55][56]–[58]. Recently, electrochemical sensors based on different ionic liquids have been used for the detection of methane [59], ozone [60], ammonia [60]–[62], oxygen [63], [64], nitrogen dioxide [60] and

ethylene [65]. In particular, room temperature ILs (RTILs) have found an increasing common use in modern gas sensor designs since they can circumvent the rigid process conditions required for certain oxidation pathways of methane analyte.[59], [66] Moreover, because of their ionic nature RTILs are effectively non-volatile at moderate temperatures; this inherent property overcomes the difficulty of dealing with solvent evaporation as is the case in AESs, making them an ideal electrolyte for sensor designs aiming to increase the device life-span. Unlike many other solid state electrolyte systems, RTILs do not suffer from electrical contact loss, and do not need significant pre-processing to get integrated into the sensor design. Lastly, RTILs are less hazardous than the common acid electrolytes used in AES systems, making them ideal candidates for widespread production and use in industry.

Although the IL based devices has gaseous detection capabilities, their use in electronic devices requires a specific design and an extra fabrication of a micro-chamber for the storage of the electrolyte in order to prevent its leakage from the sensor package. Stetter *et al*. [60], [62] used this approach, for the fabrication of ionic liquid-based amperometric sensors. Another approach used by Kubersky *et al* [67] for using gas sensors with ionic liquid is the use of solid polymer electrolyte (SPE) in which the ionic liquid is immobilized in the polymer matrix [68]–[70]. Among other advantages, this approach allowed the fabrication of a low cost, fully printed, and flexible gas sensor on a polyimide substrate.

Xiaoyi *et al* have recently shown the usage of room temperature ionic liquid to successfully develop a methane sensor for human health and safety monitoring.[59] In their research they have been able to utilize RTIL for methane detection by overcoming its disadvantage of slow diffusion by printing electrodes on a porous polytetrafluoroethyene (PTFE) substrate and passing the gas through the polymer instead of passing it through the ionic liquid. With this technique they were successfully able to utilise the advantages of RTIL while overcoming its limitations.

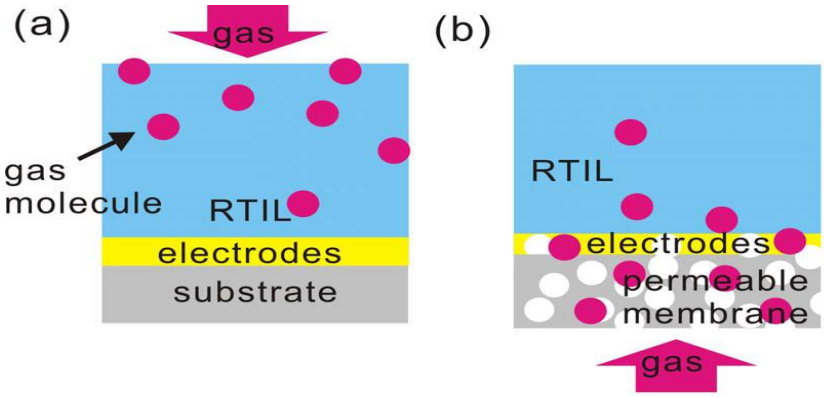

Figure 2- 8: a) Conventional sensor structure; (b) New technique used to bypass limitations of RTIL.[59]

1 – butyl – 1 – methylpyrrolidinium bis (trifluoromethylsulfonyl) imide, more commonly known as [C_4mpy][NTf_2], is one of the more frequently used RTILs in current methane sensor designs due to its good stability and conductivity. Relative to other RTILs, [C_4mpy][NTf_2] features lower viscosity and higher chemical stability[59]; RTILs are already known to suffer from low gas diffusion rates due to their inherently higher viscosity when compared to AEs which, when compounded with the low kinetic favorability of methane oxidation, result in extremely slow methane oxidation rates. This makes [C_4mpy][NTf_2] more tolerable than other RTILs as an electrolyte. Additionally, as [C_4mpy][NTf_2] is hydrophobic, it reduces the potential for sensor interference due to water splitting due to water's low solubility which acts to increase the overpotential associated with these reactions.

One convenient feature of [C_4mpy][NTf_2] is that it changes the oxidative pathway of methane.[66] Wang *et al*. [66] showed in their experimental design that by using [C_4mpy][NTf_2] interfaced with a Pt electrode, they were able to cross-validate their methane sensing platform *in situ* via an oxygen reduction reaction; since the oxidation of methane and reduction of oxygen occur at two distinct potentials, this system of reactions provides a validation platform unique to the [C_4mpy][NTf_2]-Pt system that is not available in an AE-Pt system. In their paper, they propose the following redox pathway for their sensor design:

$$CH_4 + 2O_2 \rightarrow CO_2 + 2H_2O \quad (1)$$

$$2CH_4 + 3O_2 \rightarrow 2CO + 3H_2O \quad (2)$$

$$O_2 + e \rightarrow O_2^{-\cdot} \quad (3)$$

$$2CO_2 + 2O_2^{-\cdot} \rightarrow C_2O_6^{2-} + O_2 \quad (4)$$

The side reaction (2) produces CO that would eventually poison the Pt catalyst, as is the case in most AES systems. However, due to the presence of superoxide from (3), CO can be further reduced to CO_2, and then finally to $C_2O_6^{2-}$ via (4). It is shown in their results that the final product, $C_2O_6^{2-}$ has insignificant interference with the methane signal and removes CO_2 and CO from the system cleanly. Speculation holds that it is the IL's ability to stabilize the superoxide which gives rise to this unique reaction pathway, as it is not found in any AES systems. Indeed, it can be seen that RTIL-Pt systems hold many advantages over the traditional AE-Pt systems.

2.6.3 Solid electrolyte sensor

A variety of polymer electrolytes[68][19], metal oxides[71] and inorganic salts[19] have shown significant ionic conductivities over a good temperature range. Ionic conductors can be defined as solid electrolytes (SEs), when their electronic conductivities can be neglected.

Narayanan *et al.* developed a phosphate based proton conducting SE hydrocarbon sensor.[72] The use of sodium phosphate solid electrolyte along with a hydrogenation catalyst helps detect methane at 600 °C. The sensor was developed using a two compartment cell with gold electrodes painted with Pt/CeO_2 and H_2 gas, where the solid electrolyte behaves as a proton conducting material exhibiting Nernst behavior.[72]

Zhu *et al.* have utilized alkali orthophosphates as solid electrolytes for methane sensing at higher temperatures.[73] One such solid electrolyte is sodium orthophosphate which according to Hooper *et al* acts as a versatile host for solid solution formation.[74] This solid electrolyte has the capability of functioning at room temperatures and thus can sense hydrocarbon gases like methane under ambient conditions.[74] Alberti *et al* have also successfully developed a methane gas sensor using proton conducting zirconium phosphates.[75] This solid electrolyte also shows promising results of precise and sensitive detection.[75]

There are many limitations that have been discussed in this section that motivates to continue working towards an improved sensor design. The inability of sensors to detect low concentrations at room temperatures without the loss of electrolyte and degradation is the biggest motivator for this research. Although research has progressed in the field of ionic liquid based sensors for different gases, not much has been done in the field of miniaturized electrochemical sensors for methane detection that have a longer shell life and the capacity to detect methane at ambient conditions.

2.6.4. Carbon based nanomaterials and Graphene

There has been a heavy investment in carbon based nanotechnology research in recent years thanks to the discovery of carbon based nanomaterials such as carbon nanotubes[76], fullerenes[77] and recently graphene[78]. The extensive study of carbon nanomaterials have resulted in knowing their exceptional mechanical, physical, electrical, chemical and optical properties.[76] These properties of carbon nanomaterials have garnered interest in their use in many applications such as storage devices, transistors, chemical and biological sensors and various nanocomposites.[76]

Graphene can be simply defined as a single atom thick sheet of carbon atoms which are beautifully arranged in a honeycomb type lattice.[79] Graphene, since its discovery in 2004 has proven to have plethora of application value in the fields of physics, chemistry and material sciences. Thanks to its unique crystallographic and electronic structure, it displays a multitude of exceptional properties that includes high surface area (2630 $m^2\ g^{-1}$)[80], high carrier mobility (250,000 $cm^2 \cdot V^{-1} \cdot s^{-1}$)[81], thermal conductivity (about 3000 $W \cdot m^{-1} \cdot K^{-1}$)[82], high transmittance (visible light and near infrared light absorption 2·3%)[83], excellent mechanical properties (a Young's modulus of 1×10^{12} Pa and intrinsic strength of 130 GPa)[80], good chemical stability and biocompatibility.[80]

To utilize the complete potential of these properties for various applications, a variety of different morphologies and derivatives of graphene have been developed over the years, such as graphene oxide (GO)[84], graphene nano-ribbons[85], vertically aligned carbon nanotubes[77] to name a few. The production of these derivatives from in-expensive precursors using economical processes is desirable for industrial production and applications. Recently, Tour group has

developed a technique to make porous graphene from commercial polyimide sheets. The studies conducted by the group has resulted in the formation of what is now called laser induced graphene (LIG) that contains a few layers of graphene with high electrical and thermal conductivity as well as high thermal stability.[86] Interestingly, the laser induced graphene has also demonstrated exceptional wetting properties from being super hydrophilic to super hydrophobic by using the laser in different controlled conditions.

Prior to the research on laser induced graphene, the carbonization of PI was reported to have a porous structure by exposing it to ultraviolet light[87], but unfortunately graphene could not be disclosed and no studies on the exact parameters required to sustain the various different morphologies have been conducted. It was realized that a critical fluence point of ~ 5 J/cm^2 was needed to begin the carbonization process when changing the total radiation per unit area on the PI.[77] It was also found out that when a commercial CO_2 laser raster mode was applied, a vertical growth with a height of about 1 mm of a forest of laser induced graphene fibres was obtained.[77] This led to further variation and modifications in the conditions and settings that led to development of laser induced graphene.

2.6.5. Electrode Fabrication Techniques

An important part of studies based on electrochemical sensors focus on fabrication techniques and their optimization. It is expected to achieve a few deliverables by the fabrication method; lower costs, simple and rapid processing, and accessibility of the technique. The fabrication process can be categorized into two major techniques; the direct and indirect deposition of electrode material on the surface of a substrate.

2.6.5.1. Photolithography Technique

Photolithography is widely studied as a micro fabrication method for electrochemical sensors.[88], [89][90] The electrode material is fabricated onto the photo-resist material, and the patterned design of electrode is achieved through lifting off the photoresist material from the design. This technique is cost effective in compared to the general lithography technique and is somewhat straightforward. Although it is simple, it requires an extra step to remove the photo-resist material. Therefore it is not an ideal fabrication method for simple, cost effective generation of electrodes. A lot of micro-scale components can be fabricated by deposition of material layers,

photolithographic patterning, and etching to create the desired profiles. MEMS is generally based on micro-fabrication using photolithographic technique which is made up of components between 1 - 1000 micrometers in size, resulting in MEMS devices with the size ranging from 20 micrometers to millimeters. [90] Many actuators and sensors such as micro-motors, micro-pumps, temperature and humidity sensors are applied to micro-device for implementation of their functions.

2.6.5.2. Screen Printing Technique

Screen printing technology is one of the most usable and highly developed technology given its existence for a thousand years and the years of research that has led to this technology being utilised for electrode printing and other electronic applications. The biggest revolution in this technology came with the advent of screen printing techniques on flexible substrates by the development of polymer based inks which allow low curing temperatures to be compatible with plastic substrates.[91]

This technology has created new and exciting opportunities that can be applied to electrochemical techniques for various analysis and detection at a commercial scale. Due to their cheap and mass production capabilities with consistent chemical performance, screen printed electrodes may be most useful for electrochemical sensors for *in situ* analysis because of their low power needs, linear output, fast response, high sensitivity and the ability to operate at room temperatures.[91] Also, it is quite easy to change the surface of screen printed electrodes to fit multiple purposes as required according to the use. Already many different modifications of screen printed electrodes exist for various environmental analysis such as noble metals, inorganic nanomaterials, DNA sequences and enzymes to name a few.[91]

2.6.5.3. Inkjet Printing Technique

Inkjet printing has been widely used for printing electronic systems recently. Low viscosity inks can be used with the help of this technique. This is important as it negates the use of binders and allows for the formulation of polymer inks that only contain active material and solvents.[92]

This technology has seen an extensive growth in the last three decades not only due to the growth in printer requirements at office, home and industrial level but also due to an increasing interest

with using thin polymer films for coating[93], in the fabrication of solar cells[94] and three dimensional structures including electrodes for sensors[93]. Some of the advantages of inkjet printing are its easy access, cheap cost and compact sizes. By using this technology, conductive ink capable of replacing carbon and colour dye ink solutions can be easily used to layer a conductive film on a substrate such as paper or a polymeric/ metal sheet.

More recently, a lot of research has been done for development of conductive inks for inkjet printing for metallic materials such as copper, silver and polymers.[94] Although most of them have not been successful as they have limitations such as poor conductivity, surface oxidation and not an efficient electro-migration. Carbon nanotubes based inks have recently gained traction as they have been able to provide high conductivity without the issues of surface oxidation or the need to replace polymers or use metallic pastes.[93]

2.6.6. Laser irradiation technique

Laser irradiation and patterning is a simple, and can be a faster technique for fabrication as an alternate to the lithographic fabrication process. A laser source is utilized for source of energy to ablate or remove the respective polymer material and create a desired patterned conductive surface. More recently, laser irradiation has been experimented on carbon precursors and in the reduction of graphene oxide on flexible substrates to cause graphitization.[95]–[97][98], [99][100]–[103] This is a simple process as it only needs a laser source and an operational chamber for laser irradiation in order to prevent any possible laser scattering. There are different laser that are available and can be utilized for this process, for example femtosecond pulsed laser[104], nano- and picosecond pulsed laser[100], continuous wave laser[99][101] and the laser irradiation have demonstrated at a various range of wavelength laser, ultraviolet, blue light[104], infrared range [99], [101] and visible range laser sources.[95][96], [97] The femto, nano and picosecond lasers are standard available laser sources; the cost of the equipment is the biggest concern hindering the use of this fabrication on a larger industrial scale as well as the low throughput. A better alternative, CO_2 laser-based etching/cutting machines are inexpensive, widely available and can pattern in less time due to the larger cross-section of the sample hit by the laser in a single pass due to rapid photothermal heating. These lasers are widely used in many applications in industries for cutting and marking wood, metal, and polymer materials. Hence, laser irradiation can become accessible and scalable via this type of laser source.

2.6.7. Materials for Laser irradiation Technique

One of the focus in this research has been to utilise laser irradiation technique for fabrication of interdigitated electrodes for the electrochemical sensor. Several studies have promoted polyimide as a promising carbon precursor because of its ability to carbonize easily through laser irradiation and provide a high electrochemical performance compared to graphene oxide. Polyimide is an amalgamation of many heterocyclic groups in its polymer structure. Therefore, it displays the ability to be graphitized by laser irradiation. Similar characteristics are also observed in polyetherimide (PEI), another imide group polymer.[86] However, laser irradiated polyimide has been reported primarily with the use of an aqueous-based electrolyte, this shows the ion accessibility of these carbon structures is limited or else large molecule electrolyte compounds such as ionic liquid and organic electrolytes would perform similarly. Aqueous based electrolytes are well known due to their smaller sized ions; however, they have a limited voltage window between 0-1 V due to a water splitting potential around 1.2 V. On the other hand, organic and ionic liquid electrolytes that includes room temperature ionic liquids can provide a wider voltage window of 2.5 V and 4 V respectively[105]. The combination of polyimide via CO_2 laser irradiation patterned into interdigitated architecture, and aqueous-based electrolyte in the gel formed has resulted in one of the highest reported specific capacitance in recently studied literature.[104] Literature has reported up to 31.9 mF/cm^2 at a 0.05 mA/cm^2 current density following a plasma treatment which improved the contact between the pores and ions at the interface of the electrolyte and the electrode. [104] Plasma treatment improves the surface hydrophilicity of the polyimide after laser irradiation; polyimide tends to exhibit higher hydrophobicity after laser irradiation.[106]

Chapter 3: Experimental Methods

3.1. Preparation

3.1.1 Sensor geometry and Fabrication

The laser-induced carbonization of electrodes onto flexible Kapton tape substrates is done to create an interdigitated design. This laser printing (using CO_2 laser) of electrodes is a flexible, effective and inexpensive system. The interdigitated design is obtained via laser ablation of a polyimide-coated Kapton film. This process is done using a BOSSLASER LS-1416 machine and accompanying software. The laser induced graphene with controlled scribing with a computer software, helps to etch desired geometries. An 18 x 21 mm interdigitated pattern is scribed using the CO_2 laser (Figure 4-1 (a)). The fabrication is done at a speed of 25mm/s with an 11-12 % of total power and at a scan mode with two scans done in X orientation. The fabricated geometry is further analysed using SEM imaging (Zeiss FESEM Leo 1530, at 5 kV), optical microscopy and Raman analysis conducted by a Horiba Raman Division Olympus BX 41 instrument with a 532.06 nm laser.

3.1.2. Palladium (Pd) nanoparticle (NP) synthesis and loading

A simple recipe is followed for synthesizing the Pd NP. The NP are formed from the Pd nitrate salt using a technique followed by Azhari *et al* [107]. For this preparation, 5 mM sodium citrate (Sigma-Aldrich) and 0.025 mM tannic acid (Sigma-Aldrich) were dissolved in 100mL of milli q water. This solution was heated to 70 °C while continuous stirring. 8 mL of $Pd_2(NO_3)_3$ (25 mM) solution was then injected into the sodium citrate/tannic acid solution. After injection, the reactor is maintained at the same temperature for 15 min to complete the reaction. The hydrodynamic diameter of resulting Pd was examined by dynamic light scattering (DLS, Zetasizer Nano-ZS90, Malvern) after diluting the dispersion to 0.1 mg/mL. During the synthesis it is realized that the control of temperature is very important for formation of a homogeneous well dispersed nano size particle formation and prevent them from aggregation. A temperature lesser than 70 °C leads to formation of aggregates of Pd nanoparticles, which is not desirable, hence the preparation should be conducted above this minimum required temperature.

The Pd NPs are dispersed in an aqueous solution. Due to the hydrophobic nature of the electrodes, the deposition of NPs cannot be done directly. The following technique is used to deposit the NPs through a solvent exchange with isopropyl alcohol:

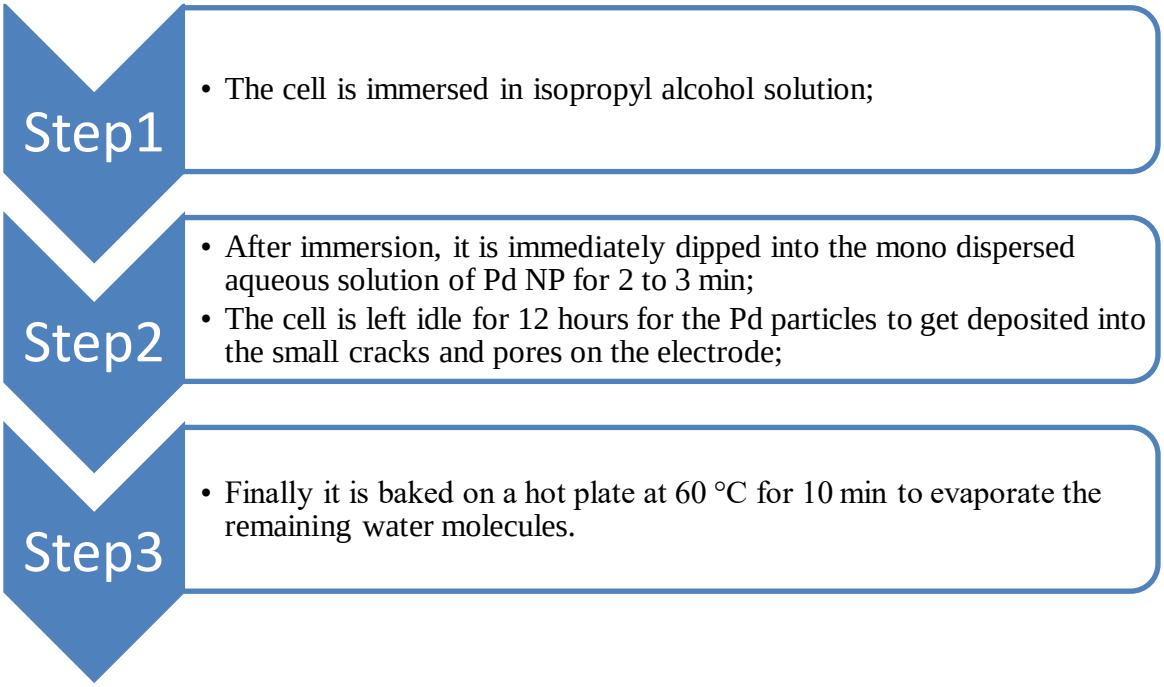

3.1.3. Application of Ionic liquid using solid polymer

Non-volatility of the electrolyte is key to preventing the sensor from drying out during operation. Ionic liquids (IL) are salts which are liquids at room temperature and due to their strong ionic bonding, they are not volatile. It was recently shown that methane is converted electrochemically to CO_2 and H_2O at room temperature when an ionic liquid electrolyte is used[55]. The IL 1-ethy-3-methyl imidazolium bis (trifluoromethylsulfonyl) imide is used as an electrolyte. Although, the IL helps with the issue of non-volatility and detection at room temperature, one major issue constraint is the issue of holding the electrolyte on a flat surface without losing or getting the IL contaminated. To resolve this issue the IL is imbibed in a polymeric substrate. Polyvinylidene fluoride (PVDF) is used for this purpose. A weight ratio of 1 part PVDF, 1.5 part IL and 3 parts N-methyl 2 pyrrolidone (NMP) solvent is used to develop the IL electrolyte imbibed in a porous solid polymer[70]. The mixture is heated at 75 °C for 2 min until a gel like material is formed which is then applied onto the interdigitated array with the help of a glass rod. The system is

allowed to dry at room conditions for 24 h where all the NMP solvent gets evaporated and a white thin layer of polymer coated IL electrolyte is formed over the interdigitated network.

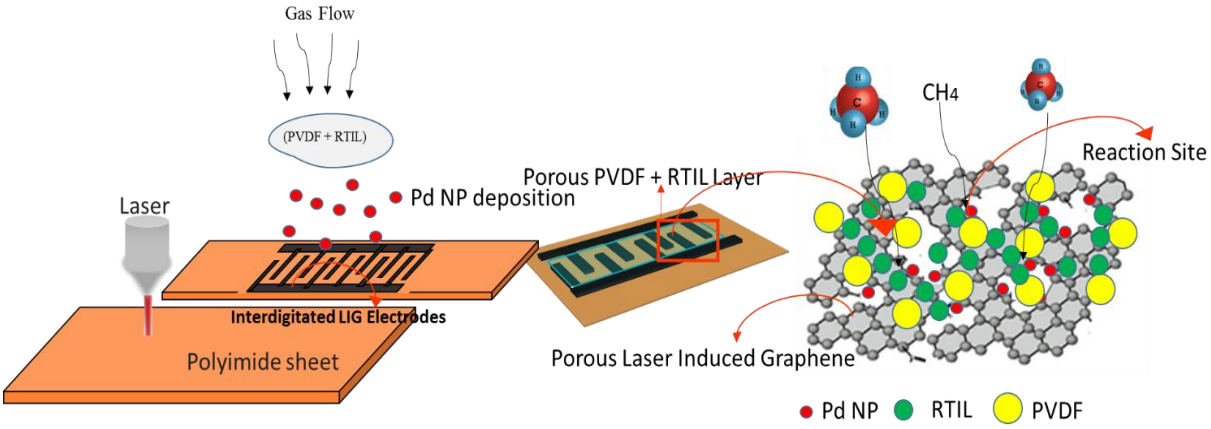

Figure 3- 1: Schematic of the fabrication process of the methane sensor. The image shows the step by step process of the fabrication process. A 3 dimensional model shows the deposition of Pd NP and the layering of the solid polymer electrolyte. A further insight shows the reaction and assembly at the molecular level.

3.2. Test chamber design and setup

During the initial stages of this project, the biggest challenge was to create a setup that is able to hold methane in a sealed space and can help detect any sensitivity response corresponding to the sensor. The testing was achieved using a batch cell setup (Gen I) where the sensor was placed in a glass chamber with two inlets for air and methane, and a connection outlet connected to the potentiostat for the measurement. This setup allowed to hold methane under partial vacuum for a limited time period to detect any sensitivity response from the sensor. The image in Figure 3-2 consists of a plexi-glass chamber with dimensions 20 cm x 15 cm x 10 cm with two inlets on top to maintain methane inlet. The chamber is filled with air, and a calculated volume of methane is injected through one inlet using a syringe of volume 60 mL, whereas the other helps to remove the excessive air due to increase in volume. A vacuum pump is connected to maintain the pressure. The air entered is regulated using a flow meter. The concentration of methane is measured using

simple volume by volume (volume entered using syringe over volume of entire chamber) calculation to find the ppm of methane inside the chamber.

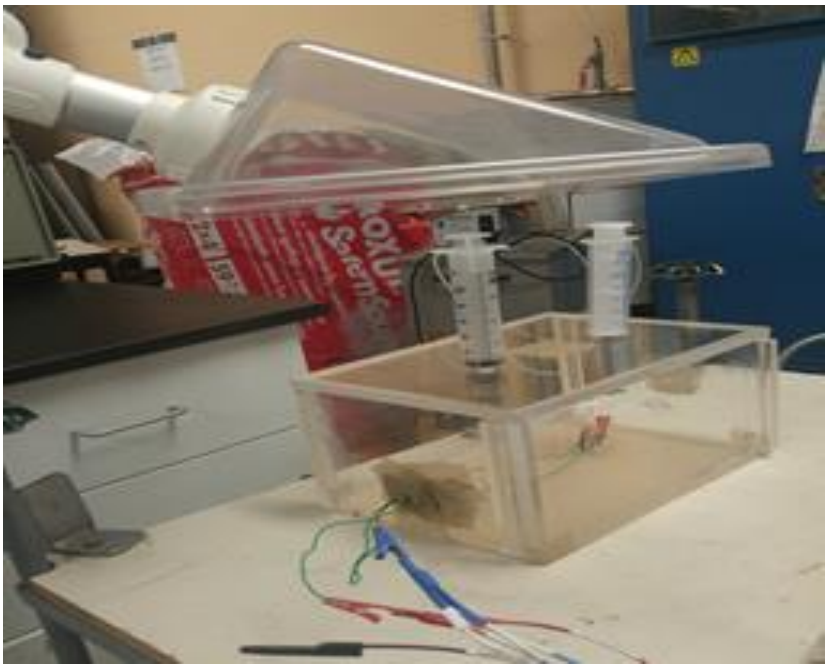

Figure 3- 2: Gen I batch testing chamber

The Gen I setup design helped in initial study and analysis of the sensor and to determine whether the sensor is responsive to different concentrations of methane. The major flaws with this setup were that the exact concentrations of methane in the chamber at any given time could not be determined accurately. Moreover, it is hard to control leaks and vacuum in a big setup like this. A new testing chamber was required, where the concentrations could be easily controlled and monitored. For this purpose a Gen 2 chamber was setup, which tested the sensitivity of methane in a flow cell setup. The image in Figure 3-3 shows the flow cell setup. An air tight container is used and fittings are created for inlet and outlets. Air from the pipeline is connected to the inlet using a regulator and a flow meter to control the flow-rate of air entering the chamber. A syringe pump is filled with methane and connected to the chamber using a non- reversible valve. The volume and flow rate of methane can be accurately measured with the help of the syringe pump. There are two outlets, one that connects the system to the potentiostat (BioLogic, VMP3B-100, 100A/5V) and the other that lets off the off gases. With the help of this setup the response at

different concentrations of methane can be known with less error. Some disadvantages of this setup are the manual handling of gases and control which induces error and uncertainty. Also, very small quantities of methane cannot be measured accurately with the help of this setup.

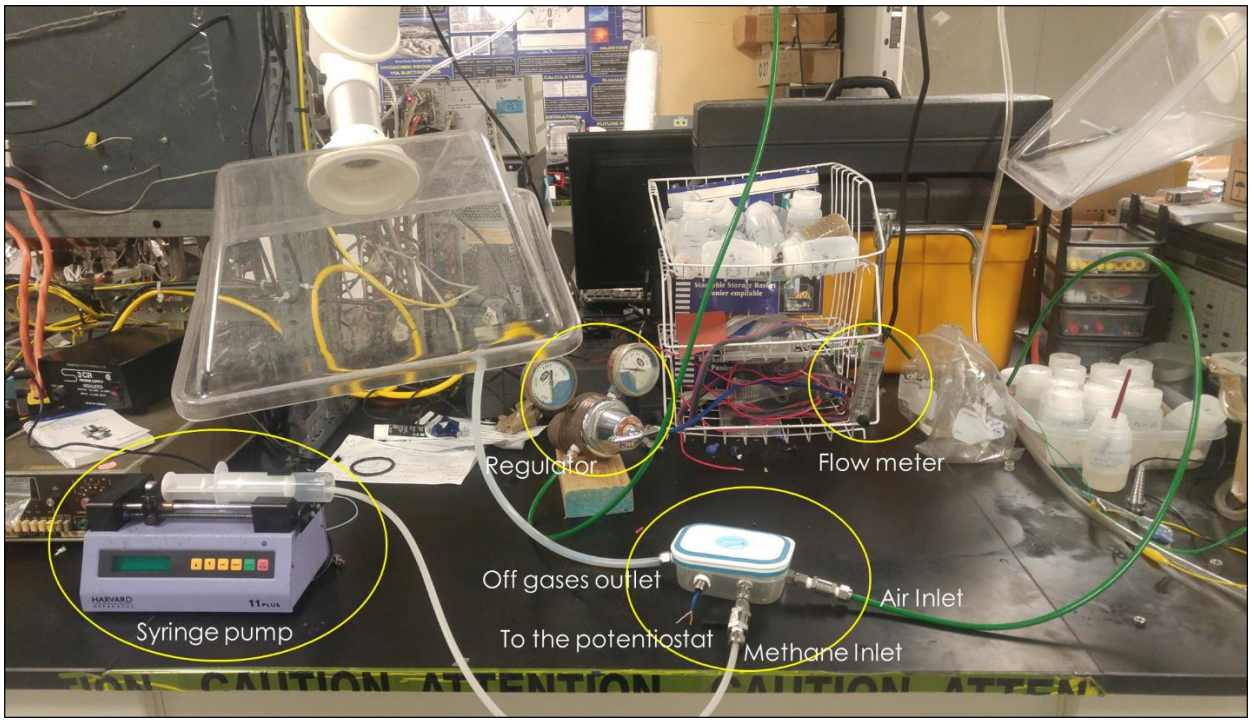

Figure 3- 3: Gen 2 Flow cell chamber

A Gen 3 flow cell test chamber is setup which uses mass flow controllers to measure and inject the gases. The off gases can also be analysed with connecting the setup to a FTIR (MKS, MultiGas 2030). The fabricated sensor is tested for sensitivity by injecting methane in a controlled and sealed self-designed chamber. With the use of mass flow controllers the dry air (Praxair) and methane (500 ppm in N_2, developed by Praxair) is mixed and sent into the chamber. Concentrations varying from 5 ppm to 100 ppm can be achieved using the mass flow controllers (as shown in Figure 3-4). The system is first flushed with nitrogen with flow rate of 200 mL/min. The nitrogen flow is then closed and the system is flushed with dry air with flow rate of 200 mL/min. After an interval of 5 minutes, the air flow rate and methane flow rate are adjusted using MFC MKS 2012 software to provide the required concentration in the chamber (concentration date is available in Appendix C, Table C-2). The mass flow controllers work within air flow rate range of 250- 10000 ml/min. This

limits the experiments to a minimum methane injection concentration of 5 ppm ± 0.1 ppm. After the experiment is conducted, the system is again flushed with nitrogen for about 2 min and then the same procedure is repeated for the ongoing experiments. The sensor is placed inside the chamber, with contacts connecting the electrodes to a portable pocket potentiostat (pocketSTAT, IVIUM Technologies), with a voltage input capacity of 5 ± 0.2 V dc, maximum input current of 0.5 A and maximum power of 2.5 W. The outlet is connected to a Fourier Transfer Infrared Spectroscope (FTIR) for further analyzing the off gases and to ensure the concentration levels inside the chamber are maintained. For the FTIR analysis, the system is flashed for 1 hour with 500 mL/min of nitrogen prior to the experiment. The IR valve is closed and the system is allowed to stabilize for 20 min. Air flow at 170 mL/min is passed while ensuring that the silica gel is bypassed. The temperature is ramped from 25 °C to 150 °C. The system is now prepared for analysis.

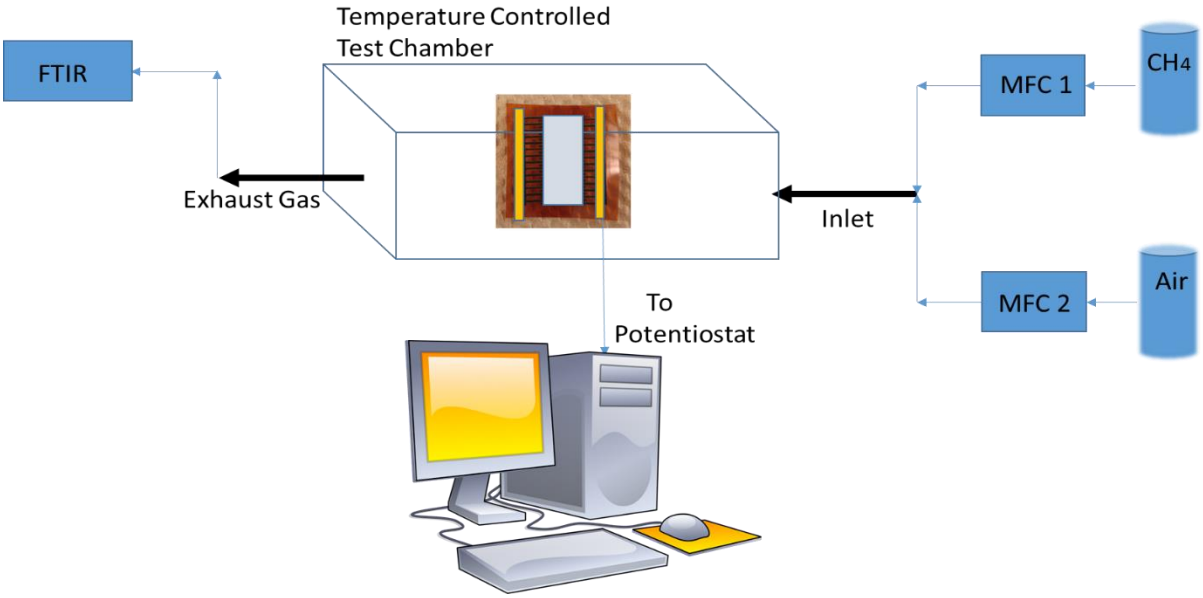

Figure 3- 4: Gen 3 Flow cell chamber design sketch

3.3. Electrochemical Impedance Spectroscopy Experiment

To conduct the EIS analysis, the impedance analyzer was setup to collect data at 100 Hz to 100 KHz with a constant potential of 0.6 V. In order to infer the resistance values from the plots, a fitting software to fit the curves was used and the approximate resistance (Rd2) was obtained. This

was achieved by using Z-fit tool. It is commercially available to perform fitting analysis by assigning the circuit elements that could possibly be the best circuit to represent the curve.

3.4. Lifetime Analysis Experiment

In order to conduct this experiment the sensors are subjected to 30 ppm of methane at a constant potential and for a duration of 180 s. The current at the 90% interval of time is recorded as the sensor response for the particular day. The sensor after testing is stored in a desiccator in order to avoid contact with any interfering gases that might be present in the laboratory.

3.5. Materials

For Palladium nanoparticle synthesis, $Pd_2(NO_3)_3$ salt (Dihydrate, Sigma Aldrich, 40% Pd Basis), Sodium Citrate (Sigma Aldrich) and Tannic Acid (Sigma Aldrich) are used. For solid polymer electrolyte, PVDF (Sigma Aldrich), 1-ethy-3-methyl imidazolium bis (trifluoromethylsulfonyl) imide (97%, Sigma Aldrich) and N-methyl 2 pyrrolidone (99.5 %, Sigma Aldrich) are used. Commercial Kapton™ polyimide film (0.005" thick film, semi-clear amber) were obtained from McMaster-Carr for interdigitated electrode fabrication. Gases, Air (Dry air supplied from University of Waterloo), Nitrogen (99 %, Praxair), Methane (500 ppm methane, 99.5 % nitrogen, Praxair, A3, 0.868 m^3 vol cylinder), Propane (500 ppm propane, 99.5 % nitrogen, Praxair, AS, 4.012 m^3 cylinder) and Ethane (500 ppm ethane, 99.5 % nitrogen, Praxair, AS, 4.012 m^3 cylinder) were used.

Chapter 4: Results and Discussion

This chapter is being prepared for publication. Most of the experimentation work in this section has been conducted by me. The setting up of flow cell system, calibration of mass flow controllers and *in situ* FTIR testing were done with the considerable help of Mr. Yichen Zhuang (PhD candidate with Dr. David Simakov). Ms. Irene Lau (MASc candidate with Dr. Michael Pope) assisted in doing SEM imaging.

4.1. Chapter Introduction

Methane is the primary component of natural gas. As a result of mining and defects in the distribution network, methane emissions occur throughout the oil and gas industry. This corresponds to the largest anthropogenic source of the potent greenhouse gas (25 times more potent than CO_2) and leads to a significant loss in revenue for the oil and gas industries: 60% of methane loss is due to fugitive release, out of which a major percentage is due to transmission lines (pipelines).[1] These leaks are currently challenging to identify or detect due to the expansive nature of the distribution network using the currently available optical, semiconductor or combustion based sensors. Such sensors are expensive and not viable for detecting minor leaks.[2] Apart from natural gas pipelines, methane sensors also find applications in agriculture, waste management, landfill monitoring, lab, hospitals and also at home for maintaining health and safety. The widespread use and production of methane also increases its magnitude of being a hazard and creating safety issues. The use of methane sensors becomes vital in these situations.

The development of inexpensive, low-power and selective electrochemical sensors could provide a cost-effective means to carry out distributed sensing over the entire network. While high temperature (> 500°C) solid-state electrochemical methane sensors have been demonstrated in the past using Yttria stabilized zirconia as a solid-state electrolyte,[40] the requirement of high temperature makes them impractical for use. More recently room temperature ionic liquids (RTILs) have gained traction for use in gas sensor design due to their ease of processing and, more importantly, their effective non-volatility;[108][109] Furthermore, the structured ionic phase can solvate or complex with a variety of solutes including methane – opening up a room temperature oxidation pathway for methane as discussed by Wang et al.[110][59] While promising results have been demonstrated using RTILs, previous designs have run into challenges with slow diffusion of

gases through the fully dense liquid films formed [111] or have been carried out by sparging the gases through a bulk ionic liquid.[5] To overcome this problem, to some extent, Mason's group has come up with an electrode design where gold electrodes were patterned by photolithography onto a porous polytetrafluoroethylene substrate (PTFE).[112] In this case, the methane could penetrate through the membrane and to the RTIL/gold interface instead of diffusing through the thin RTIL film covering the electrodes. Their sensor achieved a sensitivity of 0.31 μA/% methane (31 pA/ppm) with a 0.28% (2,800 ppm) detection limit for an ~1 mm diameter working electrode. This miniaturized system demonstrated improve performance over a previously reported organic solvent/Pt-black based system with a sensitivity of 0.5 μA/% methane (50 pA/ppm) with a detection limit of 0.5% (5,000 ppm). While promising, the detection limits of these electrochemical sensors is far from the sub-ppm values desired by industry and achievable by more advanced but expensive spectroscopic methods.[113]

One way to improve the sensitivity and detection limits of electrochemical methane sensors is to create a higher surface area electrode/electrolyte interface which is accessible by the gas phase analyte. It has been shown possible to create high surface area electrodes by techniques such as screen or ink-jet printing of high surface area carbonaceous materials like graphene[114] or carbon nanotubes.[115] More recently, a simpler approach to create patterned high surface area carbonaceous arrays, compatible with rapid prototyping, has been demonstrated by Tour's group. They demonstrated that CO_2 laser cutting/etching system could be used to spatially convert polyimide (Kapton) films into a material which they referred to as laser-induced graphene.[86] These laser systems are inexpensive and used industrially for various laser etching and cutting applications. Furthermore, each pass of the laser is capable of carbonizing ~100 μm width lines and is thus amenable to medium throughput manufacturing – creating a ~cm^2 device within seconds. Over just the last few years, this technique has been used to create a variety of devices including flexible supercapacitors,[116] water-splitting cells,[117][118][119] biosensors,[18][19] piezo-resistive sensors,[122] and robust superhydrophobic surfaces and membranes.[123]

While electrochemical sensors for liquid-phase analytes have been demonstrated,[67] gas sensors pose a challenge because liquid electrolytes typically fill the pore space and inhibit gas diffusion to the electrode (and catalyst, if one is required). Since RTILs with bis(trifluoromethylsulfonyl)imide (TFSI) anions have been shown to facilitate the room

temperature electro-oxidation reaction at Pt electrodes,[124] we strived to develop a porous and pseudo-solid state system from such RTILs. Kubersky et al., recently demonstrated that a porous, solid polymer-electrolyte (SPE) could be formed by casting a solution of polyvinylidene fluoride (PVDF) with 1-ethyl, 3-methylimidazolium bis(trifluoromethylsulfonyl)imide (EMImTFSI) in N-methylpyrrolidone (NMP) onto planar, patterned Pt electrode substrates. The morphology of the SPE layer could be tuned from micron-sized fractal aggregates of SPE to larger, connected spheroidal structures caused by differences in the nucleation and crystallization rates during drying.[70] Aerosol-jet printing of a CNT film as a working electrode (WE) on top of the porous SPE layer resulted in an NO_2 sensor with high sensitivity and a low detection limit for NO_2 gas.

Building off of these advances in materials development and sensor design, herein, we demonstrate an electrochemical methane sensor based on LIG electrodes decorated with a nano-palladium (Pd) catalyst with the meso/microporous network formed by the LIG imbibed with the SPE based on the PVDF/EMImBF$_4$ system. The porous electrolyte network that forms within the porous electrode structure leads to fast response times of less than a minute and enables a high contact area between electrode/electrolyte/methane. The flexible, planar device achieves a sensitivity of 1.1 μA/ppm of methane which is only ~2 cm^2. This is a six order of magnitude improvement over previous approaches and enables a detection limit of ~ 500 ppb. The cell operates at only ~0.5-0.6 V which minimizes power output and improves selectivity by avoiding side reactions that might occur at higher voltages. We find the sensor is insensitive to nitrogen, oxygen gases but the response is affected by relative humidity and similar gases like ethane and propane. This is likely due to water being a reaction product, along with CO_2 which was verified by off-gas analysis, confirming the RTIL-mediated oxidation pathway proposed by Wang et al.[66] The fabricated sensor is inexpensive and amenable to medium throughput manufacturing with a sensitivity and selectivity that might allow the technology to compete with laser-based spectroscopic systems and making distributed pipeline/infrastructure monitoring an economically feasible option.

4.1. Laser scribed electrodes

As shown in Figure 2, a flexible interdigitated electrode is formed upon laser irradiation of the commercial Kapton^{TM} film. The laser irradiation locally carbonizes the polymer resulting in

porous, high surface area and conductive lines with some properties reminiscent of graphene. For this reason, it has been termed laser-induced graphene (LIG) by Tour's group [86]. As illustrated in Figure 4-1a, interdigitated electrodes with dimensions of 21 x 18 mm were fabricated. Such a pattern takes 1 min 20 sec to write using a simple system often marketed to industry and hobbyists and highlighting its usefulness for rapid prototyping. The electrode geometry can be easily changes with a few clicks, unlike techniques based on photolithography. The interdigitated electrodes used for this work consists to two bus bars (side electrodes) with dimensions 21 x 1 mm and 14 fingers with dimensions 13 x 0.4 mm. The overall surface area covered by electrodes on the polyimide sheet is $2cm^2$ with an error margin of 0.1 cm^2.

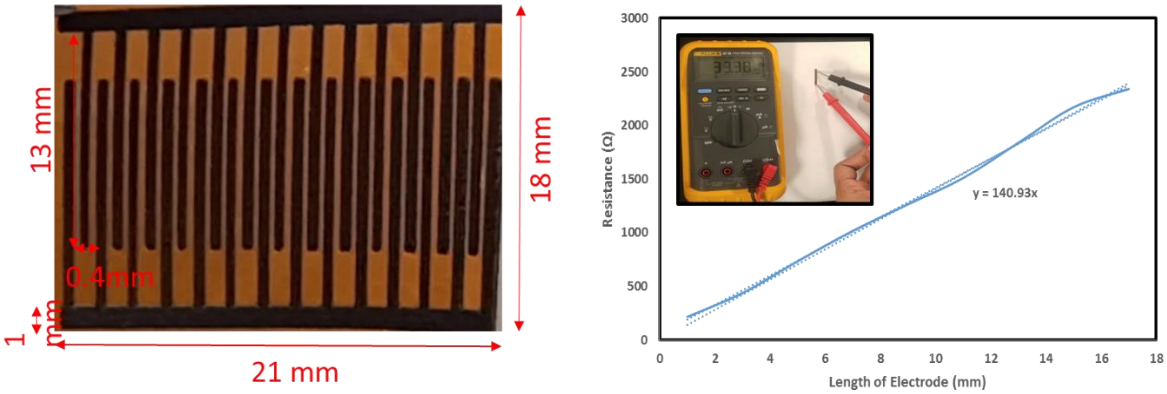

Figure 4- 1: (a) Image of the laser induced graphene interdigitated electrodes with dimensions; (b) Image showcasing the resistance measurement along the electrode line.

The resistivity of the laser induced graphene electrode is estimated to be 0.04 Ω cm (Analysed from SEM image of the electrode with an error of 1 um shown in Figure 4-1b). The conductivity of the material is estimated to be 23.75 S/cm which is similar to what has been reported by others (20 – 26 S/cm) [86]. The high conductivity of the electrodes helps affirm the performance of the sensor.

The laser scribed electrodes have good flexibility. They can be easily conformed or flexed. The flexibility of the structure has been tested with using cylinders of different radius and the electrode strip being stuck around them as shown in the image in Fig 4-2. The image shows the ability of the interdigitated structure to bend around the curvature of four different sized cylinders. This is

important as most sensors currently in use (optical, catalyst combustion sensors) have a very rigid structure, with the need to create a special structure to mount them. The flexibility of the sensor could be vital in operations such as detection of fugitive emissions in natural gas pipelines. Pipelines have a variety of shape and sizes. A sensor that can be easily attached to any structure would be beneficial and cost effective as well.

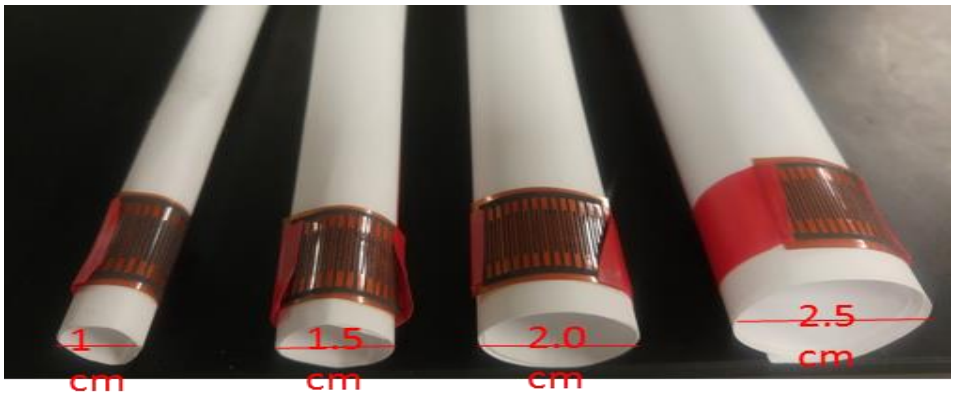

Figure 4- 2: A demonstrative image showcasing the flexibility of the laser induced graphene electrodes by flexing them around cylinders of different radii

Raman analysis was conducted by an Olympus BX 41 instrument with a 514 nm laser. The Raman spectrum of the electrode material is shown in Figure 4-3. The characteristic D, G and 2D peaks are observed at 1349.39 cm^{-1}, 1583.02 cm^{-1} and 2699.80 cm^{-1}, respectively. The spectrum obtained is consistent with the results of similar LIG work in published literature.[86], [99], [116], [125] From the narrow G peak, it is clear that there is a significant graphenic region of sp^2 C atoms. The specific position of the G peak is also highly sensitive to the number of layers present in the graphene, ranging from single layer graphene at a peak position of 1587.1 cm^{-1} and graphite possessing a peak position of 1581.6 cm^{-1}. [126], [127] According to the following empirically derived equation, the estimated number of layers is on average, 3.29:

$$\omega_G = 1581.6 + \frac{11}{1+n^{1.6}} \quad , \qquad [128]$$

where ω_G is the position of the G peak and n is the number of graphene layers.

The intensity of the D peak is reflective of the resonance due to scattering in the presence of a defect, such as the bending of sp^2. However, the ratio of I_D/I_G suggests an abundance of

nanocrystalline graphene domains. [126] The crystallite size was determined to be ~22 nm by the relation,

$$\frac{I_D}{I_G} = \frac{C(\lambda)}{L_a}, \qquad [126]$$

where C(λ) is ~4.4 nm for a 514 nm laser and L_a is the crystallite size of the graphenic domain. This is by the assumption that in the variation of I_D/I_G with L_a, the LIG lies in the regime of nanocrystalline graphite as opposed to the regime of amorphous carbon [126].

The 2D peak can be fitted with one peak at 2700 cm^{-1}, similar to single layer graphene. Without the splitting of this 2D peak, it is an indication that graphite is not present, but graphene. [129] The peak has an intensity of approximately half of the intensity of the G peak, which suggests that there are some stacking of layers of graphene, consistent with the calculated estimated layers of graphene above.

The surface morphology of laser induced graphene electrodes are investigated by scanning electron microscopy (SEM). The images (Fig 4-4 a, b and c) display the structure of the electrodes and showcases the pores in the electrode structure. Figure 4-4(a) is an image of the finger electrodes. From the image the pattern of laser being operated to fabricate the electrodes can be observed. The laser runs from in a horizontal (x-direction) orientation rather than a vertical (y-direction) orientation. The lines in the electrodes corresponds to re-run of the laser beam after first round of laser ablation. The laser is run twice in order for smoother fabrication of the electrodes as seen in the image in figure 4-4(a).

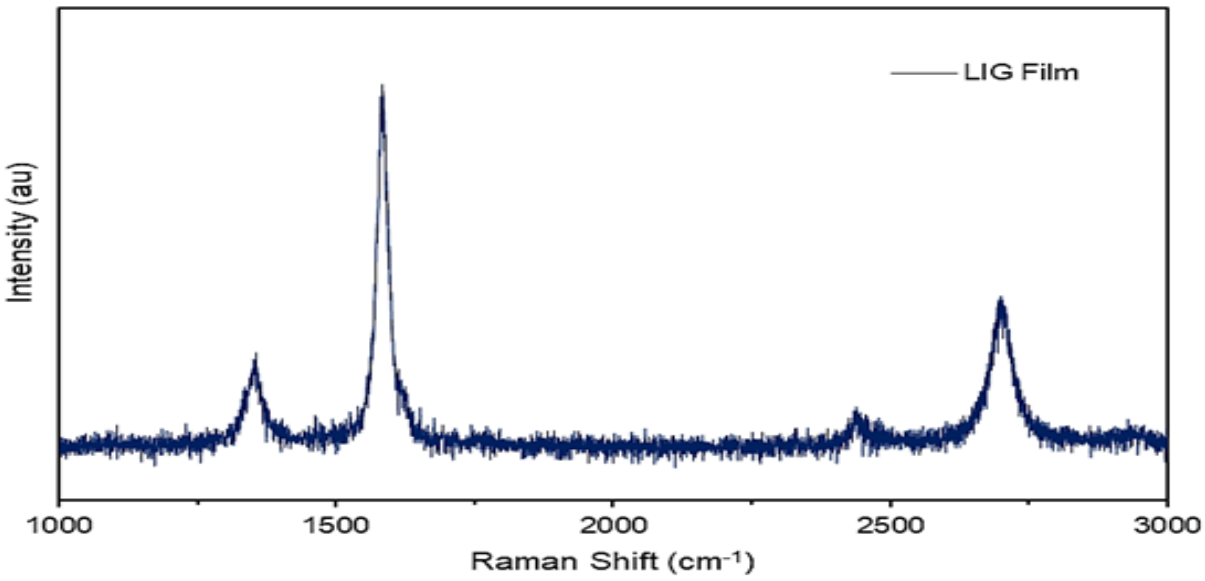

Figure 4- 3: Raman spectra of the LIG film on Kapton substrate.

Figure 4-4 (b) is a 10x magnification of the electrode layer as seen under an optical microscope. The image distinguishes between the polyimide sheet (golden yellow) and the LIG electrode fabricated on it. The image helps to understand the smooth formation of the electrode lines.

Fig 4-4 (c) is an image of the macro and micro porous structure of the laser induced graphene electrodes. The size of the macropores pores as measured with the help of SEM image is in a range of 20 to 50 μm while micropores and mesopores also exist, as confirmed by gas adsorption, leading to surface areas as high as 150 m^2/g.

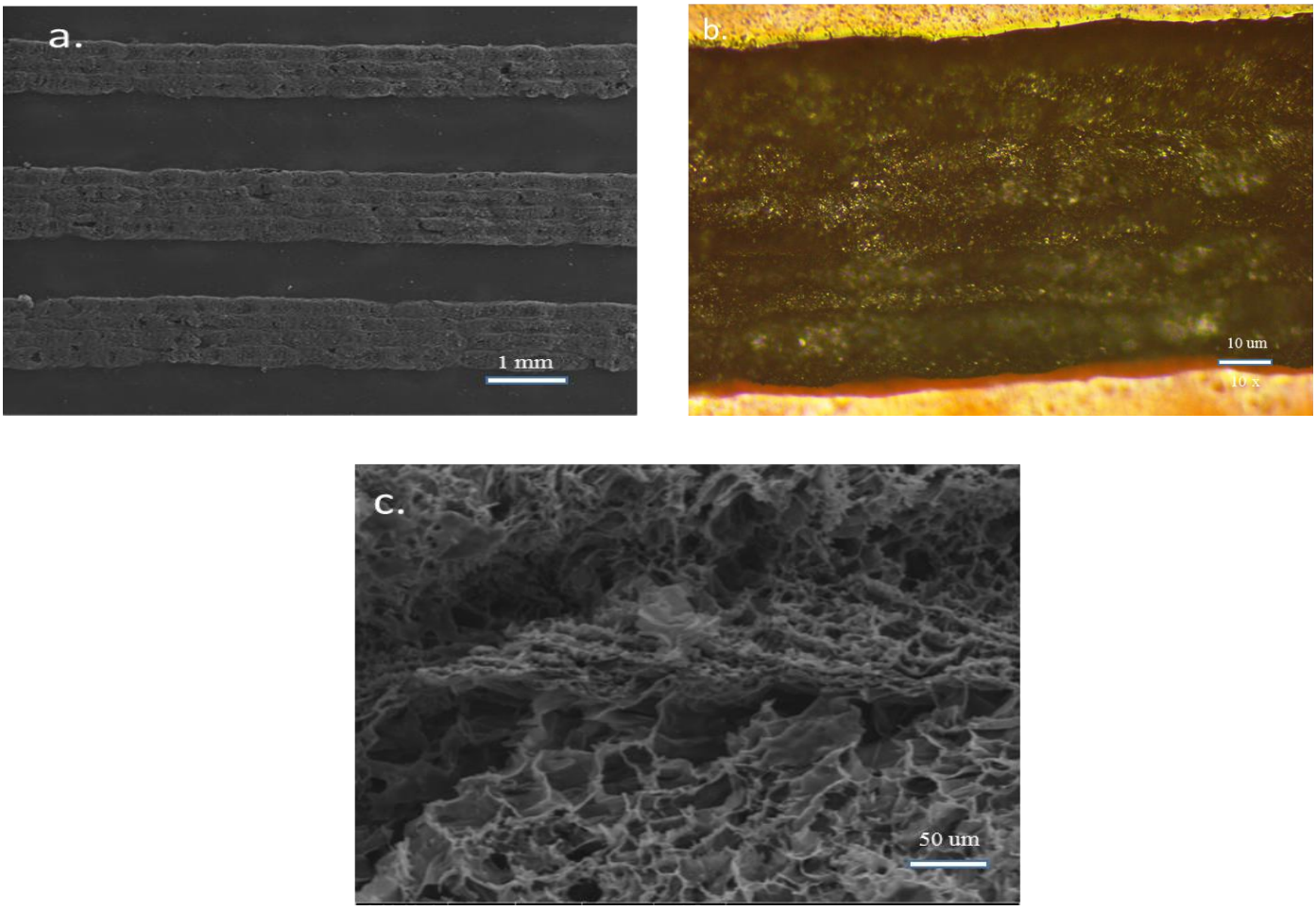

Figure 4- 4: Optical and SEM imaging of laser-induced electrodes. (a) Top view SEM image of the electrode lines illustrating their uniformity. (b) Optical microscope image of one electrode line showing laser induced graphene (black) on the Kapton^{TM} sheet (yellow) (c) Image of the porous electrode structure from the top view.

4.2. Characterization

Pd nanoparticles were chosen as the electrocatalyst for the methane oxidation reaction. As shown in Figure 4-5(a) DLS was used to measure the approximately hydrodynamic radius of the Pd nanoparticles to be 72 nm prior to imbibing the Pd solution into the porous LIG electrodes. As shown in Figure 4-5(b), after imbibing the dispersion into the electrode by a solvent exchange approach, the Pd nanoparticles were found by SEM to distribute within the porous network. While some micron-sized aggregates are clearly visible as bright contrast in the backscattered electron

(BSE) image, and likely an artifact of the drying procedure, many particles are sub-micron and likely composed of single Pd particles supported by the carbon of the LIG. EDS was used to confirm that these particles were indeed Pd and EDS mapping over the width of a finger was used to demonstrate the uniform distribution over larger length scales as shown in Figure 4-5(c) The mapping results indicated that the electrodes were composed of ~2 wt % of Pd. However, the total amount of Pd expected to be deposited into the fingers is 0.108 mg/cm^2 of electrode area based on the weight of concentration and mass of dispersion imbibed into the electrode. Thus, at the current market price for Pd, the cost of Pd is expected to be less than 0.011 cents/sensor at such a low loading.

The solvent exchange approach of depositing Pd nanoparticles onto the porous electrode has proved to be an effective technique. The Pd nanoparticles as seen in the SEM images have dispersed well due to the presence of sufficient pores in the graphene electrode. Although the dispersion is present, the technique does not guarantee the exact reproducibility than compared to some of the established techniques such as chemical vapour deposition [130]. The advantage of this technique is that it is simple and cost effective.

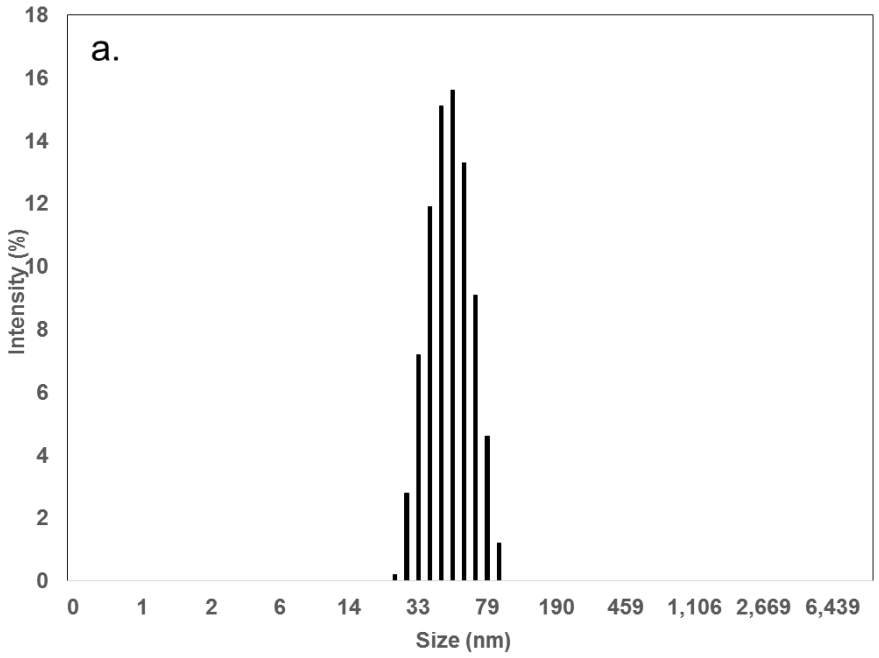

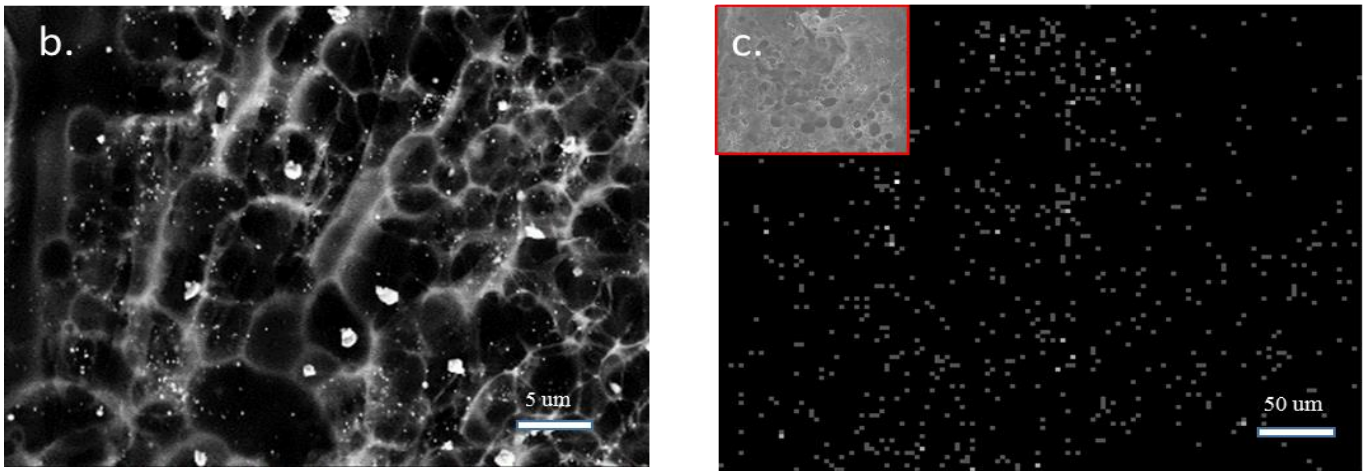

Figure 4- 5: (a) Statistical representation of the size of the nanoparticles which fall in 40-80 nm size range. (b) SEM image showcasing the dispersed Pd nanoparticle on the electrodes. (c) EDX analysis of the nanoparticles on the electrode (inset shows the mapping region).

After depositing the Pd nanoparticles, the next step of the design was to develop an electrolyte system that is sufficiently ionically conducting at room temperature, non-volatile and permeable to methane. In previous work, a PVDF/IL system has been used to create high performance sensors for NO_2 detection by casting solutions of this solid polymer electrolyte (SPE) onto monolithic electrodes.[70] Instead, we attempted to use the electrolyte system by painting it onto our porous electrodes and allowing the PVDF/IL to penetrate and the PVDF to crystallize while confined within the pore space. The preparation of this solid polymer electrolyte is derived from the work done by Kubersky and group [70]. The porous morphology of the solid polymer electrolyte as reported in their work has helped to create a porous network of polymer imbibed electrolyte for our design of interdigitated electrodes. To help better understand the structure and properties of this system SEM images have been taken (as shown in Figure 4-6). Figure 4-6 (a) is an SEM backscatter image comparing electrodes with and without the electrolyte polymer layer from a front view. As visible in the image the SPE layer completely covers the electrode surface forming an uneven porous layer. The two surfaces are easily distinguishable by the non-appearance of electrode lines on the electrode covered with electrolyte layer.

Figure 4-6(b) is a SEM image focusing on the solid polymer electrolyte layer above the electrode. The image clearly shows the porous nature of the polymeric network of ionic liquid

imbibed in PVDF. The pore sizes, measured with the help of the SEM images range from 5 to 40 um. These pores are important as they let the gaseous molecules pass through them and interact with the electrode- electrolyte surface.

Figure 4-6 (c) helps to analyze the porous surface further. One of the pores on the surface is mapped using EDX analysis (as seen in Figure 4-6 c (ii, iii, iv). C, S and F is mapped in this elemental analysis. Carbon is scarcely dispersed everywhere in and around the pore. The carbon represent the laser induced graphene, which is below this layer of SPE. The presence of carbon in the porous region shows that the pores lead to the electrode surface. As expected fluorine can be seen concentrated along the periphery of the pore showcasing that the PVDF is forming the porous network of the solid polymer electrolyte. The presence of S in and around the pore with high concentration in the pores shows the dispersion and proper imbibition of the electrolyte in the polymeric network. The presence of S in the pore shows the ability of the electrolyte to come in contact with the electrode while being held securely by the PVDF substrate.

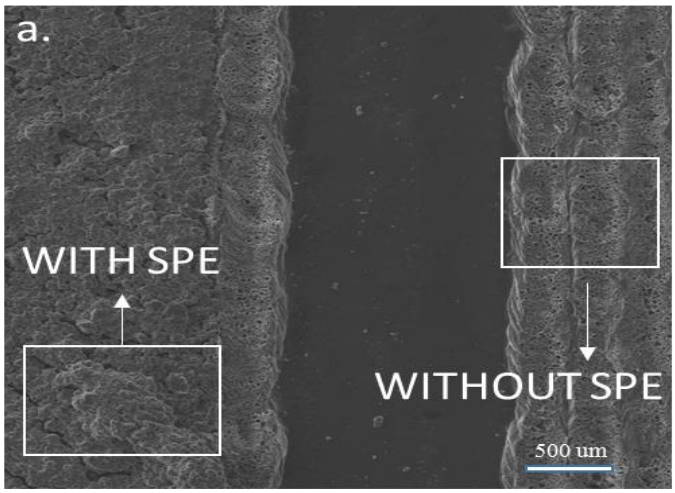

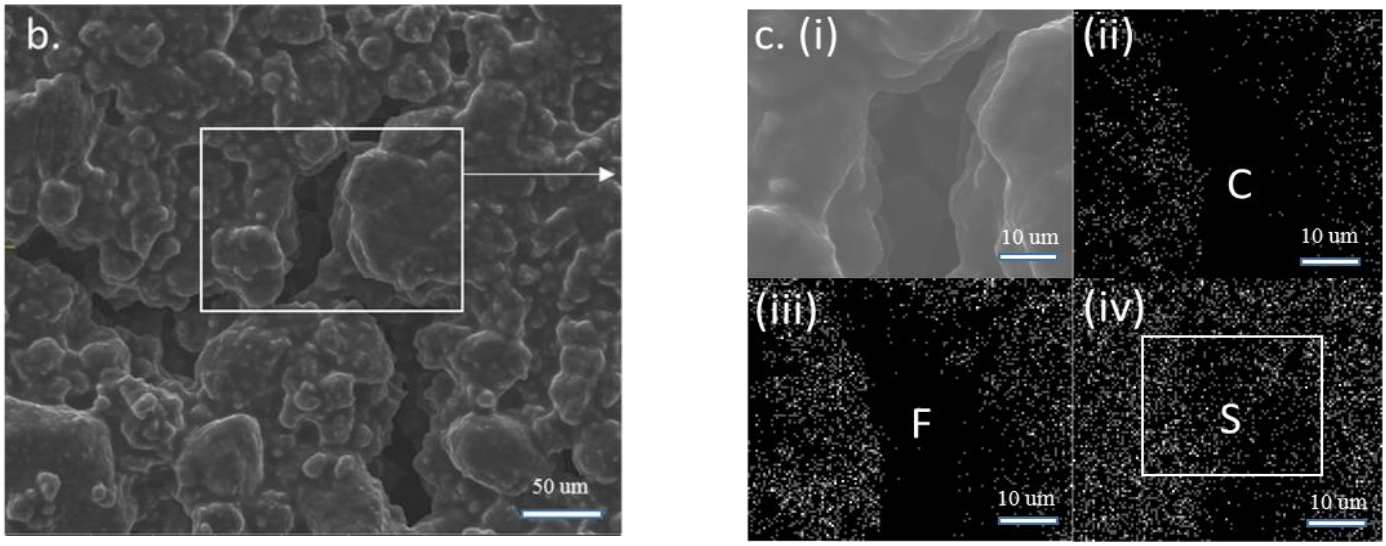

Figure 4- 6: (a). SEM image of electrodes with and without solid polymer electrolyte; (b) SEM image of the solid polymer electrolyte focusing the porous regions; (c)(i) EDX mapping image, (ii) EDX mapping of Carbon in the image, (iii) EDX mapping of Fluorine, (iv) EDX mapping of Sulphur.

The SEM image in Figure 4-7 (a) shows a vertical cross-section of the electrode with solid polymer electrolyte deposition on it. The inset in the image is a sketch of the top view. The top view as seen in the SEM images helps to better characterize the morphology and understand the penetration of the electrolyte. As seen in the image the polymeric layer can be clearly distinguished by the globular PVDF substrate with IL stretches in it. The box labeled a) in the image in Figure 4-7(a) shows this region. The electrode region can be identified with a slightly raised up region (the graphene electrode surface is slightly raised up due to the laser ablation that forms gas which escapes during the electrode formation, creating pores and a raised up surface) with pores in the region as seen in box (b). The region highlighted in box (c) is the carbon tape on which the sample has been rested for taking the SEM image.

The image is Figure 4-7(b) is an attempt to better understand the morphology of the entire system and also the reaction mechanism. The SEM sample in figure 4-7(b.i) is prepared by scrapping off some of the solid polymer electrolyte deposited over the electrode. The scrapping helps to look onto the electrode surface more closely and understand the elemental distribution on it. The EDX mapping suggest the presence of elements like C, N, S, F and Pd. The carbon in image b (ii) is

representative of the laser induced graphene electrode. The high density showcases the mapped region as the electrode surface. The presence of N is due to the polyimide (KaptonTM sheet) on which the electrodes have been formed. The image b (iv) shows the presence of fluorine which corresponds to the PVDF. The image b (v) corresponds to sulphur which is well dispersed in the image showcasing that the electrolyte is in contact with the electrode and has a good dispersion. The scrapping off of some of the polymeric layer helps to map the small Pd nanoparticle as shown in b (vi). The presence of dispersed Pd nanoparticle on the surface along with IL (S mapping) and electrode (C mapping) helps explain the mechanism. The overlapping of these elements suggests presence of numerous active locations (figure 2-1) where the suggested reaction happens when the methane gas comes in contact with the electrolyte on the electrode surface by passing through the porous polymer and the electrode surface.

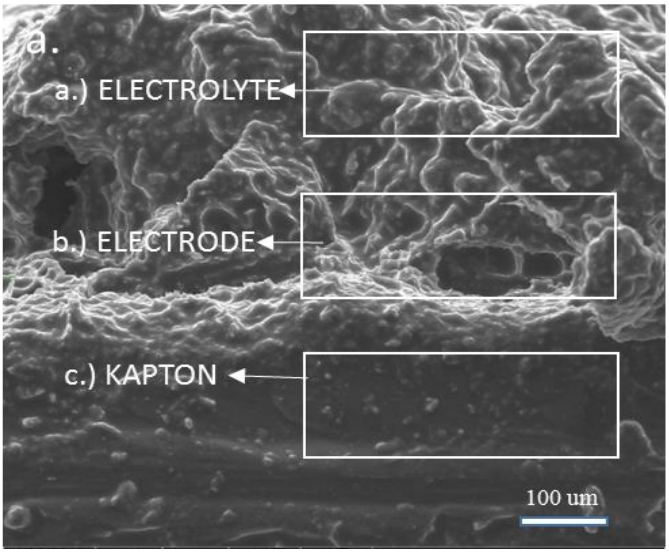

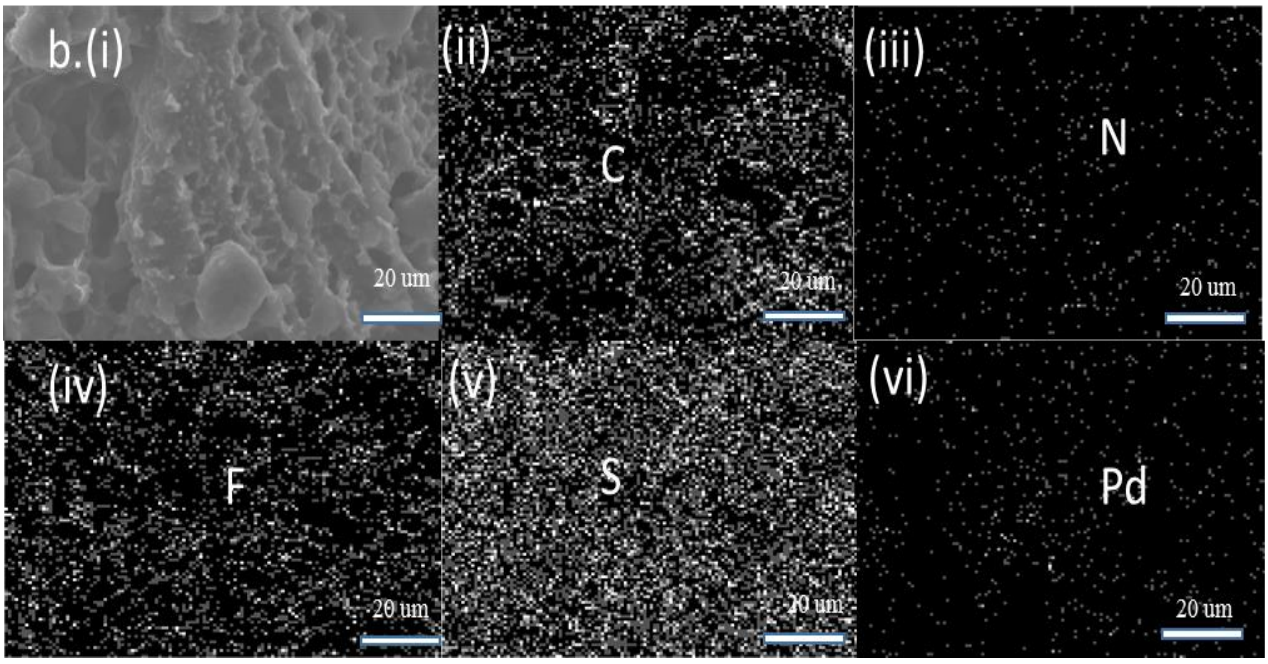

Figure 4- 7: (a) SEM of vertical cross-section of the electrode showcasing the electrode and electrolyte (inset image of a sketch for the same); (b) (i) image of the region of scrapped off SPE on the electrode on which EDX analysis has been performed, EDX mapping of (ii) Carbon, (iii) Nitrogen, (iv) Fluorine, (v) Sulphur and (vi) Palladium.

4.3. Reaction mechanism

In order to investigate the chemistry behind the operation of the sensor, exclusion tests were conducted. The exclusion test is a method to determine in what conditions is the sensor responsive. An array of data is recorded with the help of a potentiostat by holding the sensor at various constant potentials. By conducting various trials as shown in Figure 4-8 (a), a potential of 0.6 V is found to give consistent results with different concentrations of methane. The results show that the sensor is not responsive at voltages below 0.6 V. As the potential is increased further, the stable response period reduces and the current eventually drops to zero. A consistent result can be defined as a stable current value against a constant potential and concentration of methane for a limited time period. A hypothesized oxidation–reduction mechanism is proposed for this reaction. To confirm this hypothesis, the exclusion test is conducted. The sensor response is measured using a potentiostat by holding it at a constant potential of 0.6 V. The current response is measured at a

constant potential of 0.6V in a dry air atmosphere. The resulting current response can be seen in Fig 4-8 (b). The current response shows a continuous reduction (degrading response) in current over time down till reaching near zero level value when holding it at constant potential. This response indicates that the sensor is not responsive in a pure air atmosphere. A similar test is conducted by injecting 75 ppm of methane in air atmosphere. The response in Fig 4-8 (b) indicates that the sensor is responsive to methane. A constant current is observed when methane is injected. A similar experiment with and without methane in a nitrogen atmosphere (free of air (oxygen)) as indicated in Fig 4-8 (b) shows exponential decay in degrading current. This is what is expected for charging of the electrochemical double layer. These exclusion tests helps to determine that air (oxygen) is vital to the process of sensing methane.

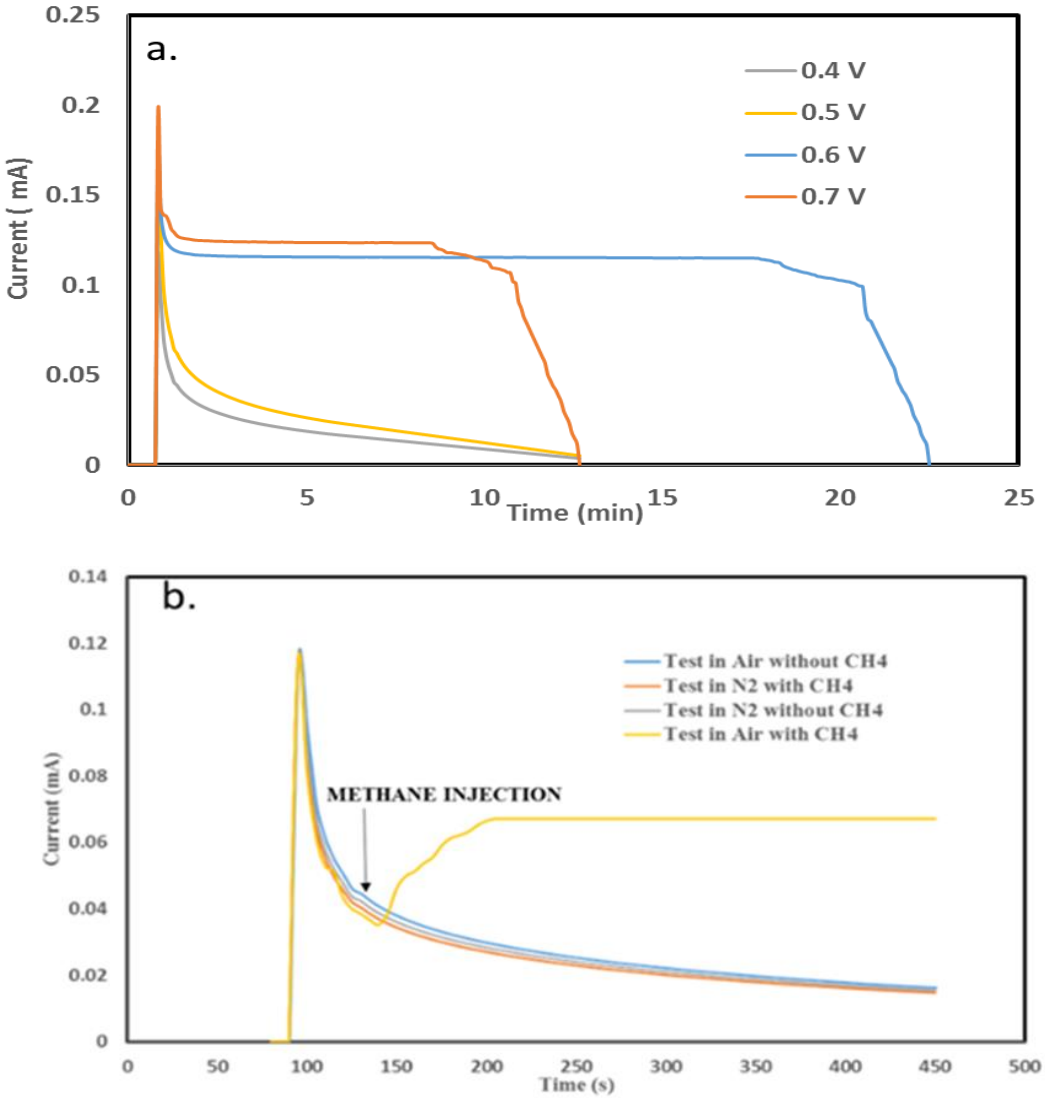

Figure 4- 8: (a) Current response of sensor at constant methane concentration at four different potential. (b) Current measured at a constant potential of 0.6 V at different conditions.

Operating at voltages much higher than 0.6 V or long time operation at 0.6V results in in the pseudo solid-state electrolye changing in colour from white to a more translucent state as illustrated in Figure 4-9 (a). We hypothesized that this could be due to water and accumulation at one of the electrodes. According to Faradays law, basic mass calculation suggests a formation of about 2.8 x 10^{-6} g of water at a current of 0.102 mA and a time duration of 300 s. To understand the reaction products from the electrochemical sensor, off-gas analysis using FTIR was carried out. Figure 4-9 (b) showcases the results obtained when high ppm of methane is injected in the gas chamber at two different concentrations (Figure 4-9 (b)). The results suggest the formation of minute levels of water and carbon dioxide. The two products are observed only for a few seconds due to the quick saturation of the sensor at high ppm of methane. Nevertheless, the results helps to confirm the products of the reaction and corroborate to the study performed by Zhdanov, V.P. *et al* [131], who suggested that methane oxidation occurs in two step kinetics with a low reactive state with the surface covered by platinum or palladium oxide and a high-reactive state with the surface covered by the chemisorbed oxygen. Thus, it can be rationalized that Pd-O is the predominantly active site where methane oxidation takes place on this Pd oxide layer. The ILs can provide a strong polar environment, wherein the C–H bond in methane can be activated electrostatically. Once H dissociated from CH_4, further polarization of CH_4 makes it even easier to dissociate additional C–H bonds. Based on above rationalization, the following methane oxidation mechanism in NTf_2 based ILs has been proposed. In step 1, oxygen is supplied from the gas phase via irreversible dissociative adsorption on Pd vacant sites.

$$2Pd + O_2 \leftrightarrow 2PdO\ (ads) \quad (1)$$

In NTf_2 based ionic liquid system NTf_2 could adsorb on the metallic oxide surface. NTf_2 typically behaves as a weak or non-coordinating anion. However a weak Pd-NTf_2 coordinate complex likely can occur in the absence of other ligands. The formation of Pd-NTf_2 would have high catalytic activity

$$Pd - O + \mathrm{NTf2} \rightarrow O - Pd - NTf2 + e \quad (2)$$

The reaction is limited by dissociative chemisorption of CH_4 occurring via Eley-Rideal mechanism[132] by breaking of C-H bonds.

$$4O - Pd - NTf_2 + CH_4 \leftrightarrow CO_2 + 2H_2O + 4Pd - NTf_2\ , \quad (3)$$

where H_2O generated could adsorb on the electrode surface since IL is hydrophobic.

The overall reaction can hence be summarized as

$$CH_4 + O_2 \xrightarrow{Pd/NTf_2-IL} CO_2 + 2H_2O \quad (4)$$

The proposed overall reaction helps to understand the chemistry behind this electrochemical sensor and helps understand the working of this system.

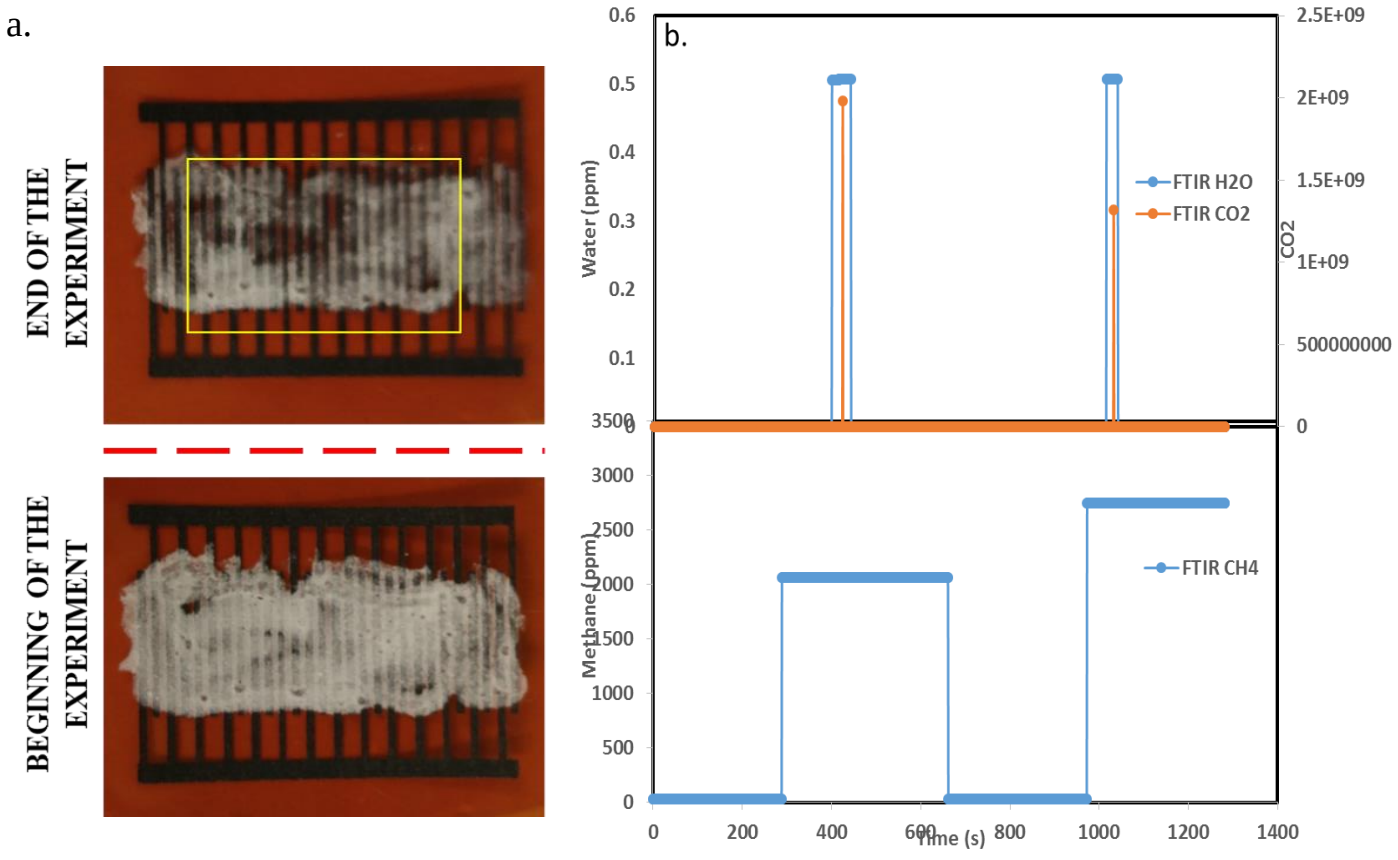

Figure 4- 9: (a.) Image of the sensor before and after testing it with methane at a constant potential and constant methane concentration; (b) FTIR results showcasing the water and carbon dioxide forming at two different intervals corresponding to two different methane concentrations.

4.4. Maximum Response Studies

4.4.1. Effect of Pd loading on the sensitivity of the methane sensor

The Pd nanoparticles play a vital role in detection of methane gas. The Pd helps to offset any activation overpotential that develops. Our hypothesis is that a higher Pd loading would lead to a more responsive sensor. An experiment to relate Pd loading to the sensitivity of the sensor was performed. Three samples of different Pd concentrations were deposited on the sensor. The sensor was then tested for sensitivity by subjecting it to a variety of different concentrations of methane. The results however agreed to the hypothesis partially. The increase in concentration from 0 mM to 25mM reciprocated in increase in sensitivity but a further increase in concentration to 30 mM and 35 mM saw no such increase. The similar response seen after a concentration of about 25 mM suggests that there might not be any significant performance improvement after a certain level of deposition. The optimization results are depicted in Figure 4-10 (a). The plateau in performance of the sensor with increase in Pd concentration can be attributed to the fact that the adsorption of the Pd nanoparticles is limited to the porous structure of the laser induced graphene electrodes. The Pd nanoparticles have occupied most of the active sites (pores) and hence increasing any further concentration does not result in any further increase in the performance.

4.4.2. Effect of the amount of IL imbibed in the polymer on the sensitivity of the sensor.

The amount of IL used in the sensor also plays a major factor in the sensitivity of the sensor. The IL facilitates the speed of the reaction. The higher the amount of IL on a given area, the higher formation of O-Pd-Ntf2 sites on the electrode for methane to bond and carry the reaction. Hence, more ionic liquid should correspond to higher sensitivity for methane gas. As shown in figure 4-10 (b), the ratio of IL to PVDF is varied to determine its effect on the sensitivity. The results show that 1: 1.5: 3 gives the best sensitivity, shown in Figure 4-10 (b). Ideally 1:2:3 should have had the best results but it is noted that using 2 parts ionic liquid does not gel with the polymer leading to a liquid electrolyte film that makes device handling difficult.

4.4.3. Effect of solid polymer electrolyte on the sensitivity of the sensor

A similar test is done by varying the amount of NMP in the solid polymer electrolyte formation ratio. The experiment is done while holding the PVDF: IL ratio constant and varying their dilution in NMP. The variation in NMP experiment helps confirm our optimization results. A trend with highest current value recorded at 1: 1.5: 3 ratio. The NMP is ratio is varied from no NMP in the beginning to no PVDF (only NMP) towards the end. Figure 4-10 (c) shows the maximum response results. The results can be justified by the fact that the purpose of NMP is to help facilitate the binding of the PVDF and ionic liquid. A mixture of PVDF and IL does not gel together, causing significant phase separation and low homogeneity. The NMP solvent vaporizes after dissolving PVDF and heating the solution. The vaporization creates additional pores in the solid polymer electrolyte causing it to form a porous layer. This porous layer is the reason why methane can pass through the polymer layer and interact with the electrolyte at the electrode interface for facilitating any chemical activity. An experiment was performed to test the importance of PVDF in sensitivity response of the sensor. To realize the role of PVDF, the sensor was coated with 100 μm thick layer of IL and another one with solid polymer electrolyte (PVDF + IL). The sensor when tested with 50 ppm of methane, resulted in 38.3% higher response with solid polymer electrolyte than compared to the one without any PVDF. This can be attributed to the fact that a pure ionic liquid layer creates hurdles for methane to come in contact with the electrode whereas the use of PVDF with IL enables the gas to permeate all the way through to the electrodes.

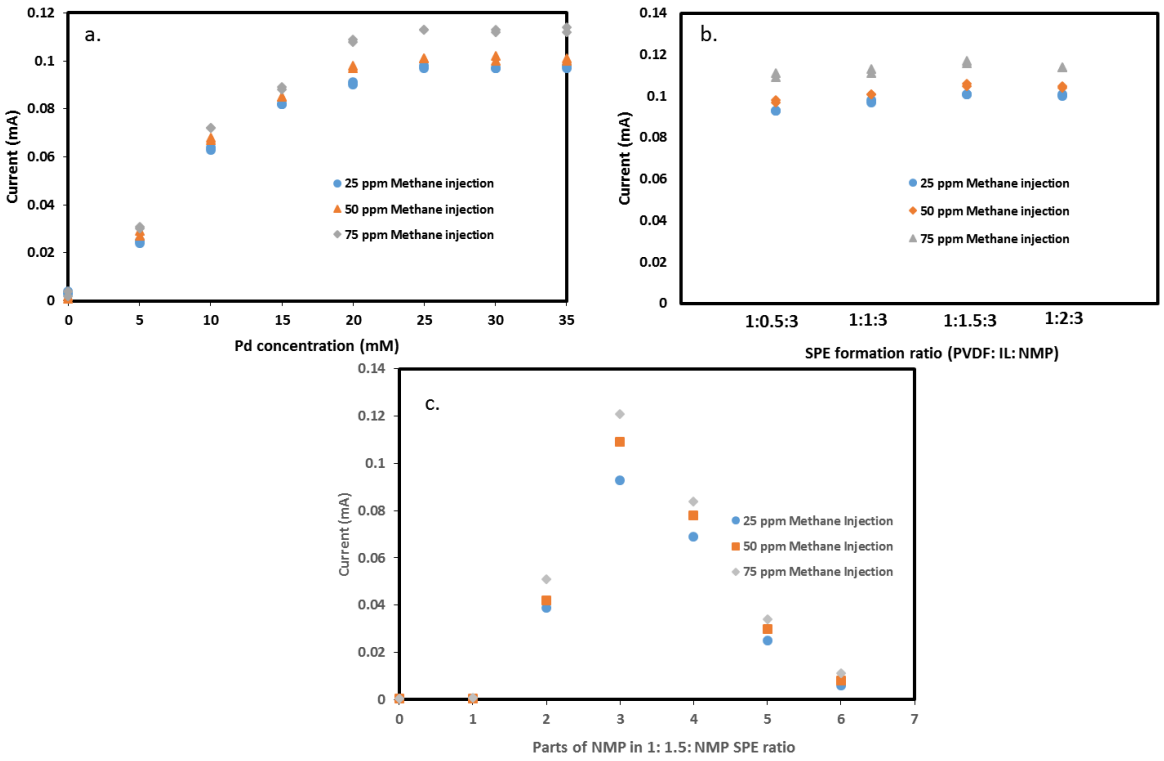

Figure 4- 10: (a) Current response of sensors at constant potential with different Pd loading at three different methane concentrations; (b) Current response of sensors at constant potential with different Ionic liquid amount at three different methane concentrations; (c) Current response of sensors at constant potential with different solvent (NMP) amount at three different methane concentrations.

4.5. CH_4 sensing properties

Figure 4-11 shows the response of the sensor towards CH_4 under a range of different concentrations. A constant voltage of 0.6 V is applied to three different concentrations (5 ppm, 25 ppm and 50 ppm) of methane. On application of constant potential the current variations are recorded for the time duration until which the current levels drop down to background levels of 0.0005 mA (noise). Figure 4-11 (a) shows the current response for 5 ppm of methane injection. A spike in current is seen just after the initial equilibrium which can be attributed to the double layer charge capacitance in the sensor. The spike diminishes and the current reaches stability for a limited duration. A gradual reduction of current is witnessed which can be explained due to the saturation of active pores with off products like water. This saturation blocks the pores, hence

cutting off any further reaction at the active site. The saturation impacts the ability of the sensor to sense methane for a continuous duration. A rest period where drying of sensor can take place needs to be provided for effective operation of the sensor. Figure 4-11 (a), (b) and (c) shows the operation of the sensor with increasing drying time. With 5 ppm of methane, the stable current is observed for about 16 min after which the current starts to decay. Once the current reaches noise levels, the sensor is allowed to rest in dry air conditions for about 12 min after which the 99.31% of the previous stable current values are seen. The same test is repeated for 25 ppm and 50 ppm. Similar trend is observed with a distinct observation that the drying time required for higher concentrations increases to 17 and 20 min respectively to reach approximately 99% of the original stable current values. The increase in drying time can be attributed to higher rate of reaction with increasing concentration of methane leading to increase in product formation. The stability duration also reduces with increasing concentrations which is in sync with the previous observations.

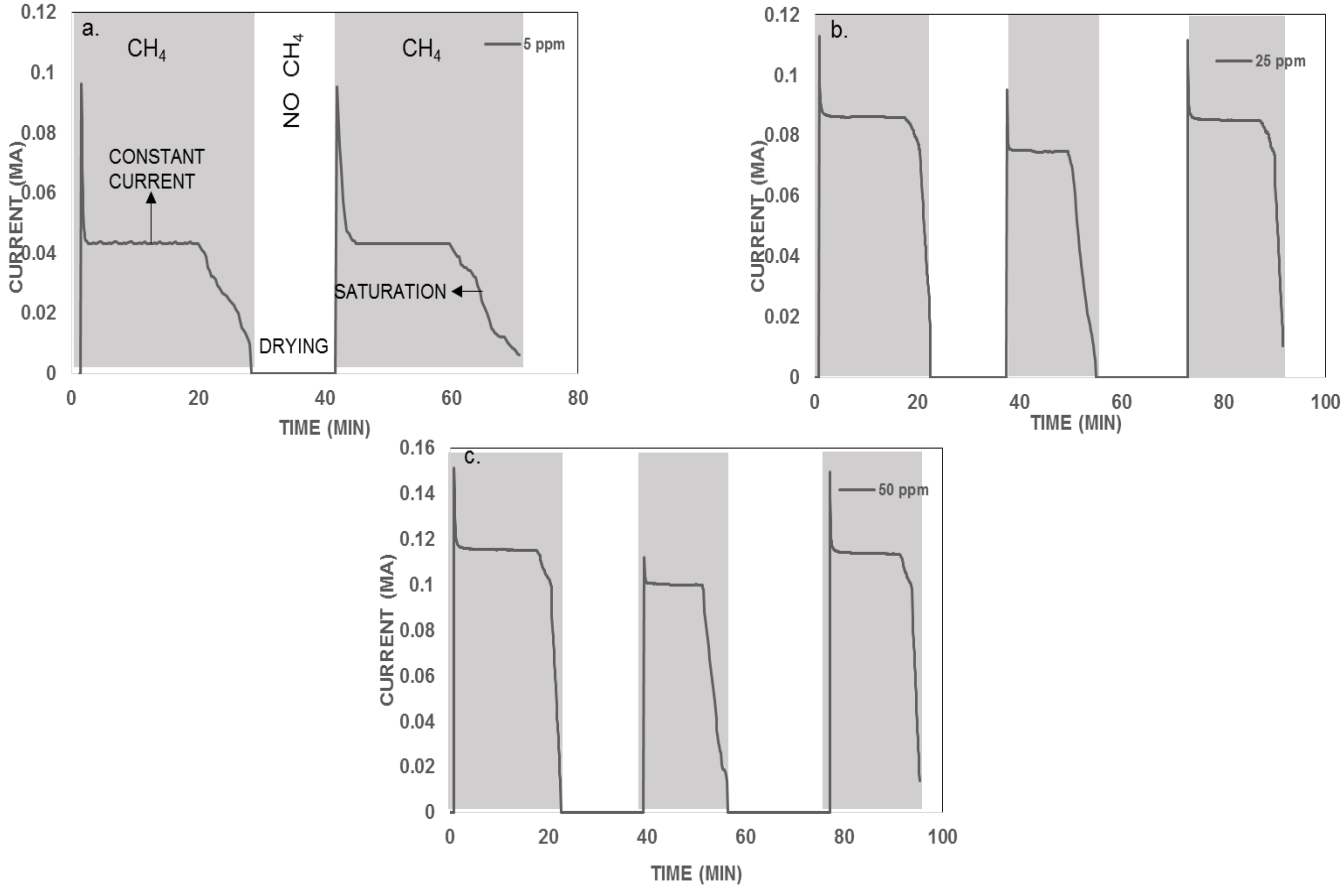

Figure 4- 11 (a, b, c) shows the sensor response at different concentration with varying drying time once saturation is achieved.

Based on the information obtained from the drying time experiment of 50 ppm methane concentration, a time duration of stable current of about 16 – 18 minutes is obtained wherein the sensor response does not degrade and the saturation of sensor does not play its role yet. This time duration is utilized for conducting another experiment to determine the response time of the sensor with changing concentrations of methane. Methane is injected for a fixed duration of time in steps of 10 ppm. As shown in Figure 4-12 (a), the methane concentration is increased in steps of 10 ppm every 2 min. It is observed that with a step increase in methane concentration, there is also a corresponding increase in the current values. On conducting electrochemical impedance spectroscopy on the sensor and fitting the results to a model curve, the resistance and capacitance values are obtained. By fitting an exponential current decay curve to the current time curve, RC time constant of 41.12 seconds was obtained. By fitting another decay curve onto a current vs. time graph obtained from the sensor when subjected to no methane resulted in a RC time constant of 11.3 seconds. The difference in the two RC time can be attributed to the fact that with the presence of methane, electrochemical behaviour of the sensor changes due to additional reactions and transfers taking place resulting in a delayed response. This time constant signifies the time it takes for current to decay 63.2% value of the initial double layer current. At this point stable current is achieved. The response time of the sensor can hence be calculated as 41 s $\pm$ 1 s. The root mean square (RMS) value of the current obtained from different concentrations of methane is 0.0878 mA, which can hence be known as the signal current. The average noise value obtained is 0.005 mA. Hence the signal to noise ratio for this sensor is 17.5. The signal to noise ratio obtained is promising for an electrochemical sensor in compared to others reported in the literature [133][134]. It is however significantly lower than optical and NDIR based sensors[29], [135].

Figure 4-12 (b) shows the results of current response with varying methane concentration for four different sensors. The four sensors in the image (inset) are all identical except the number of finger electrodes (electrode lines). The graphical response of the sensors with 18, 9, 6 and 3 electrode lines is shown in the figure. On analyzing the response at 5 different methane concentration for these four sensors, it is observed that the current response decreases proportionally with the reduction in electrode lines. There is an average 32% reduction in current

response from 18 electrode lines to 9 electrode lines. A further 23 % reduction is seen from 9 lines to 6 lines. An average 31% reduction in current response is observed when lines reduce from 6 to 3. The results are indicative of the fact the lower the number of lines, the less surface area for the reaction, hence less current observed. The reduced lines makes the sensor a better fit in terms of lower costs that arise from reduction in energy consumption and material use. The sensors are also tested for response in air and a current value of 0.008 mA is obtained which is slightly higher than the noise level. This current could correspond to the theoretical concentration of methane in air (~ 2 ppm), but there is no definite theory or proof to correlate this value to the atmospheric concentration of methane.

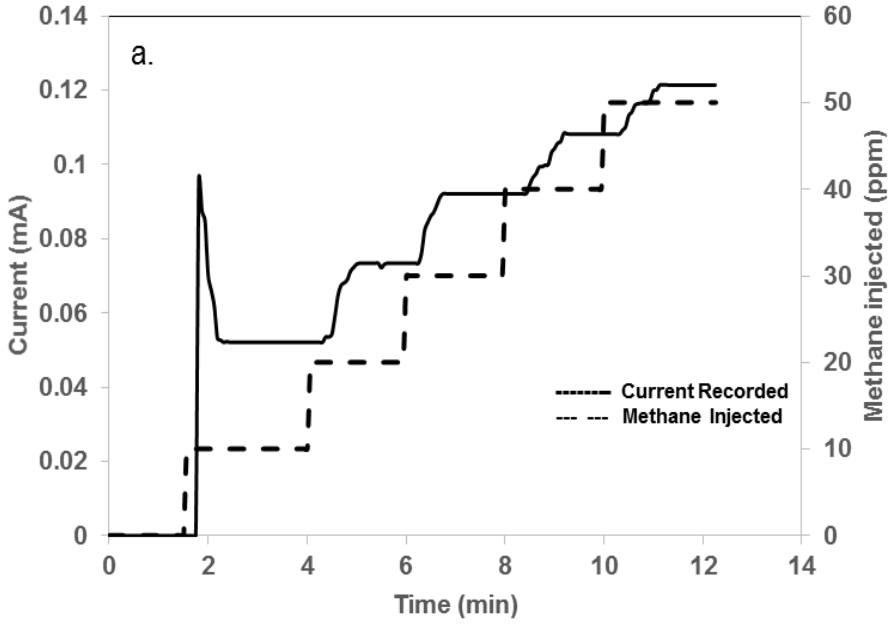

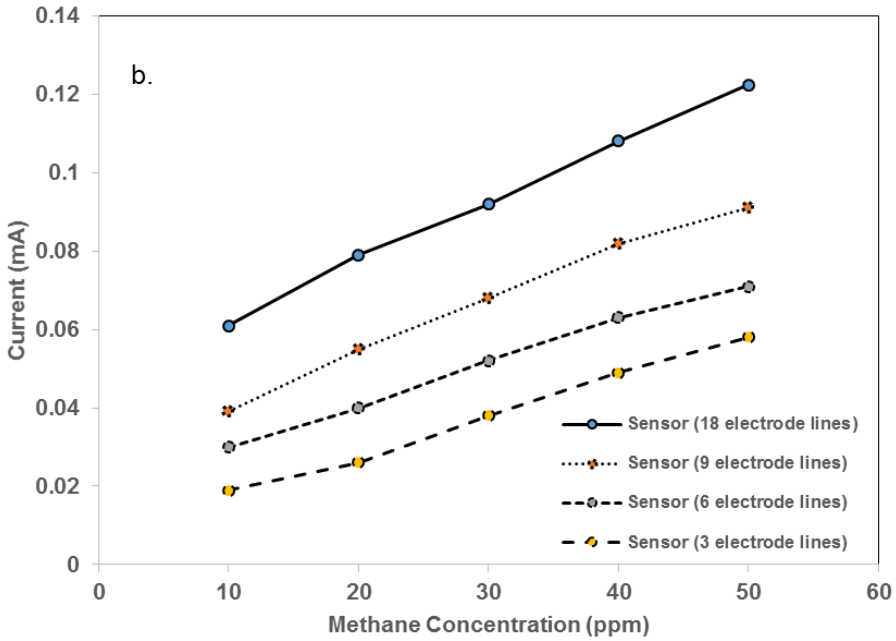

Figure 4- 12: (a) current response with a step variation in methane concentration; (b) response of sensor with varying number of electrode lines.

4.6. Interference gases and Lifetime Analysis

From the previous results it has been established that the sensor is responsive to methane and also responsive to different concentrations of methane. In order to verify the performance of the sensor in real atmosphere, the sensor has been tested for performance in presence of interfering gases that will be present in a natural gas system, where the sensor will be best put to use. The interfering gases that are selected for this experiment are water vapor, ethane and propane. Natural gas has trace quantities of ethane and propane[1], hence it is important to know whether the sensor is responsive to these hydrocarbons apart from methane. The sensor is tested with minute quantities of ethane and propane and the resulting current has been plotted as shown in figure 4-13. The results suggest that the sensor does respond to these longer chain hydrocarbon gases but the response time and the current recorded is lower than compared to methane. Also the response towards propane is lower than that towards ethane. One explanation for this behavior could be the increase in size of the molecular structure that needs to pass through the pores and react. Moreover the oxidation- reduction reaction would face difficulty with increase in molecular structure and

limited presence of oxygen. The sensor is also tested with methane but in humid conditions (RH 100%). The sensitivity of the sensor towards methane is tested in presence of 100 % humidified air and the response is plotted as shown in figure 4-13. The results suggest a significant reduction in response in the presence of humidified air which can be attributed to both the blocking of pores by water molecules, hindering reaction and shifting of reaction equilibrium backwards due to the presence of excess product (Le Chatelier's Principle). These results obtained suggest that the electrochemical sensor will behave differently in presence of different interfering substances and a standard calibration is required according to the local conditions of the area where the sensor is deployed to gauge the response and interpret the amount of leakage when detected.

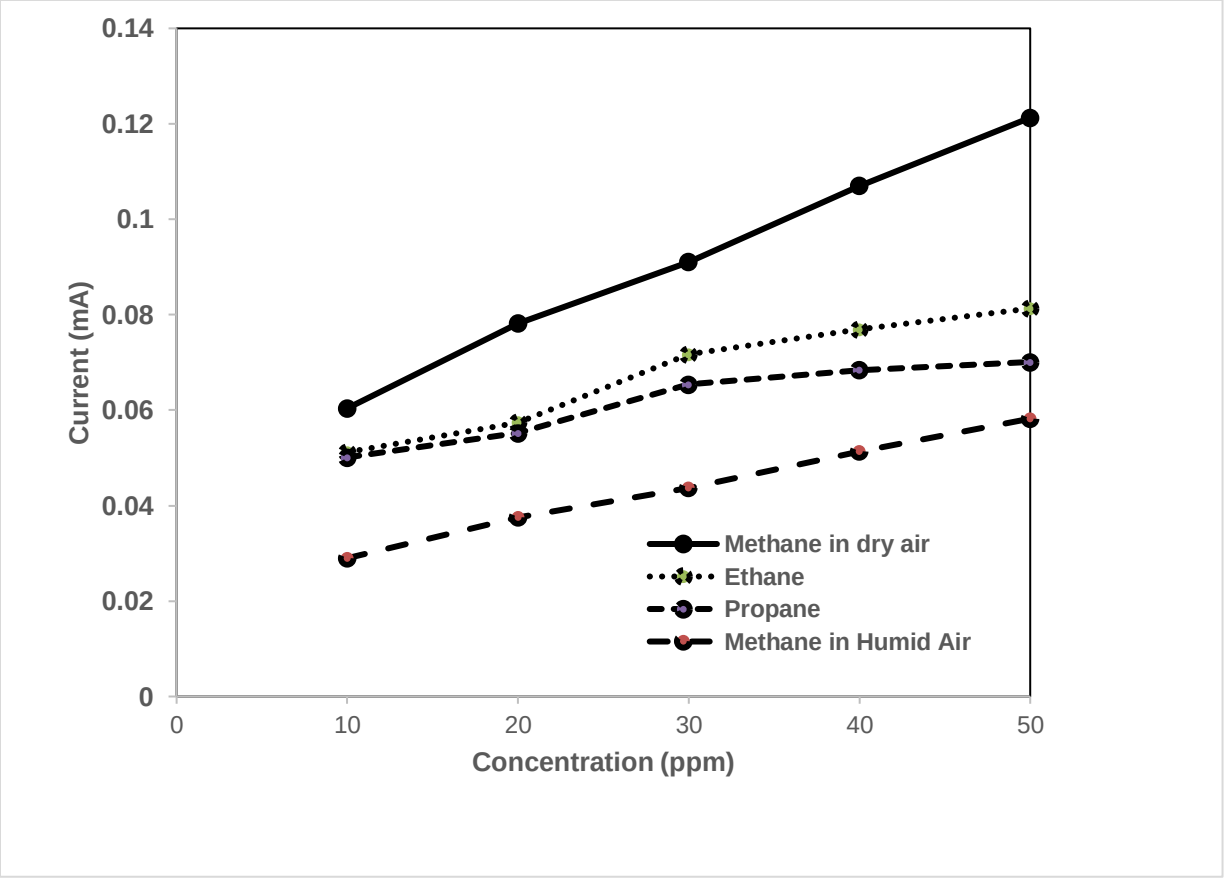

Figure 4- 13: Sensor response with interfering gases

In order to analyse the longevity of the sensor, two set of sensors have been tested daily over a period of 30 days to record the performance of the sensor over a long period of time. The results

shown in figure 4-14 suggests a fairly stable response of the sensor with higher and lower values of 0.092 mA and 0.0868 mA and a standard deviation of 0.0017. The results obtained are promising for using the sensor for longer periods provided a standard calibration is done in order to identify correct amount of leakages while detecting any fugitive release.

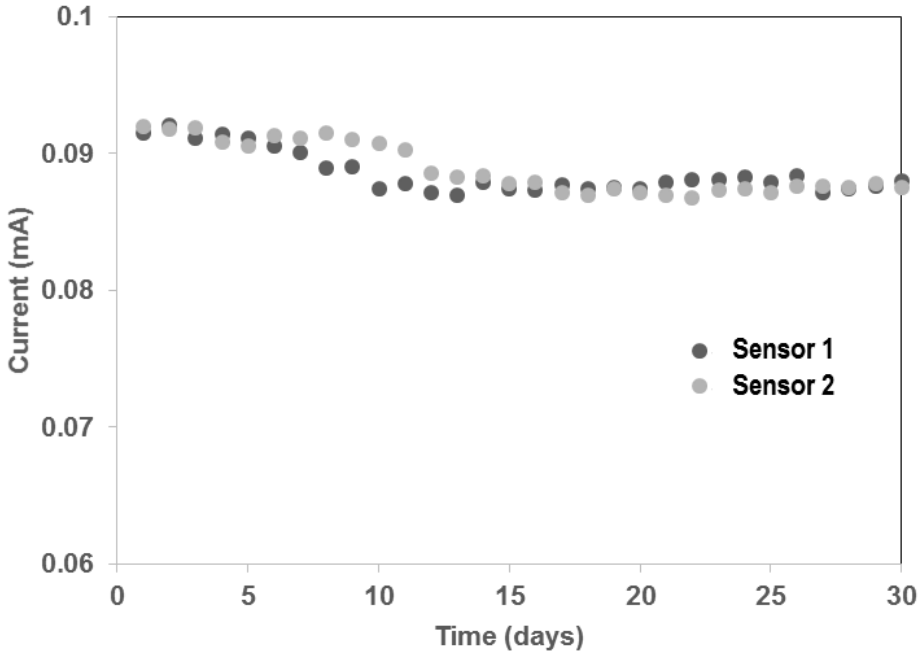

Figure 4- 14: Sensor tested for response for a continued period of 30 days.

4.7. Electrochemical Impedance Spectroscopy Studies.

An experiment was designed to gauge the sensitivity of the sensor to electrochemical environment.

The concentrations of methane gas injected for this experiment were 20 ppm, 30 ppm, 40 ppm and 50 ppm. The data was further analyzed and the Nyquist plots were plotted as shown below.

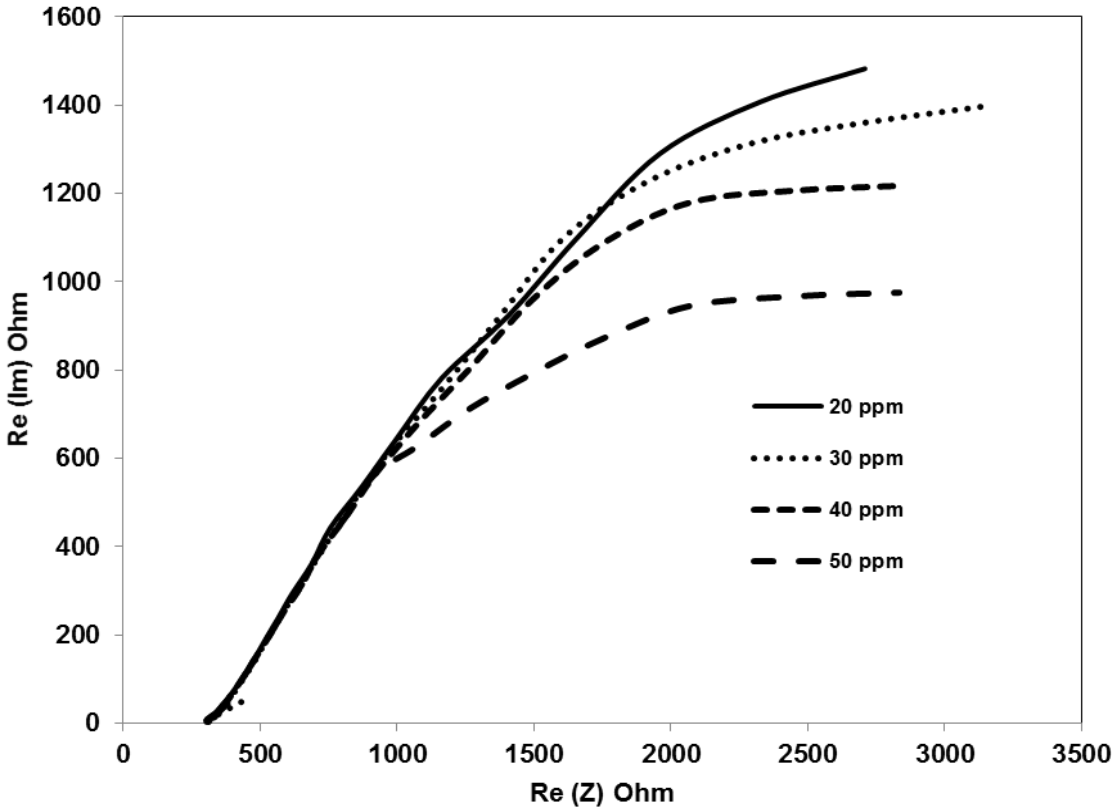

Figure 4- 15: EIS response of sensor at different concentrations of methane.

The Nyquist plots showed that the diameter of the semicircle varied with amount of methane injected, which indicates that the electrodes were sensitive to the electrochemical concentration. In the above case the diameter decreases with increasing concentration because as the concentration increased there was more diffusion, more electrochemical activity hence leading to the increase in number of ions traveling from the anode to the cathode and the current flow therefore decrease in resistance. The resistance data obtained from this analysis is plotted as a function of concentration in figure 4-15 (b). As expected, the resistance shows a decreasing trend with increase in concentration.

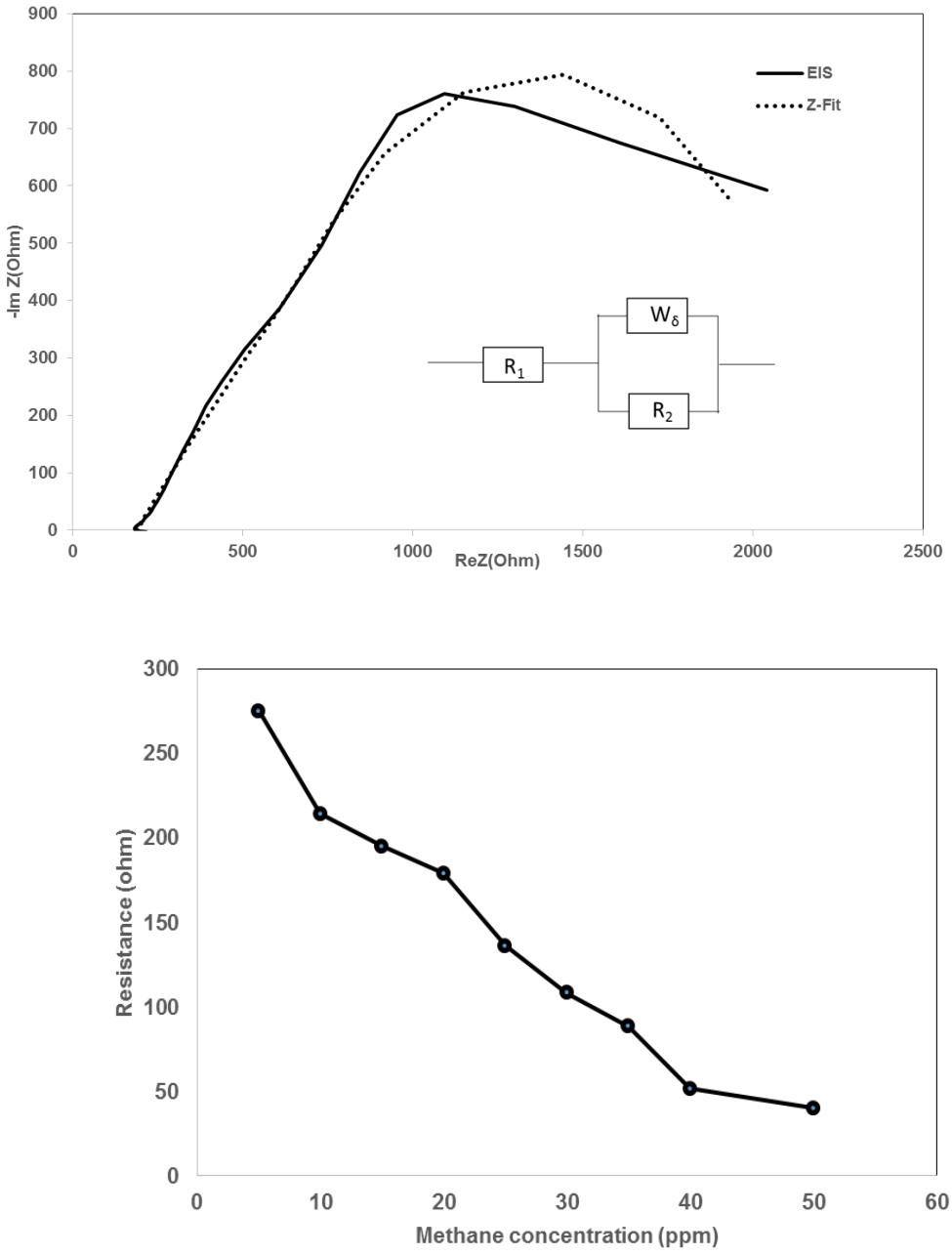

Figure 4- 16: (a) Z-fit analysis being performed to determine the equivalent circuit and corresponding resistance; (b) Resistance across sensor at different concentrations of methane.

Chapter 5: COMSOL Fugitive Release Model

This work was performed with my guidance and the supervision of Dr. Michael Fowler by the fourth year undergrad design project group**.**

The purpose of the COMSOL Fugitive Release Model was to predict the leakage path of CH_4 as it exits the crack and based on the results, determine the optimal positioning of the CH_4 sensor.

5.1. Theory behind COMSOL simulation

5.1.1. Stress Analysis

Linear Elastic Material

Materials that are considered to display linear elastic behavior follow three main assumptions.[140] The assumptions are that the material only undergoes small amounts of strain, the stress is linearly related to the strain of the material and once the load has been removed, the material will return to its original shape. The linear relationship between the stress and the strain of the material can be described by Hooke's Law.

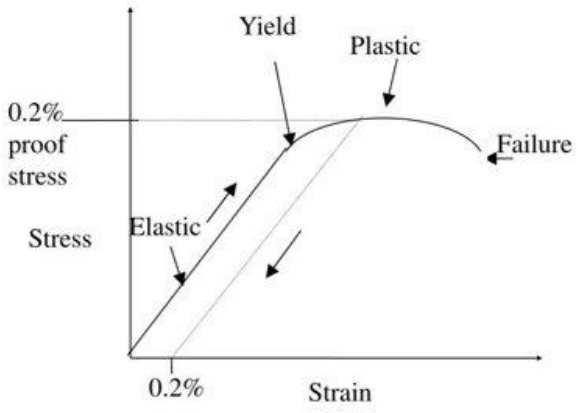

Figure 5- 1: Stress-strain curve of steel

The general shape of a stress strain curve for a linear elastic material can be seen in Figure 5-1.

Pre-tensioned Bolts

During the installation of flanges, bolts are mounted by applying a specified torque to tighten it. This applied torque tightens the bolt to a certain pre-stress value which also causes deformations to any surrounding areas.[141] The pre-tension stress applied to the flange bolts can be determined through the following equation[142],

$$F = cA_tS_p \tag{1}$$

where F is the preload tension force, A_t is the tensile shear area of the bolt, and S_p is the proof load of the bolt.

5.1.2. Computational Fluid Dynamics

Navier Stokes Equations

The flow of a single-phase fluid can be described by the Navier-Stokes equations.[143] It is derived by applying the basic principles of mass, energy and momentum through a finite control volume. The general form of Navier-Stokes consists of three equations:

$$0 = \frac{\partial \rho}{\partial t} + \nabla \cdot (\rho u) \tag{2}$$

the continuity equation that describes the conservation of mass,

$$\rho \frac{\partial u}{\partial t} + \rho(u \cdot \nabla)u = \nabla \cdot [-pI + \tau] + F \tag{3}$$

the conservation of momentum equation, and

$$\rho C_P \left(\frac{\partial T}{\partial t} + (u \cdot \nabla)T\right) = -(\nabla \cdot q) + \tau : S - \frac{T}{\rho}\frac{\partial \rho}{\partial T}\left|\left(\frac{\partial \rho}{\partial t} + (u \cdot \nabla)p\right) + Q\right. \tag{4}$$

the conservation of energy equation.

There are two main assumptions used in the derivation of the Navier-Stokes equations. The first being that the fluid of interest is a continuum, which means that it is considered to be a continuous substance rather than the formation of many discrete particles. The second assumption is that the temperature, pressure, velocity, and density fields are weakly differentiable.

Hagen Equation

The Hagen equation can be used to characterize the leakage of a fluid through a pinhole.[144] It is derived from the momentum equation based on two main assumptions. One assumption is that the fluid flowing through the circular pipe follows the Newton's law of viscosity which means that the shear stress of adjacent fluid layers is proportional to the velocity gradient between the two layers. For a constant temperature and pressure, the ratio is assumed to be constant. The other assumption is that the relative motion between the fluid particles and the solid boundaries is zero. This is referred to as the no slip condition at the boundary.

The fully derived form of the Hagen equation can be seen below:

$$Q = \frac{\pi * D * \Delta P}{128 * L * \mu} \tag{5}$$

The equation provides the volumetric flow of a fluid through a cylinder and is dependent on the pressure difference across the cylinder, the diameter of the leak, the dynamic viscosity of the fluid, and the length of the leakage passageway.

5.1.3. Transport of Diluted Species into Porous Media

The transport of a diluted species into a porous media can be used to model the transport of a chemical species by means of diffusion, convection and dispersion.[145] The general mass balance equation for the transport of a chemical species is as follows,

$$\frac{\partial c}{\partial t} + \nabla \cdot (cu) = \nabla \cdot (D \nabla c) + R \tag{6}$$

where C is the concentration of the species, D is the diffusion coefficient, R is reaction rate of the species, and u is the velocity vector.

If the transport is determined only by diffusion/dispersion, it is governed by Fick's law and reduces to the following form,

$$\frac{\partial c}{\partial t} = \nabla \cdot (D \nabla c) \tag{7}$$

5.2. COMSOL Model

Currently, the COMSOL modelling is composed of three different simulation areas; a stress analysis of the flange, the fluid flow of the pipe/flange system and the dispersion of the CH_4 as it exits the crack. For the simulation, a normal mesh size was used to obtain a balance between accurate results and a reasonable computation time.

5.2.1. Stress Analysis

There is a lack of literature support on methods regarding the prediction of crack development location on pipelines. For this reason, it was determined that a stress analysis can be used to find the potential high stress areas along the flange. These high stress areas would indicate high probability locations for crack development. Based on the information provided from Pro-Flange and the conducted research, it was found that many flange leaks are due to operator error. The solid mechanics model shows the stress development in the flange due to various human errors such as uneven pre-stressed bolts and displacement of the gasket. In industry, uneven pre-stressed bolts would occur if an operator applies an uneven torque on the bolts resulting in areas of higher and lower stress.

In COMSOL, an uneven pre-tensioned stress analysis was done to simulate an uneven tightening of the bolts during installation or maintenance. This was done by setting the pre-load stress of one of the bolts to be higher than that of the other three. Also, a displacement condition was placed on the upper edge of the gasket to simulate misalignment during installation or any shifting that may occur after repeated use of the pipeline.

As seen in Figure B-3 of Appendix B, the bolt with the higher pre-stressed force is under the largest amount of stress, which would make a crack more likely to develop in that area. Figure B-4 of Appendix B shows the resulting von Mises stress caused from the gasket displacement. For both the pre-stressed bolt and gasket displacement conditions, the rest of the pipe/flange were set to be fixed constraints.

5.2.2. Computational Fluid Dynamics

The fluid flow through the pipe and flange was simulated using computational fluid dynamics. Single-phase laminar flow was used to simulate the fluid flow within the pipe/flange system and the fluid dynamics are governed by the Navier-Stokes equations. Laminar flow was chosen to simplify the model and reduce the overall computation time. To further simplify the physics of the fluid flow, it was also decided to set the wall with no slip conditions. The resulting streamlines and principle volume flow direction can be seen in Figure B-5 of Appendix B.

To simulate the leak in COMSOL, a long cylinder with a very small radius was inserted into the pipe/flange system to allow for fluid to flow from inside the pipe to the outer flange wall. In reality, a crack would not have such a well-defined shape but for the purposes of modelling, it provides a good estimate. Simulations were run for 0.15mm, 0.25mm, and 0.5mm crack size leaks for a range of internal pipe pressures, which can be found in Table B-2 of Appendix B. The fluid flow through the crack can be seen in Figure B-6 of Appendix B.

The leakage rate for the 0.33mm crack determined by the Hagen Equation was found to be about 2722 m^3/year. This leakage rate is very close to a value recorded from an EPA study on a Russian compressor station of 3077 m^3/year.[146] The EPA study does not specify the actual size of the leak, but the values still show that the COMSOL model is able to produce realistic leakage rates.

5.2.3. Transport of Diluted Species into Porous Media

To simulate the dispersion characteristics of the CH_4 gas as it exits the crack and enters the atmosphere, the system was considered to follow the transport physics of a dilute species in a porous media.[147] The dilute species was the CH_4 gas and the porous media was taken to be air. The porous media was modelled in COMSOL by placing the flange in a rectangular box with a width, depth and height of 0.4m, 0.25m and 0.2m respectively. To determine the rate at which the CH_4 escapes, the Hagen-Poiseuille equation was used to characterize the fluid feeding through cylindrical channels. Simulations were run to see differences in leakage path depending on whether the leak is located at the top or the bottom of flange. The resulting dispersion streamlines for the bottom leak can be seen below in Figure 5-2. The streamline for the top leak can be found on Figure B-7 of Appendix B.

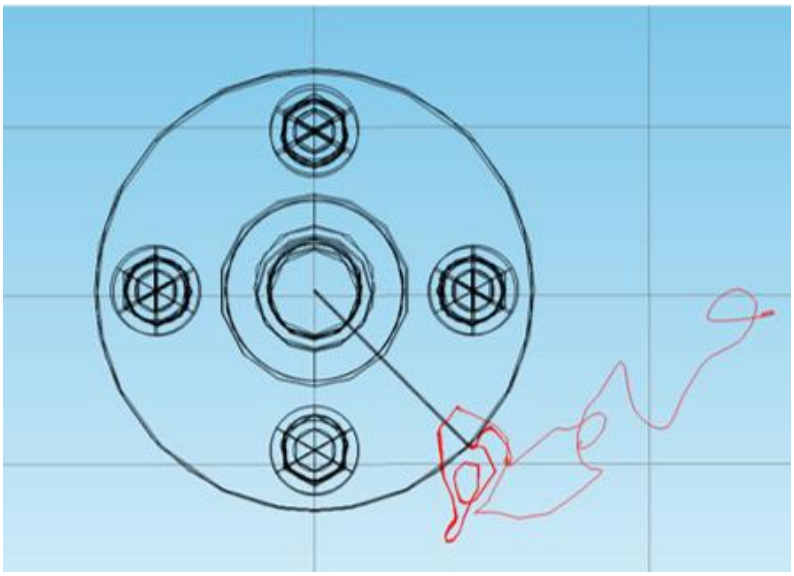

Figure 5- 2: Dispersion path of CH_4 from bottom leak

In both cases, the path of the CH_4 leak was shown to flow away from the flange as it rose. From these results, it was determined that simply placing sensors along the flange surface would be insufficient for CH_4 detection. Additionally, factors that influence the gas flow including weather conditions (wind speed and direction) and pressure (affecting the speed of gas leak) can add to this outward dispersion and cause the gas leak to bypass the sensor. As a result, a donut shaped fender was chosen to encompass the entire flange as seen in Figure B-9 of Appendix B. The final dimensions of the donut shaped fender are: 1.33:1 fender to flange diameter ratio and 1.25:1 fender to flange width ratio. The COMSOL model was re-run with the inclusion of a fender and showed that as CH_4 exits the crack, it moves upwards as it runs along the fender. Figure 5-3 below and Figure B-8 of Appendix B, show how the fender alters the leakage path of the CH_4. This allows for a single sensor to be placed at the top of the fender for CH_4 detection regardless of the position of the leak on the flange.

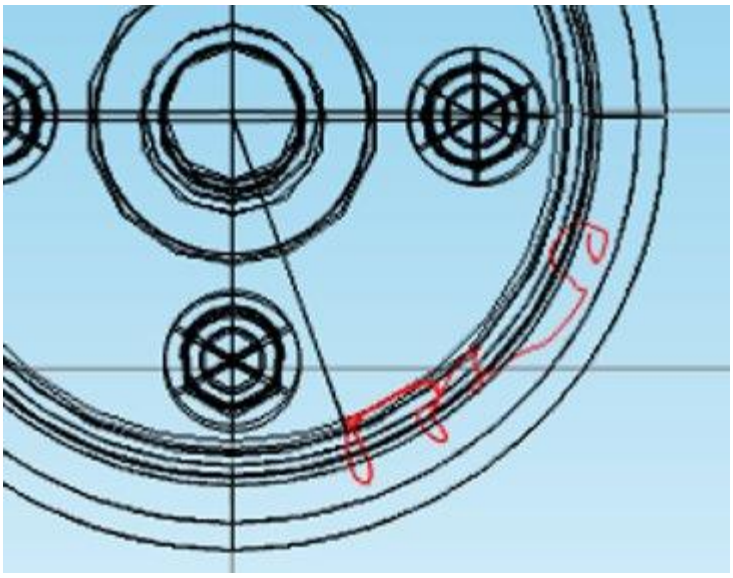

Figure 5- 3: Dispersion path of CH_4 from bottom leak with fender

5.2.4. Assumptions

Summary of assumptions used in COMSOL model:

- The bolt and the flange are linear elastic materials for the stress analysis,
- The fluid flow through the pipe and flange is laminar,
- The relative motion between the fluid particles and the solid boundaries is zero (no slip condition),
- Crack was assumed to have the geometry of a regular cylinder,
- Dispersion coefficient of CH_4 into air is constant,
- Environmental effects such as wind conditions are ignored.

5.3. Cost Analysis

Effective detection of fugitive releases and leaks along the pipelines can save up to $251.1 million CAD/year.[1] Using COMSOL simulation and natural gas prices given from Enbridge, it is estimated that a 0.33 mm crack will result in a loss of $148 CAD/year. An EPA study conducted on a Russian compressor station showed a similar loss accounting up to $187 CAD/year. However, this study does not specify the crack size and therefore, may not be the most accurate comparison. With a proper leak detection system, loss encountered from normal operations can be reduced.

The total cost of the current prototype is approximately $ 0.15, excluding the cost of electronics, operating costs and cost of the injection mold. The breakdown of this cost is found below in Table 5-1. Conservative estimates for electronic circuitry for a sensor is about 50 cents a sensor when produced at large scale (5000 sensor/batch).

Table 5- 1: Cost breakdown of the current prototype

	Amount	**Cost (CAD)**	**Required Amount/Sensor**	**Cost/Sensor**	**Notes**
Palladium nitrate powder	2g	$178.00	0.2g to prepare 50mL of 25mM of palladium nanoparticle solution	$17.80/500 sensors	From Alfa Aesar
			14 electrode requires 100 µL of this solution	$0.0356	14 electrodes per sensor
Kapton sheet	0.002" x 12" x 12"	$20.00	Overall dimension 18mm x 21mm	$0.0814	From Professional Plastics
	0.06mm x 100mm x 33m	$30.00		$0.0034	From Spool3D Canada
Poly(vinylidene fluoride)	500g	$86.90	2mg per sensor	$0.0003	From Alfa Aesar
N-Methyl-2-pyrrolidone	25L	$2,109.45	30µL solvent required per sensor	$0.0025	From VWR
	500mL	$125.00		$0.0075	From MilliporeSigma
Ionic Liquid	250mL	$220.00	20µL solvent required per sensor	$0.0176	
Electricity During Etch				$0.005	

The cost is expected to increase with the inclusion of remote sensing and a renewable power source. However, the cost can be reduced by opting for a microcontroller and pulse detection instead of a constant voltage supply. The average cost of a microcontroller is approximately $ 0.52[139]. Using a microcontroller can reduce the total cost of the prototype to approximately $ 0.98. A fully working sensor costing less than a dollar is many folds cheaper than the current technology in use.

Chapter 6: Conclusion and Recommended Future Steps

6.1 Concluding Remarks

This research work was motivated by the fact that in 2016, Environment and Climate Change Canada (ECCC) proposed a new regulation to reduce 40-45% of the current methane (CH_4) emissions from the oil and gas (O&G) sector by 2025.[148] CH_4 is the primary component of natural gas and it is the largest source of industrial emissions from the O&G industry. It was realised from literature that an effective way to reduce fugitive release is proper and cost effective monitoring and detection. Electrochemical methane sensor were determined to be the best alternative in this case.

The early objectives of this research was to develop a prototype sensor geometry and identify material that will be incorporated in order to develop a low cost sensitive electrochemical methane sensor. A summary of the results is provided below:

- Through literature review and discussions with other researchers in Dr. Pope's lab, it was realized that interdigitated electrode structure fabricated using carbon di oxide laser can be used to develop what is known as laser induced graphene by Tour's group. An 18 x 21 mm interdigitated electrodes with 18 electrode lines with a total surface area of 2 cm^2 was developed. The interdigitated electrodes were characterized using optical microscopy, SEM and Raman spectroscopy.
- The results from the characterization helped in analysis of pore sizes in the electrodes and also confirm the porous nature of the laser induced graphene electrodes. Through literature review, it was realized that a catalyst type material is required in order to carry out any reaction on the electrode surface at room temperature. Palladium nanoparticles were determined to be the best fit.
- The porous nature of the electrodes led to the deposition of Pd nanoparticles instead of coating the entire electrode with Palladium, which would have resulted in an expensive sensor. The nanoparticles of 50 – 70 nm size range were fabricated and deposited on the finger electrode using a simple transfer technique utilizing the hydrophobic- hydrophilic property of the materials.

- The results from the deposition were confirmed by SEM imaging and EDX analysis that helped to confirm the dispersion of Pd nanoparticles on the electrodes. Room temperature ionic liquid ([EMIM][N(tF)$_2$]) is used as an electrolyte for this sensor. The challenge of ionic liquid loss on a flat surface and containing it on the finger electrodes was countered by imbibing ionic liquid in a PVDF polymer matrix by using NMP solvent. The mixture was called as solid polymer electrolyte.
- The materials were then put together in a step by step assembly. The developed prototype was tested preliminarily in a batch setup. With promising response the testing setup was modified to a flow cell setup.

After successful development of sensor material, experiments were designed and determined to analyze the response of the sensor towards methane and other gases and to determine a reaction mechanism and optimal response of the sensor at different concentrations and physical conditions. Performing these experiments resulted in the following conclusions:

- In order to determine and understand the response, the sensor was tested at a constant concentration of methane at various potentials to record the current response. A steady response was obtained at 0.6 V and above, with reduced stability with further increase in voltage.
- To understand further the reaction mechanism and behavior of sensor, it was tested in pure nitrogen environment, which resulted in realizing that the sensor is responsive only in oxygen environment. Further observation suggested moistness on the electrode surface when the sensor is run for a considerate time period. Analyzing the off gases using a FTIR concluded in water and CO_2 being the products which resulted in determining a reaction mechanism
- The characterization study helped in realizing the working of the sensor. With SEM analysis, it was realized that the ionic liquid was able to come in contact with the Pd nanoparticles at the pores in the electrode. The porous nature of electrodes and the SPE helped create a path for the gas to flow through and react at the site.
- The findings from the optimization studies and the sensitivity test resulted in determining the optimal amounts of Pd nanoparticle, ionic liquid and polymer required for the best performance. The sensitivity test resulted in determining the signal levels at each

concentration of methane. It also helped to determine the response time, rest time and the signal to noise ratio.

- Finally, electrochemical impedance spectroscopy methods were applied in estimating an equivalent circuit model that is representative of the reaction mechanism. The EIS results also help in finding the resistance associated with each concentration of methane subjected to the sensor. At last a cost estimation study is briefly conducted to estimate the cost of a sensor when fabricated at an industrial scale. It is concluded from the cost estimation study that the fabricated sensor is cheaper and hence more economical to use than other sensors available in market as of date.

The above results provide a strong argument for why laser induced graphene electrochemical methane sensors are a good fit for methane fugitive release detection in industries and other arenas. For one, they are flexible, easy to synthesize and cost effective than compared to other sensors currently in use. Second, the results from this research shows that the sensor is responsive (sensitive) to different concentrations of methane.

One of the major objectives of this research is to use the electrochemical sensor for fugitive methane release in gas pipelines. In order to fit the sensors on the flange it was realized that it was important to understand a leakage path. To utilize minimum sensors, it was important to model the gas leakage in a flange and design a structure that can focus the leakage in a particular direction in order for the sensor to detect it. Therefore another objective of this research was to model the gas leakage path, develop a design to direct the gas leakage in a particular direction and connect the sensor with electronics to make it stand alone. Based on the results, the following conclusions can be drawn.

- The model developed in COMSOL is based on laminar flow of gas through a pin hole style defect. The model is preliminary and further iterations are required to mimic a leakage type response.
- A fender type design was prepared to direct the gas towards the sensor. The design provided some results but further analysis is required for a much more sophisticated design that does not allow gas to escape in other directions.

- An Arduino based stand-alone system was hooked to the sensor to record current at constant potential. The system works well and is responsive but the current setup is arduous and expensive

To summarize, this research illustrated the fabrication of laser induced graphene based electrochemical methane sensors. The research focused into the fabrication and testing of the sensor. It also shed light on a novel technique to incorporate electrode, electrolyte and the catalyst to develop a fuel cell like system but on a thin-film. This research would encourage other researches to develop a more robust electrochemical sensor for methane and other gases and also look into new avenues of research into ionic liquid electrode interactions for electrochemical applications.

6.2. Future Work

6.2.1. Effect of interfering gases on sensor response

Since several other gases such as CO_2, CO, H_2S, NO_x and SO_x may also be present at elevated concentrations at various locations in the oil and gas industry and within pipelines, it is necessary to determine their effect on the sensor response. For example, CO is known to poison catalysts such as Pt or Pd and the extent to which this effects performance and methods to ameliorate this effect must be sought after if it is found to be a problem.

6.2.2. Effect of relative humidity on sensor response

While other gases may not be present in all cases, the sensor will experience a wide range of relative humidity depending on weather conditions. In our preliminary designs we have noticed what we believe is water being produced by the sensor, possibly through the oxidation of methane, and this floods the cell, preventing its operation. Thus the presence of water is a very important aspect of the design that needs to be investigated further.

6.2.3. Operating temperature limitations

In principle, the sensors developed will be placed on pipelines across Canada which can experience extreme temperatures below -30°C. This may impact the kinetics of the electrochemical

reactions significantly as well as potentially cause ionic liquid/polymer composite to crystallize and increase the ionic resistance in the cell.

6.2.4. Incorporating a reference electrode

Electrochemical sensors typically require a reference electrode in order to control and measure the working electrode potential. Without this, the cell potential might drift under different conditions (in particularly temperature, humidity and operating life) and not lead to a predictable current output.

6.2.5. Flange leakage modelling and plume analysis

The current modelling was based on a laminar flow assumption. In reality the flow should be turbulent due to uneven cracks and the gas escaping out should emit out as a plume. Hence, change fluid flow from laminar to turbulent for a better representation of CH_4 behaviour in natural gas pipelines. Include the influence of the environmental conditions, such as wind, that might affect the dispersion of CH_4, as that will influence the fender positioning and specifications. Currently, the wind has been modelled in COMSOL, as seen in Figure E.10 of Appendix E, but has yet to be coupled to the CH_4 flow exiting the crack. Use a more rigorous dispersion model for determining the leakage pathway of CH_4 as it exits the crack.

BIBLIOGRAPHY

[1] ICF International, "Economic Analysis of Methane Emission Reduction Opportunities in the Canadian Oil and Natural Gas Industries" 2015.

[2] J. Yang, L. Zhou, J. Huang, C. Tao, X. Li, and W. Chen, "Sensitivity enhancing of transition mode long period fiber grating as methane sensor using high refractive index polycarbonate/cryptophane A overlay deposition," *Sensors Actuators, B Chem.*, vol. 207, no. Part A, pp. 477–480, 2015.

[3] "Overview of Greenhouse Gases- Methane Emissions." [Online]. Available at: https://www.epa.gov/ghgemissions/overview-greenhouse-gases.

[4] P. . James Speight, "INFRARED ABSORPTION SPECTROSCOPY," in *Lange's Handbook of Chemistry*, 16th ed, McGraw-Hill Professional, 2005.

[5] D. R. Bloch, "Characterization," in *Organic Chemistry*, 2nd ed, McGraw-Hill Professional, 2012.

[6] M. Triki, T. Nguyen Ba, and A. Vicet, "Compact sensor for methane detection in the mid infrared region based on Quartz Enhanced Photoacoustic Spectroscopy," *Infrared Phys. Technol.*, vol. 69, pp. 74–80, 2015.

[7] C. Massie, G. Stewart, G. McGregor, and J. R. Gilchrist, "Design of a portable optical sensor for methane gas detection," *Sensors Actuators B Chem.*, vol. 113, no. 2, pp. 830–836, Feb. 2006.

[8]; Gershon J. Shugar Jack T. Ballinger, "SPECTROSCOPY," in *Chemical Technicians' Ready Reference Handbook*, 5th ed., McGraw-Hill Professional, 2011.

[9] M. Bass, "OPTICAL FIBER SENSORS," in *Handbook of Optics: Volume V – Atmospheric Optics, Modulators, Fiber Optics, X-Ray and Neutron Optics*, 3rd ed., McGraw-Hill Professional, 2010.

[10] L. Dong, W. Yin, W. Ma, L. Zhang, and S. Jia, "High-sensitivity, large dynamic range, auto-calibration methane optical sensor using a short confocal Fabry–Perot cavity," *Sensors Actuators B Chem.*, vol. 127, no. 2, pp. 350–357, 2007.

[11] C. Zheng *et al.*, "Development and field deployment of a mid-infrared methane sensor without pressure control using interband cascade laser absorption spectroscopy," *Sensors Actuators B Chem.*, vol. 244, pp. 365–372, 2017.

[12] N. P. Ayerden, M. Ghaderi, P. Enoksson, G. de Graaf, and R. F. Wolffenbuttel, "A miniaturized optical gas-composition sensor with integrated sample chamber," *Sensors Actuators B Chem.*, vol. 236, pp. 917–925, 2016.

[13] J. Chou, *Hazardous Gas Monitors – A Practical Guide to Selection, Operations and Applications*. McGraw-Hill, 1999.

[14] Sensitron, "Catalytic Sensors."

[15] S. Yamauchi, *Chemical Sensor Technology, Volume 4*, 1st ed. 1992.

[16] G. Korotcenkov, *Handbook of Gas Sensor Materials: Properites, Advantages and Shortcomings for Applications*. Springer Science & Business Media, 2013.

[17] N.-H. Park, T. Akamatsu, T. Itoh, N. Izu, and W. Shin, “Calorimetric Thermoelectric Gas Sensor for the Detection of Hydrogen, Methane and Mixed Gases,” *Sensors* , vol. 14, no. 5. 2014.

[18] G. Instrumentation, *Understanding Catalytic LEL Combustible Gas Sensor Performance. GfG Instrumentation.* .

[19] A. M. Azad, S. A. Akbar, S. G. Mhaisalkar, L. D. Birkefeld, and K. S. Goto, “Solid-State Gas Sensors - a Review,” *J. Electrochem. Soc.*, vol. 139, no. 12, pp. 3690–3704, 1992.

[20] “Detecting combustible gases and vapours - catalytic bead or infrared ?; Dragger Review,” pp. 24–29.

[21] C. K. HO, M. T. ITAMURA, M. J. KELLEY, and R. C. HUGHES, “Review of Chemical Sensors for In-Situ Monitoring of Volatile Contaminants,” no. March, 2001.

[22] R. P. Deshpande, “INTRODUCTION TO CAPACITORS,” in *Capacitors*, McGraw-Hill Professional, 2015.

[23] L. M. Dorojkine, “The non-catalytic thermal wave-based chemical gas sensor for methane and natural gas,” *Sensors Actuators B Chem.*, vol. 89, no. 1, pp. 76–85, 2003.

[24] T. Qiu-lin *et al.*, “Design, fabrication and characterization of pyroelectric thin film and its application for infrared gas sensors,” *Microelectronics J.*, vol. 40, no. 1, pp. 58–62, 2009.

[25] Y. Querner, V. Norkus, and G. Gerlach, “High-sensitive pyroelectric detectors with internal thermal amplification,” *Sensors Actuators A Phys.*, vol. 172, no. 1, pp. 169–174, 2011.

[26] Q. Tan *et al.*, “Three-gas detection system with IR optical sensor based on NDIR technology,” *Opt. Lasers Eng.*, vol. 74, pp. 103–108, 2015.

[27] M. H. Lee, R. Guo, and A. S. Bhalla, “Pyroelectric Sensors,” no. i, pp. 229–230, 1998.

[28] Z. Hdr, Q. Tan, Z. Wendong, X. Chenyang, G. Tao, and X. Jijun, *Miniature low-power IR monitor for methane detection*, vol. 44. 2011.

[29] Z. Zhu, Y. Xu, and B. Jiang, “A one ppm NDIR methane gas sensor with single frequency filter denoising algorithm,” *Sensors (Switzerland)*, vol. 12, no. 9, pp. 12729–12740, 2012.

[30] M. . Bauersfeld, “Semiconductor Gas Sensors Using Thin and Thick Film Technology,” *Fraunhofer IPM, (n.d.).*, pp. 2–3.

[31] G. F. Fine, L. M. Cavanagh, A. Afonja, and R. Binions, “Metal Oxide Semi-Conductor Gas Sensors in Environmental Monitoring,” *Sensors* , vol. 10, no. 6. 2010.

[32] V. Milosavljevic, *Electronic Gas Sensors and Detectors – Classification and Operating Principles*. 2012.

[33] M. S. Kanan, M. O. El-Kadri, A. I. Abu-Yousef, and C. M. Kanan, “Semiconducting Metal Oxide Based Sensors for Selective Gas Pollutant Detection,” *Sensors* , vol. 9, no. 10. 2009.

[34] K. Wetchakun *et al.*, “Semiconducting metal oxides as sensors for environmentally hazardous gases,” *Sensors Actuators B Chem.*, vol. 160, no. 1, pp. 580–591, 2011.

[35] M. . Grace, R; Hibner, J; Portnoff, “Measurement and Analysis of Vapor Sensors Used at

Underground Storage Tank Sites," *Carnegie Mellon Res. Inst.*, 1995.

[36] K. Wetchakun *et al.*, *Semiconductor Metal Oxides as Sensors for Environmentally Hazardous Gases*, vol. 160. 2011.

[37] M. Fleischer, "Modern Gas Sensors Allow Innovation," 2009.

[38] F. S. Carrasco, J. Ramon, M. Lleonart, C. Qu, and F. S. Carrasco, "Tin Oxide Gas Sensors : An Electrochemical Approach," 2002.

[39] E. Bakker and Y. Qin, "Electrochemical sensors," *Anal Chem*, vol. 78, no. 12, pp. 3965–3984, 2006.

[40] P. K. Sekhar, J. Kysar, E. L. Brosha, and C. R. Kreller, "Development and testing of an electrochemical methane sensor," *Sensors Actuators, B Chem.*, vol. 228, pp. 162–167, 2016.

[41] A. T. Ashcroft *et al.*, "Selective oxidation of methane to synthesis gas using transition metal catalysts," *Nature*, vol. 344, p. 319, Mar. 1990.

[42] P. Jacquinot, B. Müller, B. Wehrli, and P. C. Hauser, "Determination of methane and other small hydrocarbons with a platinum-Nafion electrode by stripping voltammetry," *Anal. Chim. Acta*, vol. 432, no. 1, pp. 1–10, 2001.

[43] A. T. Ashcroft, A. K. Cheetham, M. L. H. Green, and P. D. F. Vernon, "Partial oxidation of methane to synthesis gas using carbon dioxide," *Nature*, vol. 352, p. 225, Jul. 1991.

[44] S. Z. and J. R. S. T. Otagawa, "Electrochemical Oxidation of Methane in Nonaqueous Electrolytes at Room Temperature," *J. Electrochem. Soc.*, vol. 132, no. 12, pp. 2951–2957, 1985.

[45] D. Wei and A. Ivaska, "Applications of ionic liquids in electrochemical sensors.," *Anal. Chim. Acta*, vol. 607, no. 2, pp. 126–135, Jan. 2008.

[46] L. E. Barrosse-Antle, A. M. Bond, R. G. Compton, A. M. O'Mahony, E. I. Rogers, and D. S. Silvester, "Voltammetry in room temperature ionic liquids: comparisons and contrasts with conventional electrochemical solvents.," *Chem. Asian J.*, vol. 5, no. 2, pp. 202–230, Feb. 2010.

[47] M. Galiński, A. Lewandowski, and I. Stępniak, "Ionic liquids as electrolytes," *Electrochim. Acta*, vol. 51, no. 26, pp. 5567–5580, 2006.

[48] M. Freemantle, *An Introduction to Ionic Liquids*. The Royal Society of Chemistry, 2009.

[49] M. Armand, F. Endres, D. R. MacFarlane, H. Ohno, and B. Scrosati, "Ionic-liquid materials for the electrochemical challenges of the future.," *Nat. Mater.*, vol. 8, no. 8, pp. 621–629, Aug. 2009.

[50] M. Díaz, A. Ortiz, and I. Ortiz, *Progress in the use of ionic liquids as electrolyte membranes in fuel cells*, vol. 469. 2014.

[51] X. Chen, J. Zhu, R. Tian, and C. Yao, "Bienzymatic glucose biosensor based on three dimensional macroporous ionic liquid doped sol–gel organic–inorganic composite," *Sensors Actuators B Chem.*, vol. 163, no. 1, pp. 272–280, 2012.

[52] S. S. Silva, A. R. C. Duarte, A. P. Carvalho, J. F. Mano, and R. L. Reis, "Green processing of porous chitin structures for biomedical applications combining ionic liquids and supercritical fluid technology.," *Acta Biomater.*, vol. 7, no. 3, pp. 1166–1172, Mar. 2011.

[53] M. Steichen, J. Larsen, L. Gütay, S. Siebentritt, and P. J. Dale, “Preparation of CuGaSe 2 absorber layers for thin fi lm solar cells by annealing of ef fi ciently electrodeposited Cu – Ga precursor layers from ionic liquids,” *Thin Solid Films*, vol. 519, no. 21, pp. 7254–7258, 2011.

[54] L. Vidal, M.-L. Riekkola, and A. Canals, “Ionic liquid-modified materials for solid-phase extraction and separation: a review.,” *Anal. Chim. Acta*, vol. 715, pp. 19–41, Feb. 2012.

[55] R. G. Buzzeo, M.C.; Hardacre, Christopher; Compton, “Use of room temperature ionic liquids in gas sensor design.,” in *Analytical Chemistry*, 76th ed., 2004, pp. 4583–4588.

[56] L. Xiong and R. G. Compton, “Amperometric Gas detection : A Review,” vol. 9, pp. 7152–7181, 2014.

[57] F. Faridbod, “Application of Room Temperature Ionic Liquids in Electrochemical Sensors and Biosensors,” M. R. Ganjali, Ed. Rijeka: IntechOpen, 2011, p. Ch. 29.

[58] D. S. Silvester, “Recent advances in the use of ionic liquids for electrochemical sensing,” *Analyst*, vol. 136, no. 23, pp. 4871–4882, 2011.

[59] Xiaoyi Mu *et al.*, “Fabrication of a miniaturized room temperature ionic liquid gas sensor for human health and safety monitoring,” *IEEE Biomed. Circuits Syst. Conf.*, vol. 1, pp. 140–143, 2012.

[60] M. T. Carter, J. R. Stetter, M. W. Findlay, and V. Patel, “Amperometric Gas Sensors with Ionic Liquid Electrolytes,” *ECS Trans.* , vol. 58, no. 34, pp. 7–18, Apr. 2014.

[61] J. Xiaobo, B. Craig E., S. Debbie S., A. Leigh, H. Christopher, and C. Richard G., “Electrochemical Ammonia Gas Sensing in Nonaqueous Systems: A Comparison of Propylene Carbonate with Room Temperature Ionic Liquids,” *Electroanalysis*, vol. 19, no. 21, pp. 2194–2201, Oct. 2007.

[62] M. T. Carter, J. Stetter, M. Findlay, and V. Patel, “Printed Amperometric Gas Sensors,” *Meet. Abstr.* , vol. MA2012-02, no. 56, p. 3859, Jun. 2012.

[63] X.-J. Huang, L. Aldous, A. M. O’Mahony, F. J. del Campo, and R. G. Compton, “Toward Membrane-Free Amperometric Gas Sensors: A Microelectrode Array Approach,” *Anal. Chem.*, vol. 82, no. 12, pp. 5238–5245, Jun. 2010.

[64] R. Toniolo, N. Dossi, A. Pizzariello, A. P. Doherty, S. Susmel, and G. Bontempelli, *An oxygen amperometric gas sensor based on its electrocatalytic reduction in room temperature ionic liquids*, vol. 670. 2012.

[65] S. H. M. A. G. Zevenbergen, D. Wouters, V.-A. T. Dam and and M. C.-C. Brongersma, “Electrochemical Sensing of Ethylene Employing a Thin Ionic-Liquid Layer,” *Anal. Chem.*, vol. 83, pp. 6300–6307, 2011.

[66] Z. Wang *et al.*, “Methane–oxygen electrochemical coupling in an ionic liquid: a robust sensor for simultaneous quantification,” *Analyst*, vol. 139, no. 20, pp. 5140–5147, 2014.

[67] P. Kuberský, J. Altšmíd, A. Hamáček, S. Nešpůrek, and O. Zmeškal, “An Electrochemical NO_2 Sensor Based on Ionic Liquid: Influence of the Morphology of the Polymer Electrolyte on Sensor Sensitivity,” *Sensors (Basel).*, vol. 15, no. 11, pp. 28421–28434, Nov. 2015.

[68] M. Nádherná, F. Opekar, and J. Reiter, *Ionic liquid–polymer electrolyte for amperometric solid-*

state NO_2 sensor, vol. 56. 2011.

[69] M. Nádherná, F. Opekar, J. Reiter, and K. Štulík, *A planar, solid-state amperometric sensor for nitrogen dioxide, employing an ionic liquid electrolyte contained in a polymeric matrix*, vol. 161. 2012.

[70] P. Kuberský, A. Hamáček, S. Nespůrek, R. Soukup, and R. Vik, "Effect of the geometry of a working electrode on the behavior of a planar amperometric NO_2 sensor based on solid polymer electrolyte," *Sensors Actuators, B Chem.*, vol. 187, pp. 546–552, 2013.

[71] S. Yao and S. JR, "Solid Electrolyte Sensors for Emissions Monitoring," *Illinois Inst. Technol.*, pp. 2–3, 2000.

[72] B. K. Narayanan, S. A. Akbar, and P. K. Dutta, "A phosphate-based proton conducting solid electrolyte hydrocarbon gas sensor," *Sensors Actuators B Chem.*, vol. 87, no. 3, pp. 480–486, 2002.

[73] B. Zhu and B.-E. Mellander, "Proton conduction in salt-ceramic composite systems," *Solid State Ionics*, vol. 77, pp. 244–249, 1995.

[74] B. C. T. A. Hooper, P. Mcgeehin, K.T. Harrison, *Solid State Chem.* 1978.

[75] G. Alberti, A. Carbone, and R. Palombari, *Solid state potentiometric sensor at medium temperatures (150–300°C) for detecting oxidable gaseous species in air*, vol. 75. 2001.

[76] S. Iijima, "Helical microtubules of graphitic carbon," *Nature*, vol. 354, p. 56, Nov. 1991.

[77] L. X. Duy, Z. Peng, Y. Li, J. Zhang, Y. Ji, and J. M. Tour, "Laser-induced graphene fibers," *Carbon N. Y.*, vol. 126, pp. 472–479, 2018.

[78] K. S. Novoselov *et al.*, "Electric field effect in atomically thin carbon films.," *Science*, vol. 306, no. 5696, pp. 666–669, Oct. 2004.

[79] F. Wang *et al.*, "Laser-induced graphene: preparation, functionalization and applications," *Mater. Technol.*, vol. 33, no. 5, pp. 340–356, Apr. 2018.

[80] M. D. Stoller, S. Park, Y. Zhu, J. An, and R. S. Ruoff, "Graphene-Based Ultracapacitors," *Nano Lett.*, vol. 8, no. 10, pp. 3498–3502, Oct. 2008.

[81] A. S. Mayorov *et al.*, "Micrometer-Scale Ballistic Transport in Encapsulated Graphene at Room Temperature," *Nano Lett.*, vol. 11, no. 6, pp. 2396–2399, Jun. 2011.

[82] A. A. Balandin, "Thermal properties of graphene and nanostructured carbon materials," *Nat. Mater.*, vol. 10, p. 569, Jul. 2011.

[83] R. R. Nair *et al.*, "Fine Structure Constant Defines," vol. 320, no. June, pp. 2–3, 2008.

[84] D. C. Marcano *et al.*, "Improved Synthesis of Graphene Oxide," *ACS Nano*, vol. 4, no. 8, pp. 4806–4814, Aug. 2010.

[85] K. Hata, D. N. Futaba, K. Mizuno, T. Namai, M. Yumura, and S. Iijima, "Water-Assisted Highly Efficient Synthesis of Impurity-Free Single-Walled Carbon Nanotubes," *Science (80-.).*, vol. 306, no. 5700, p. 1362 LP-1364, Nov. 2004.

[86] J. Lin *et al.*, “Laser-induced porous graphene films from commercial polymers,” *Nat. Commun.*, 2015.

[87] M. Schumann, R. Sauerbrey, and M. C. Smayling, “Permanent increase of the electrical conductivity of polymers induced by ultraviolet laser radiation,” *Appl. Phys. Lett.*, vol. 58, no. 4, pp. 428–430, Jan. 1991.

[88] M. Beidaghi and Y. Gogotsi, “Capacitive energy storage in micro-scale devices: recent advances in design and fabrication of micro-supercapacitors,” *Energy Environ. Sci.*, vol. 7, no. 3, pp. 867–884, 2014.

[89] W. Zhong-Shuai *et al.*, “Layer-by-Layer Assembled Heteroatom-Doped Graphene Films with Ultrahigh Volumetric Capacitance and Rate Capability for Micro-Supercapacitors,” *Adv. Mater.*, vol. 26, no. 26, pp. 4552–4558, Apr. 2014.

[90] J. Lin *et al.*, “3-Dimensional graphene carbon nanotube carpet-based microsupercapacitors with high electrochemical performance.,” *Nano Lett.*, vol. 13, no. 1, pp. 72–78, Jan. 2013.

[91] M. Li, Y.-T. Li, D.-W. Li, and Y.-T. Long, “Recent developments and applications of screen-printed electrodes in environmental assays—A review,” *Anal. Chim. Acta*, vol. 734, pp. 31–44, 2012.

[92] Y. Ye-Lin, J. V. Lidon-Roger, E. Garcia-Breijo, J. Garcia-Casado, and G. Prats-Boluda, “A comparative analysis of printing techniques by using an active concentric ring electrode for bioelectrical recording,” *Microelectron. Int.*, vol. 32, no. 2, pp. 103–107, Apr. 2015.

[93] O.-S. Kwon *et al.*, “Fabrication and characterization of inkjet-printed carbon nanotube electrode patterns on paper,” *Carbon N. Y.*, vol. 58, pp. 116–127, 2013.

[94] N. T. Dinh *et al.*, “High-resolution inkjet printing of conductive carbon nanotube twin lines utilizing evaporation-driven self-assembly,” *Carbon N. Y.*, vol. 96, pp. 382–393, 2016.

[95] M. F. El-Kady and R. B. Kaner, “Scalable fabrication of high-power graphene micro-supercapacitors for flexible and on-chip energy storage.,” *Nat. Commun.*, vol. 4, p. 1475, 2013.

[96] M. F. El-Kady and R. B. Kaner, “Direct Laser Writing of Graphene Electronics,” *ACS Nano*, vol. 8, no. 9, pp. 8725–8729, Sep. 2014.

[97] V. Strong *et al.*, “Patterning and electronic tuning of laser scribed graphene for flexible all-carbon devices.,” *ACS Nano*, vol. 6, no. 2, pp. 1395–1403, Feb. 2012.

[98] J. Lin, “Laser-induced porous graphene films from commercial polymers,” *Nat. Commun*, vol. 5, p. 5714.

[99] R. Ye, “Laser-Induced Graphene Formation on Wood,” *Adv. Mater.*, vol. 29, no. 37, p. 1702211.

[100] M. F. El-Kady, V. Strong, S. Dubin, and R. B. Kaner, “Laser scribing of high-performance and flexible graphene-based electrochemical capacitors.,” *Science*, vol. 335, no. 6074, pp. 1326–1330, Mar. 2012.

[101] Z. Peng *et al.*, “Flexible Boron-Doped Laser-Induced Graphene Microsupercapacitors,” *ACS Nano*, vol. 9, no. 6, pp. 5868–5875, Jun. 2015.

[102] G. Joseph, A. A. Kirubaraj, D. Devaprakasam, and C. Engineering, “FABRICATION OF

FLEXIBLE SUPER CAPACITOR USING LASER."

[103] C. Petridis *et al.*, "Post-fabrication, in situ laser reduction of graphene oxide devices," *Appl. Phys. Lett.*, vol. 102, no. 9, p. 93115, Mar. 2013.

[104] J. Cai, C. Lv, and A. Watanabe, "Cost-effective fabrication of high-performance flexible all-solid-state carbon micro-supercapacitors by blue-violet laser direct writing and further surface treatment," *J. Mater. Chem. A*, vol. 4, no. 5, pp. 1671–1679, 2016.

[105] O. S. Sizuka, R. M. Cerqueira, O. F. Dondeo, D. A. José, and B. E. Cocchieri, "Viscosity, pH, and moisture effect in the porosity of poly(furfuryl alcohol)," *J. Appl. Polym. Sci.*, vol. 128, no. 3, pp. 1680–1686, Jul. 2012.

[106] Y. Li *et al.*, "Laser-Induced Graphene in Controlled Atmospheres: From Superhydrophilic to Superhydrophobic Surfaces.," *Adv. Mater.*, vol. 29, no. 27, Jul. 2017.

[107] A. Azhari, E. Marzbanrad, D. Yilman, E. Toyserkani, and M. A. Pope, "Binder-jet powder-bed additive manufacturing (3D printing) of thick graphene-based electrodes," *Carbon N. Y.*, vol. 119, pp. 257–266, Aug. 2017.

[108] Z. Lei, B. Chen, Y.-M. Koo, and D. R. MacFarlane, "Introduction: Ionic Liquids," *Chem. Rev.*, vol. 117, no. 10, pp. 6633–6635, May 2017.

[109] H. Zhao, "Review: Current studies on some physical properties of ionic liquids," *Phys. Chem. Liq.*, vol. 41, no. 6, pp. 545–557, Dec. 2003.

[110] Z. Wang *et al.*, "Methane–oxygen electrochemical coupling in an ionic liquid: a robust sensor for simultaneous quantification," *Analyst*, vol. 139, no. 20, pp. 5140–5147, 2014.

[111] B. Digital, "An electrochemical gas sensor based on paper supported room temperature ionic liquids," pp. 153–158, 2012.

[112] H. Wan, H. Yin, L. Lin, X. Zeng, and A. J. Mason, "Miniaturized planar room temperature ionic liquid electrochemical gas sensor for rapid multiple gas pollutants monitoring," *Sensors Actuators, B Chem.*, vol. 255, pp. 638–646, 2018.

[113] J. Xia, F. Zhu, S. Zhang, A. Kolomenskii, and H. Schuessler, "A ppb level sensitive sensor for atmospheric methane detection," *Infrared Phys. Technol.*, vol. 86, pp. 194–201, 2017.

[114] E. B. Secor, P. L. Prabhumirashi, K. Puntambekar, M. L. Geier, and M. C. Hersam, "Inkjet Printing of High Conductivity, Flexible Graphene Patterns," *J. Phys. Chem. Lett.*, vol. 4, no. 8, pp. 1347–1351, Apr. 2013.

[115] R. P. Tortorich and J.-W. Choi, "Inkjet Printing of Carbon Nanotubes," *Nanomaterials*, vol. 3, no. 3, pp. 453–468, Sep. 2013.

[116] L. Li, "High-Performance Pseudocapacitive Microsupercapacitors from Laser-Induced Graphene," *Adv. Mater.*, vol. 28, no. 5, pp. 838–845.

[117] J. Zhang, C. Zhang, J. Sha, H. Fei, Y. Li, and J. M. Tour, "Efficient Water-Splitting Electrodes Based on Laser-Induced Graphene," *ACS Appl. Mater. Interfaces*, vol. 9, no. 32, pp. 26840–26847, 2017.

[118] J. Zhang, M. Ren, Y. Li, and J. M. Tour, "In Situ Synthesis of Efficient Water Oxidation Catalysts

in Laser-Induced Graphene," *ACS Energy Lett.*, vol. 3, no. 3, pp. 677–683, 2018.

[119] J. Zhang, M. Ren, L. Wang, Y. Li, B. I. Yakobson, and J. M. Tour, "Oxidized Laser-Induced Graphene for Efficient Oxygen Electrocatalysis," *Adv. Mater.*, vol. 30, no. 21, pp. 1–7, 2018.

[120] G. Xu, Z. A. Jarjes, V. Desprez, P. A. Kilmartin, and J. Travas-Sejdic, "Sensitive, selective, disposable electrochemical dopamine sensor based on PEDOT-modified laser scribed graphene," *Biosens. Bioelectron.*, vol. 107, no. November 2017, pp. 184–191, 2018.

[121] F. Tehrani and B. Bavarian, "Facile and scalable disposable sensor based on laser engraved graphene for electrochemical detection of glucose," *Sci. Rep.*, vol. 6, no. January, pp. 1–10, 2016.

[122] S. Luo, P. T. Hoang, and T. Liu, "Direct laser writing for creating porous graphitic structures and their use for flexible and highly sensitive sensor and sensor arrays," *Carbon N. Y.*, vol. 96, pp. 522–531, 2016.

[123] C. M. Tittle, D. Yilman, M. A. Pope, and C. J. Backhouse, "Robust Superhydrophobic Laser-Induced Graphene for Desalination Applications," *Adv. Mater. Technol.*, vol. 3, no. 2, pp. 1–10, 2018.

[124] Z. Wang and X. Zeng, "Bis(trifluoromethylsulfonyl)imide (NTf2)-Based Ionic Liquids for Facile Methane Electro-Oxidation on Pt," *J. Electrochem. Soc.*, vol. 160, no. 9, pp. H604–H611, 2013.

[125] and J. M. T. Y. Chyan, R. Ye, Y. Li, S. P. Singh, C. J. Arnusch, "Laser-Induced Graphene by Multiple Lasing: Toward Electronics on Cloth, Paper, and Food," *ACS Nano*, vol. 12, no. 3, pp. 2176–2183.

[126] A. C. Ferrari and J. Robertson, "Interpretation of Raman spectra of disordered and amorphous carbon."

[127] M. Wall, "The Raman Spectroscopy of Graphene and the Determination of Layer Thickness Raman Spectroscopy and the Raman Spectrum of Graphene."

[128] M. Wall, "The Raman Spectroscopy of Graphene and the Determination of Layer Thickness Raman Spectroscopy and the Raman Spectrum of Graphene."

[129] A. C. Ferrari *et al.*, "Raman Spectrum of Graphene and Graphene Layers."

[130] C. Bosch-Navarro, J. P. Rourke, and N. R. Wilson, "Controlled electrochemical and electroless deposition of noble metal nanoparticles on graphene," *RSC Adv.*, vol. 6, no. 77, pp. 73790–73796, 2016.

[131] V. P. Zhdanov, "Simulation of the effect of surface-oxide formation on bistability in CO oxidation on Pt-group metals," *J. Chem. Phys.*, vol. 126, no. 7, 2007.

[132] J. M. vo. Niessen, "The influence of physisorption and the Eley-Rideal mechanism on a surface reaction: CO + O_2," *Chem. Phys.*, vol. 156, no. 1, pp. 63–69, 1991.

[133] M. Systems, "Current Fluctuation Measurements of Amperometric Gas," vol. 23, no. 4, pp. 531–543, 2016.

[134] F. Magalhães, J. P. Carvalho, L. A. Ferreira, F. M. Araújo, and J. L. Santos, "Methane detection system based on wavelength modulation spectroscopy and hollow-core fibres," *Proc. IEEE Sensors*, pp. 1277–1280, 2008.

[135] G. Gong and H. Zhu, “Development of highly sensitive sensor system for methane utilizing cataluminescence,” *Luminescence*, vol. 31, no. 1, pp. 183–189, 2016.

[136] J. Z. Xiao-Zi (Riny) Yuan, Chaojie Song, Haijiang Wang, *Electrochemical Impedance Spectroscopy in PEM Fuel Cells: Fundamentals and Applications*. Springer, 2010.

[137] M. I. Prodromidis, “Impedimetric immunosensors-A review,” *Electrochim. Acta*, vol. 55, no. 14, pp. 4227–4233, 2010.

[138] C.M.A. Brett and A.M. Oliveira-Brett, *Electrochemistry: Principles, Methods and Applications*. Oxford, UK: Oxford University Press, 1993.

[139] “MCU Microcontrollers – Cost Climbs.,” 2016.

[140] “Structural Mechanics Module User’s Guide; COMSOL,” 2015.

[141] “Prestressed Bolts in a Tube Connection. COMSOL.”

[142] “Bolted Joint Design. (n.d). Fastenal Engineering & Design Support.”

[143] “CFD Module User’s Guide v5.3.,” 2017.

[144] R. Chemicoff, W.P., Engblom, L., Houf, W., Marchi, C.S., & Schefer, “Characterization of Leaks from Compressed Hydrogen Systems and Related Components.,” 2005.

[145] “CFD Module User’s Guide v5.3. COMSOL,” 2017.

[146] “Methane Leak Measurements at Selected Natural Gas Pipeline Compressor Stations in Russia.,” 1996.

[147] E. Lazzari, S., Perini, K., Roccotiello, E., & Rossi di Schio, “Simplified CFD Modelling of Air Pollution Reduction by Means of Greenery in Urban Canyons.,” 2016.

[148] “Proposed Methane Regulations.,” 2017.

Appendix A: Criteria and Constraints

After completing a literature review of six various types of sensors: solid electrolyte, semiconducting oxide, catalytic combustion, optical, pyroelectric, and ionic liquid sensors, the following constraints and criteria were determined:

- requires high selectivity and sensitivity to CH_4,
- robust (temperature, corrosion, and poison resistant),
- inexpensive and easy to manufacture,
- and lab-scale sensing technology that could be easily implemented for industry-use.

Since the sensor will be implemented within a natural gas pipeline (i.e. hydrocarbon environment), it will be necessary to have high selectivity of CH_4. The sensor will also be required to detect small amounts of CH_4 leaks to properly capture the leaks and reduce the amount of greenhouse gas emitted. The lifetime and fouling resistance are important factors as the sensor may be placed in high-stress and remote conditions. For the sensor to be suitable for industrial usage, it should be easy to implement from lab-scale testing and be inexpensive to produce (in order to be competitive in the market). Finally, the sensing technology should be current and proven to be competitive in the market. Table B-1 is the decision matrix for selecting a suitable sensor based on our constraints and criteria with a score is given from 1 to 5 (worst to best).

Table A- 1: Decision Matrix for Sensor Selection

Criteria	Solid Electrolyte	Semiconducting Oxide	Catalytic Combustion	Optical	Pyroelectric	Ionic Liquid
Selectivity	4	2	2	5	3	3
Sensitivity	4	3	3	5	4	3
Fouling Resistance	4	2	1	4	3	2
Lifetime	3	3	2	5	3	2
Manufacturability	4	5	5	1	4	3
Cost	4	5	4	1	3	4
Technology Readiness	4	5	3	4	3	5
Suitability for Application	5	3	1	4	3	1

Final Score	**32**	28	21	29	26	23

Criteria	**Score: 5**	**Score: 4**	**Score: 3**	**Score: 2**	**Score: 1**
Selectivity	Outstanding selectivity of CH_4. Able to detect within complex hydrocarbon environment with no deviations due to interferences (cross-selectivity, humidity effects, etc.).	Excellent selectivity of CH_4. Able to detect within hydrocarbon environment with little deviations due to interferences (cross-selectivity, humidity effects, etc.).	Good selectivity of CH_4. Able to detect within hydrocarbon environment with some deviations due to interferences (cross-selectivity, humidity effects, etc.).	Acceptable selectivity of CH_4. Able to detect within hydrocarbon environment with deviations due to interferences (cross-selectivity, humidity effects, etc.).	Poor selectivity of CH_4. Unable to detect within hydrocarbon environment (cross-selectivity, humidity effects, etc.).
Sensitivity	Outstanding sensitivity of CH_4. Can detect down to 10ppm.	Excellent sensitivity of CH_4. Can detect down to 50ppm.	Good sensitivity of CH_4. Can detect down to 100ppm.	Acceptable sensitivity of CH_4. Can detect down to 500ppm.	Poor sensitivity of CH_4. Can detect above 1000ppm.
Fouling Resistance	Outstanding resistance to temperature changes, corrosion, and poisoning resistance.	Excellent resistance to temperature changes, corrosion and poisoning resistance.	Good resistance to corrosion and poisoning resistance. Lacking in temperature change resistance.	Acceptable resistance to corrosion and poisoning resistance. Lacking in temperature change resistance.	Poor resistance to temperature changes, corrosion, and poisoning resistance.
Lifetime	Outstanding lifetime (5+ years).	Excellent lifetime (3-5 years).	Good lifetime (2 years).	Acceptable lifetime (1 year).	Poor lifetime (< 1 year).
Manufacturability	Outstanding manufacturability with no difficulty in materials and equipment.	Excellent manufacturability with little difficulty in materials and equipment.	Good manufacturability with some difficulty in materials and equipment.	Difficult to manufacture with considerable difficulty in materials and equipment.	Extremely complex steps to manufacture. Requires special equipment and difficult materials.
Cost	Outstanding cost to produce (< $1 per unit).	Excellent cost to produce ($1 - $10 per unit).	Good cost to produce ($10 - $50 per unit).	Acceptable cost to produce ($50 - $100 per unit).	Poor cost to produce ($100+ per unit).
Technology Readiness	Outstanding readiness with technology being standard in industry.	Excellent readiness with technology	Good readiness with technology being known and somewhat	Acceptable readiness with technology known but not utilized in industry.	Poor readiness with technology under

Criteria	Score: 5	Score: 4	Score: 3	Score: 2	Score: 1
		being utilized in industry.	utilized in industry.		development and not utilized in industry.
Suitability for Application	Outstanding applicability to oil and gas pipeline for remote leak detection. Easy installation and requires minimal maintenance.	Excellent applicability to oil and gas pipeline for remote leak detection. Easy installation and requires little maintenance.	Good applicability to oil and gas pipeline for remote leak detection. Simple installation and requires some maintenance.	Acceptable applicability to oil and gas pipeline for remote leak detection. Difficult installation and requires frequent maintenance.	Poor applicability to oil and gas pipeline for remote leak detection. Difficult installation and requires weekly/monthly maintenance.

Appendix B: Additional Figures, Data and Drawings

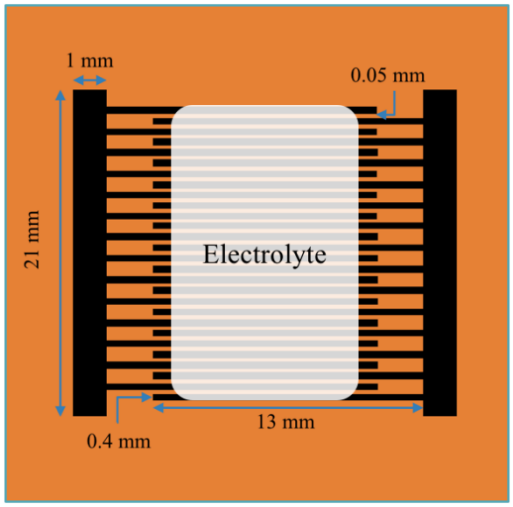

Figure B- 1: Sensor configuration with baseline dimensions

Table B- 1: Specifications of the 5 different sensors tested

Parameter	**Sensor 1 (S1) (Baseline)**	**Sensor 2 (S2)**	**Sensor 3 (S3)**	**Sensor 4 (S4)**	**Sensor 5 (S5)**
Overall Dimension	18mm x 21mm				
# of Fingers	14				
Overall Surface Area of Interdigitated Electrodes	1.988cm^2				
2 Major Side Electrode Dimensions	21mm x 1mm				
Each Interdigitated Finger Electrode Dimension	13mm x 0.4mm		13mm x 0.8mm (2x width)		
Spacing between Fingers	0.05mm	0.1mm (2x spacing)			
Electrolyte Thickness	40-50µm			20-30µm	70-80µm

Table B- 2: CH_4 concentration data

CH4 cylinder	
Concentration(ppm)	500
flow rate, ml/min	50
After mixing with air	
CH4 concentration, ppm	Air flow rate
500	0
200	75
150	117
100	200
50	450
40	575
30	783
20	1200
10	2450
5	4950
2.5	9950
1	24950
0.5	49950
0.1	249950
0.05	499950
Air flow controller	
MFC step increment (0.1%), ml/min	20
MFC starting point (1%) flow rate	200
Air flow rate range, ml/min	200-20000

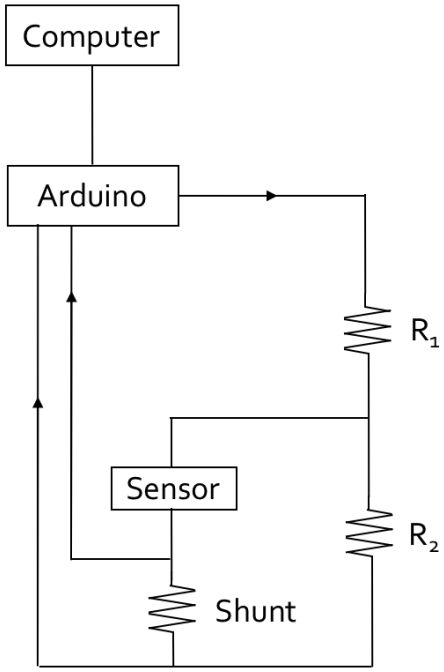

Figure B- 2: Schematic of the electrical circuit

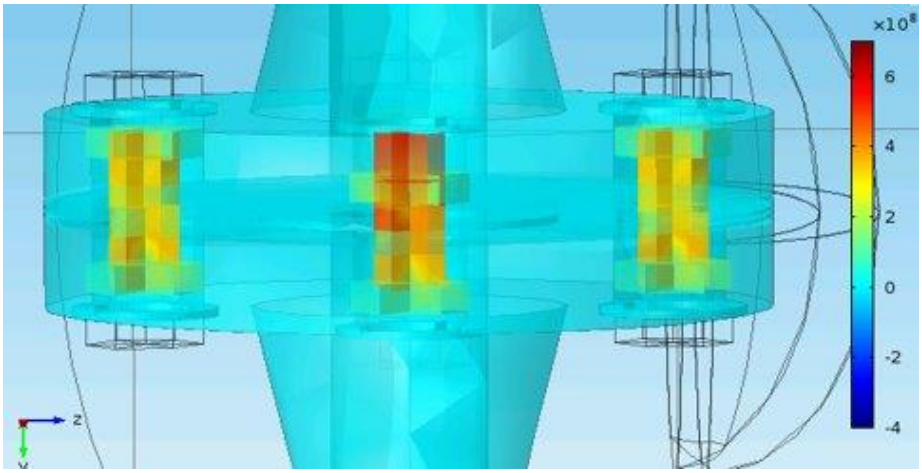

Figure B- 3: Stress development due to pre-stressed bolts

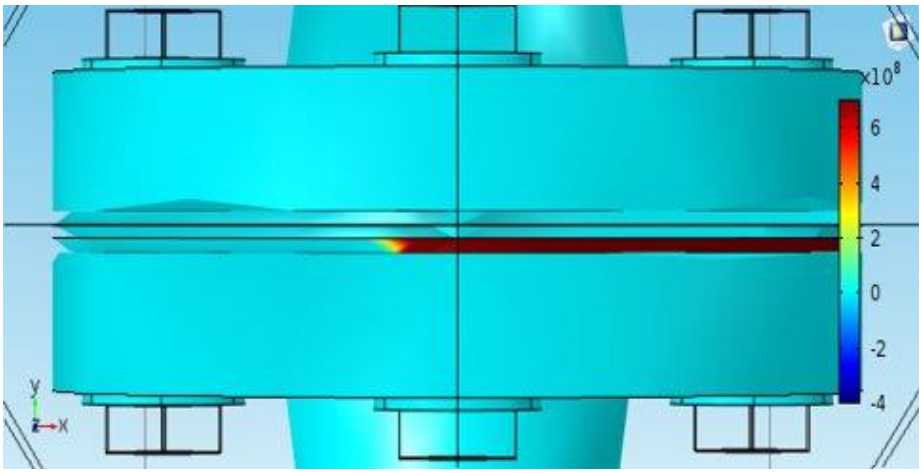

Figure B- 4: Stress development due to gasket displacement

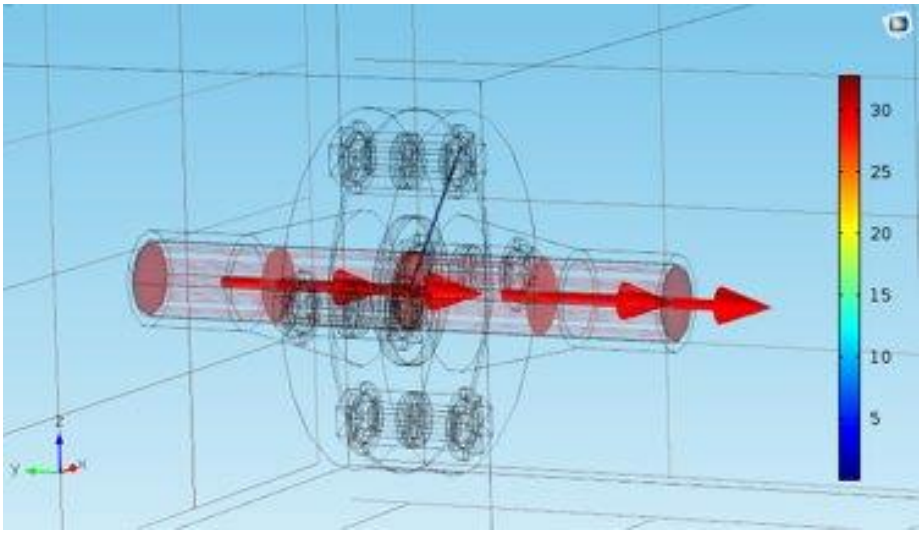

Figure B- 5: Internal flow of CH_4 gas through pipe

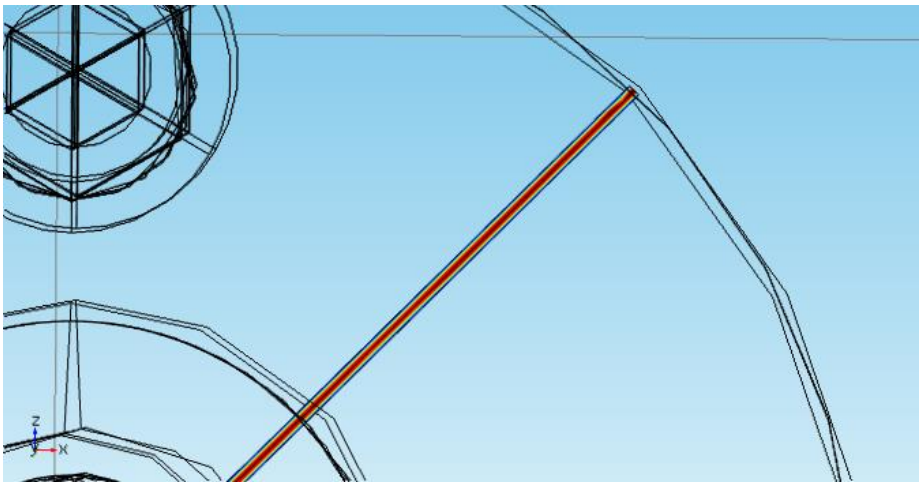

Figure B- 6: Internal flow of CH_4 gas through crack

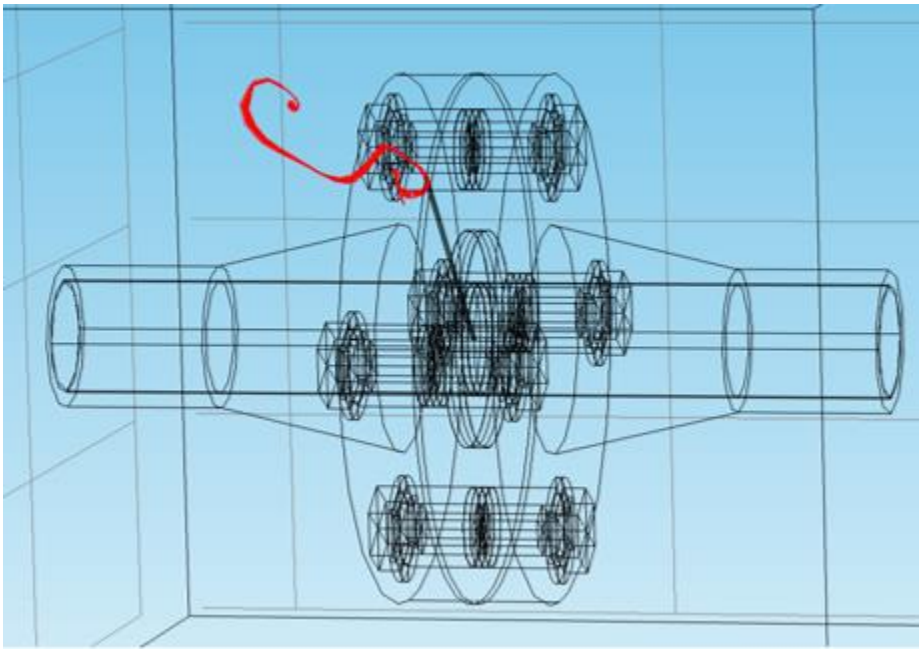

Figure B- 7: Dispersion path of CH_4 from top leak

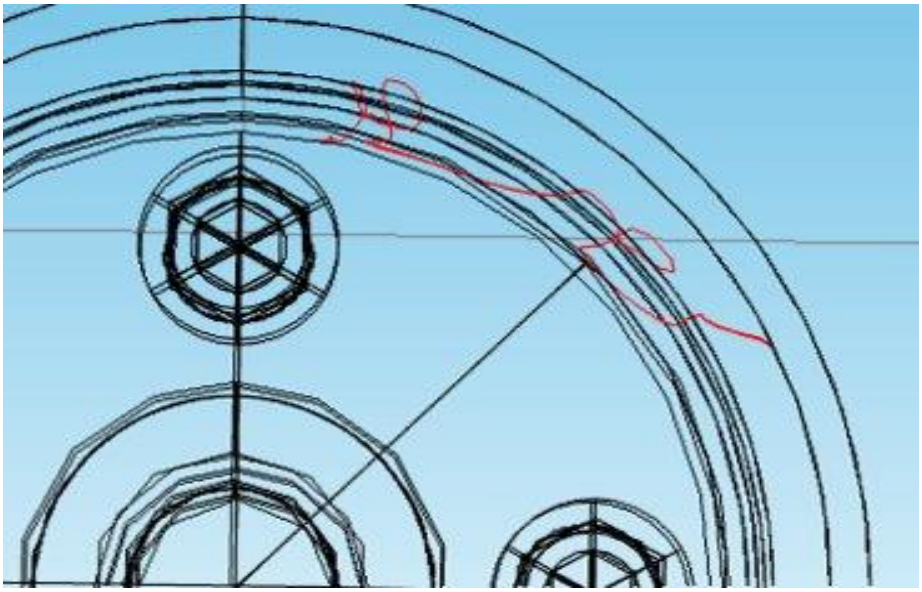

Figure B- 8: Dispersion path of CH_4 from top leak with fender

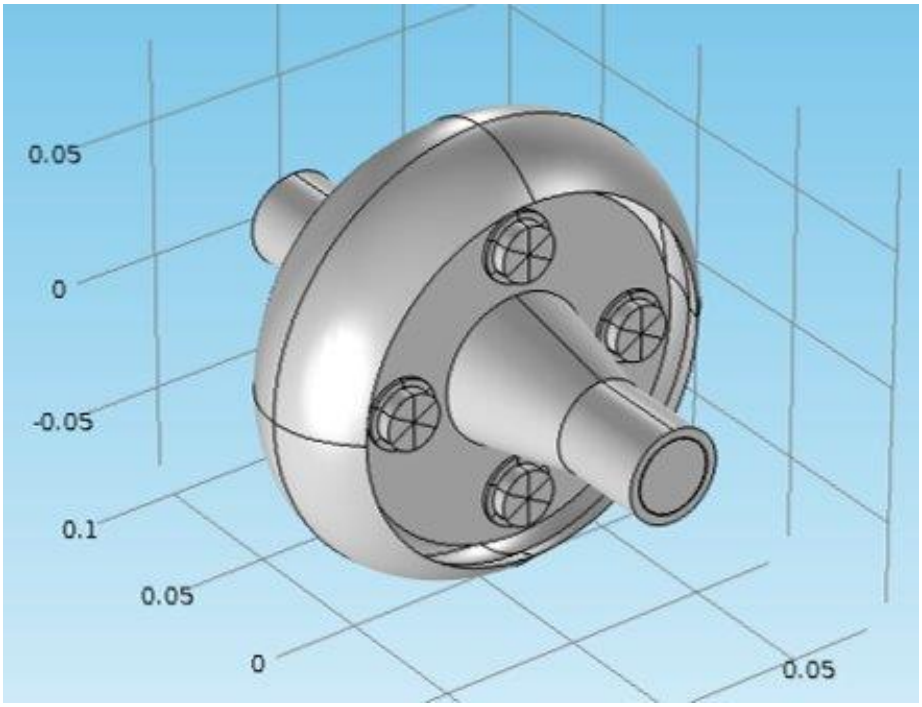

Figure B- 9: COMSOL model of fender/flange system

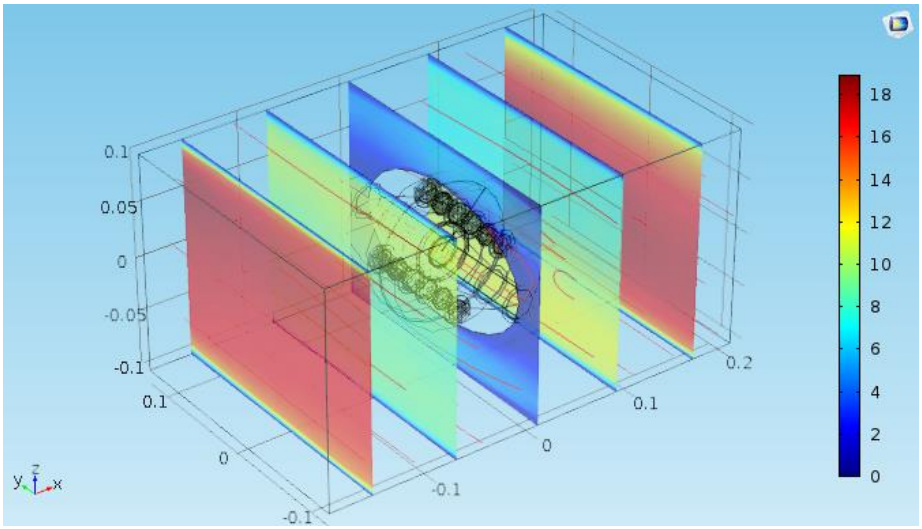

Figure B- 10: Wind velocity profiles around flange

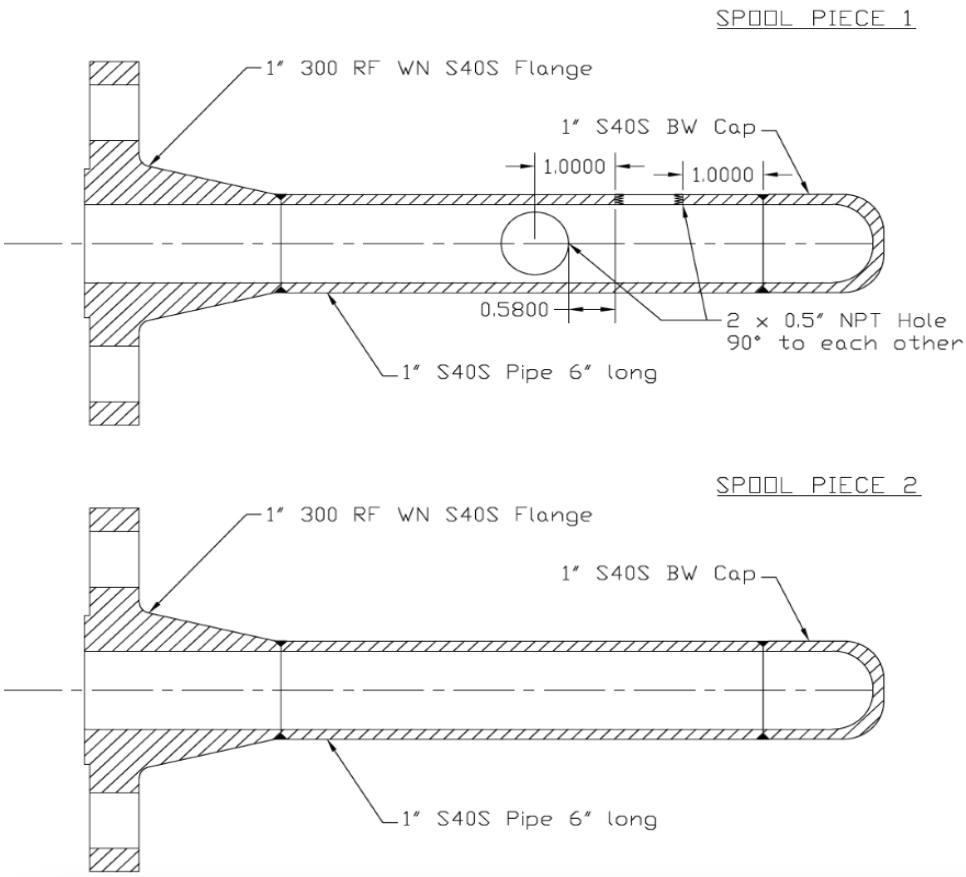

Figure B- 11: Detailed 2D drawing of the flange from Pro-Flange Ltd.

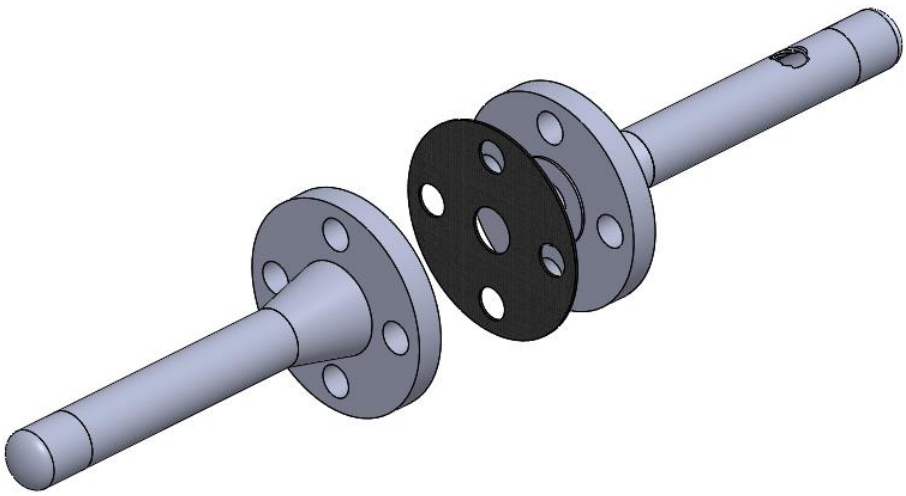

Figure B- 12: 3D drawing of flange, with pipe and gasket from Pro-Flange Ltd.

Glossary

CH_4: methane

CO_2: carbon dioxide

ECCC: Environment and Climate Change Canada

EPA: Environmental Protection Agency

GHG: greenhouse gas

LDAR: leak detection and repair

O&G: oil and gas

SMO: semiconducting metal oxide

SPE: solid polymer electrolyte

EIS: Electrochemical Impedance Spectroscopy

LIG: Laser Induced Graphene

FTIR: Fourier Transformation Infrared Spectroscopy